NASA-CR-204584

**Bureau of Engineering Research**
**The University of Texas at Austin**
**Austin, Texas**

**CAR 96-2**

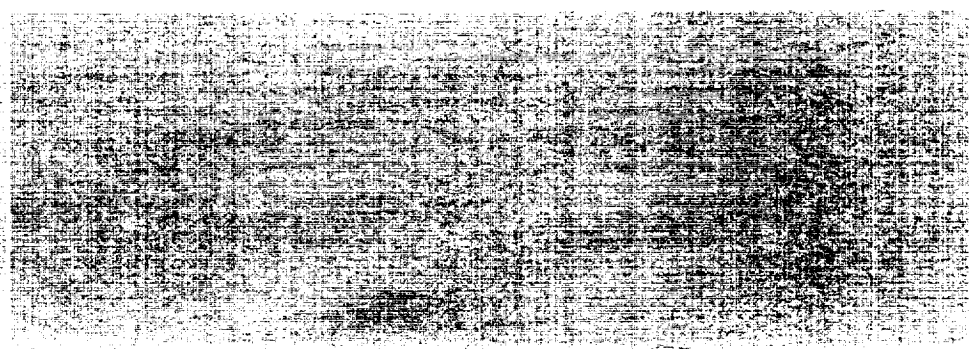# A FREQUENCY-DOMAIN SUBSTRUCTURE
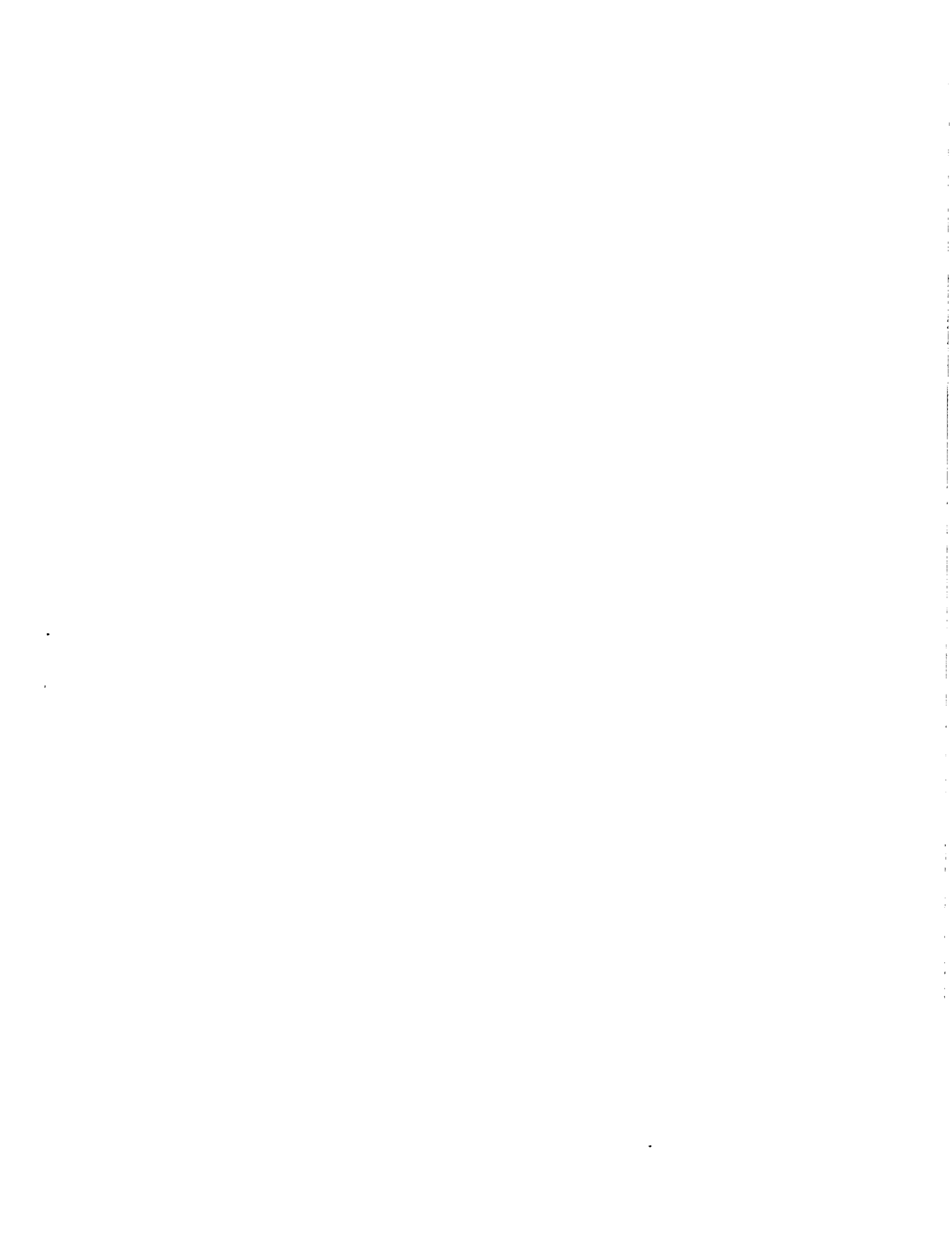# SYSTEM IDENTIFICATION ALGORITHM
by
Eric L. Blades and Roy R. Craig, Jr.

# A FREQUENCY-DOMAIN SUBSTRUCTURE SYSTEM IDENTIFICATION ALGORITHM

by

Eric L. Blades

Roy R. Craig, Jr.*

Report No. CAR 96-2

REPORT

for

Center for Aeromechanics Research

(formerly Center for Aeronautical Research)

Bureau of Engineering Research

College of Engineering

The University of Texas at Austin

Austin, Texas 78712

August 1996

*John J. McKetta Energy Professor in Engineering

# Acknowledgments

# Abstract

A new frequency-domain system identification algorithm is presented for system identification of substructures, such as payloads to be flown aboard the Space Shuttle. In the vibration test, all interface degrees of freedom where the substructure is connected to the carrier structure are either subjected to active excitation or are supported by a test stand with the reaction forces measured. The measured frequency-response data is used to obtain a linear, viscous-damped model with all interface-degree of freedom entries included. This model can then be used to validate analytical substructure models. This procedure makes it possible to obtain not only the fixed-interface modal data associated with a Craig-Bampton substructure model, but also the data associated with constraint modes. With this proposed algorithm, multiple-boundary-condition tests are not required, and test-stand dynamics is accounted for without requiring a separate modal test or finite element modeling of the test stand. Numerical simulations are used in examining the algorithm's ability to estimate valid reduced-order structural models. The algorithm's performance when frequency-response data covering narrow and broad frequency bandwidths is used as input is explored. It's performance when noise is added to the frequency-response data and the use of different least squares solution techniques are also examined. The identified reduced-order models are also compared for accuracy with other test-analysis models and a formulation for a Craig-Bampton test-analysis model is also presented.

# Table of Contents

# List of Tables

# List of Figures

# Chapter 1

# Introduction

The dynamic behavior of complex engineering structures can be predicted by using various analytical and numerical methods, with the most popular method being the finite element method. A finite element model (FEM) is an approximation of a continuous structure, and assumptions are made in the development of the FEM concerning the distribution of mass and stiffness, approximation of boundary conditions, estimation of material properties, and so forth. As a result, the FEM may or may not accurately represent the original structure. Before this mathematical model can be used to perform any sort of analysis and the results used with confidence, the model must be test-validated to ensure that it accurately represents the physical structure. Thus, there exists the need to be able to characterize the dynamic behavior of structures experimentally.

For some structures, performing a vibration test on the entire structure is usually not feasible or practical due to the size and complexity of the structure. To facilitate testing, the original structure is divided into smaller, more manageable components, referred to as substructures. Component mode synthesis, or substructuring, techniques are generally employed to analyze the individual components and couple them together to form an analytical model of the original structure [1, 2]. For example, the Space Shuttle Orbiter, pay-

load, external tank, and solid rocket boosters are each substructures which can be analyzed individually and coupled together to form the final launch vehicle model.

To verify an individual substructure model, a modal test is performed to identify the modal parameters of the actual substructure. The modal parameters of interest are the natural frequencies, damping factors, natural mode shapes, and the residual mass and stiffness. Since the natural frequencies are scalar quantities, they can be readily compared. The comparison of the mode shapes is not as straightforward and involves orthogonality and cross-orthogonality checks using the experimental mode shapes and test-analysis models.

When the vibration test is performed, the boundary conditions should be representative of those experienced during actual flight conditions. It is important that that the correct boundary conditions be provided at the substructure interface locations in order to obtain accurate results. For Space Shuttle payloads, this has sometimes led to fixed-base modal tests being performed to verify the analytical substructure model. The difficulty with this test method is that it requires the interface locations to have zero translational and rotational displacement. In actual test conditions, this situation is very difficult to achieve, since the test stand used to support the test article is rarely rigid enough and the dynamics of the test stand must be considered.

Therefore, to eliminate these problems, a new test method and algorithm called the Substructure System Identification (SSID) algorithm has been developed to identify substructures and verify analytical substructure

models [3, 4]. In the vibration test, all interface degrees of freedom are either actively excited by a shaker or connected to a test stand with the reaction forces measured. The results can be used to obtain a linear, viscous-damped model of the substructure. The purpose of this investigation was to verify the proposed algorithm's ability to identify valid structural models. Numerical simulations were used to simulate test data, and the algorithm's performance when noise was added to the test data, and the effects of spatial and frequency truncation, were examined.

Chapter 2 reviews pertinent test methods and structural system identification algorithms. In Chapter 3, the theory of the Substructure System Identification algorithm is discussed. Model reduction and various test-analysis models used to aid in the comparison between the test and analytical results are discussed in Chapter 4. Chapter 5 highlights some of the computational aspects of the SSID algorithm that affect the final solution, such as different methods for solving an over-determined system of linear equations. In Chapter 6, the results of various numerical simulations using the SSID algorithm are presented and analyzed. Finally, in Chapter 7, conclusions are drawn and recommendations for future research are proposed.

# Chapter 2

# Review of Literature

Reviews of previous test methods and structural system identification algorithms that are relevant to this work are given in this chapter. Test verification methods are discussed in Section 2.1. Section 2.2 reviews several different time-domain and frequency-domain structural system identification algorithms.

## 2.1 Test Verification of Analytical Substructure Models

### 2.1.1 Test Verification of Finite Element Structural Models

The response of complex structures subjected to dynamic loading has been a subject of interest for many decades. The finite element method is usually employed to facilitate the analysis of the structure. A finite element model of the continuous structure is created by discretizing it to $N$ finite degrees of freedom (DOF). The resulting second-order differential equations of motion for a linear time-invariant model can be written in the form

$$M\ddot{x}(t) + C\dot{x}(t) + Kx(t) = Df(t) \tag{2.1}$$

where $M$, $C$, and $K$ are respectively the mass, damping, and stiffness matrices of the system, $x(t)$ is the time-dependent coordinate vector, $D$ is the force-distribution matrix, and $f(t)$ is the time-varying applied force. Based on the

4

following physical assumptions about the structure, the system matrices are assumed to be positive definite or semidefinite: 1) all degrees of freedom have inertia, so the system kinetic energy is strictly positive and the mass matrix is positive definite, 2) for any forced motion, the system does not create energy, so the damping matrix is positive semidefinite, and 3) the strain energy is always positive, so the stiffness matrix is positive semidefinite.

The FEM must provide a physically significant representation of the physical structure. However, assumptions are made in the development of the FEM, and much expertise is required in order to obtain reliable and valid results. The initial FEM must be experimentally validated before it can be used to predict the response of the structure.

An experimental model can be obtained using one of the identification algorithms described in the next section. Then, a comparison between the experimental model and an analytical test-analysis model (TAM) is made in an attempt to verify the math model. Test-analysis models are discussed further in Chapter 4.

The analytical model is deemed to be a good representation of the physical structure if there is good agreement between the measured and analytically computed modal parameters. Generally, if the identified natural frequencies are within 10%, and an orthogonality check of the test modes with respect to a TAM mass matrix is satisfied, the math model is considered "test-verified." Acceptable orthogonality results are characterized by values of all of the off-diagonal terms being less than 0.1 when the diagonal values are normalized to unity [5]. The test data is generally considered to be correct, therefore

any discrepancies between the analytical and the measured modal parameters are attributed to the math model.

Numerous procedures exist for updating the finite element model to match the experimental data. There are two general approaches for model updating. One approach is to modify the entire matrices, and the other is to update only individual elements within the matrices [6, 7]. The analytical mass matrix is generally considered to be a good estimation of the structure's mass characteristics, so many updating techniques focus on updating only the stiffness matrix. There also exist numerous methodologies that update the analytical model so as to minimize the difference between the analytical and experimental frequency response functions [8].

### 2.1.2 Space Shuttle Payload Model Verification Tests

A coupled-loads analysis for lift-off and landing events must be performed for any payload that will fly aboard the Space Shuttle. The mathematical model used to perform the coupled-loads analysis must be in the form of Craig-Bampton modes or mass and stiffness matrices [9]. Before using the math model in the coupled-loads analysis, the math model must be test-verified by correlating it with modal test data.

Test-verification of math models has traditionally been accomplished by performing a modal test on the payload with the interface degree of freedom constrained. For a proper validation, the boundary conditions imposed during the test should match those in service, which has led to the use of fixed-base testing as a common approach used to verify the constrained math models.

There are two different attachment configurations that may be used, depending on the size of the payload. Larger payloads are supported by four lateral trunions and a keel trunion. Figure 2.1 illustrates the payload-orbiter boundary conditions for larger payloads. Shorter payloads are supported by two lateral trunions and a single keel trunion. Ideally, the trunions are restrained in only one or two translational degrees of freedom with all other degrees of freedom free.
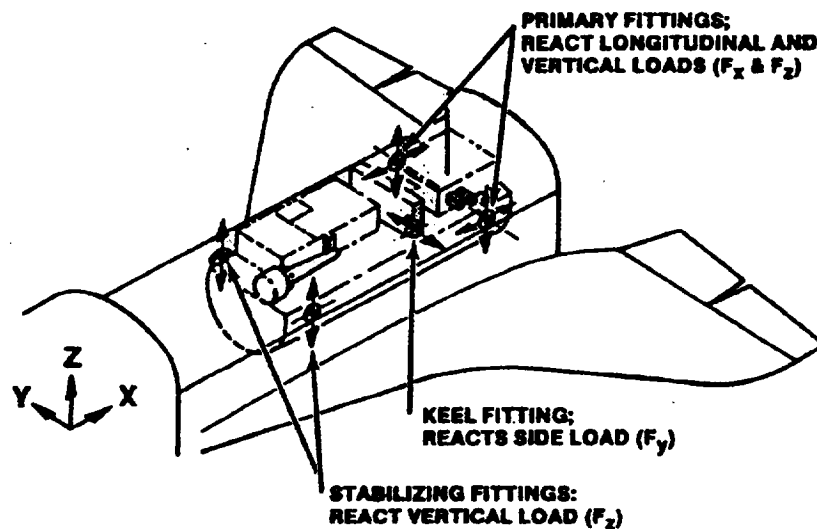


Figure 2.1: Payload-Orbiter Boundary Conditions

For payload math models, the Craig-Bampton form is often used. In order to experimentally verify a Craig-Bampton substructure model, the component fixed-interface modes must be validated. Measuring the fixed-interface modes involves attaching the substructure to a test-stand in a manner such that the appropriate translational displacements at interface degrees of freedom are

8

zero. Therefore, a large and rigid test-stand has to be constructed and tested to ensure that its fundamental frequency is above the frequency range of interest of the substructure. This requirement is to ensure that there is no coupling between the test stand and the test article. Construction of such a test-stand is usually very expensive. Frequently, the test stand will not be rigid enough and test-stand dynamics must be accounted for by performing additional modal tests or finite element analysis of the test-stand. The terms related to the constraint modes in the Craig-Bampton model are seldom test-verified.

Additional difficulties involved with fixed-base testing make the approach very difficult and impractical in many cases. Reference [10] describes some of the difficulties encountered in the fixed-base test of a Space Station module prototype; mainly that the interface degrees of freedom could not be properly represented, which introduced nonlinearities into the system at the interfaces. Alternate test methods have been suggested using free-free modal test data to verify the constrained modes. Since a rigid test-stand is not required, free-free modal tests are generally less complicated and cheaper to conduct than a fixed-base modal survey. However, the test is performed in a different constraint condition than that used for the coupled-loads analysis, so additional information must be measured at the constraint degrees of freedom, since free-free modes alone are not sufficient to validate a constrained model.

A mass-additive technique was used as an alternative to fixed-base testing to derive constrained modes from free-free modes to verify a Space Station prototype module and a Space Shuttle payload [11]. Large masses were added at the interface locations and a superposition of the mass-loaded normal

modes was used to obtain the constrained modes. The additional masses at the interface locations lowered the frequency of the local "trunion modes" into the bandwidth of the global modes of the structure. The additional masses also allowed the interfaces to be exercised more than during a free-free test. This method was found to work better for structures having well-spaced natural frequencies than for those with high modal densities, like the Space Station module. Drawbacks of this method are that a large number of mass-additive modes are required to derive the fixed-base modes, which increases the difficulty of the correlation task, and that it may be difficult to determine the proper size of the interface masses. Reference [12] contains details of the free-free modal test that was used to obtain the experimental data and also a description of the problems encountered during the fixed-base modal test of the Space Station module.

The residual flexibility approach has also been used as a technique for deriving constrained structural modes from free-free modes supplemented with residual dynamics information. A successful application of the residual flexibility approach to test-validate a Space Shuttle payload is given in References [13, 14]. The residual flexibility information was obtained from drive-point frequency response functions at each of the payload-shuttle interface locations by subtracting the synthesized response from the measured response. The payload FEM was then adjusted to match the free-free modes and the residual flexibility terms. Admire, et al., also used the residual flexibility approach to verify math models of the Space Station prototype module and a Space Shuttle payload [15]. The same approach utilized in Ref. [13] was followed, and it was shown that the residual flexibility method worked well and was bet-

ter suited than the mass-additive approach for the Space Station module. It was concluded that the approach can be used as an alternative to constrained boundary testing, but measurement techniques need to be improved to better measure the required frequency response functions associated with the residual information.

A technique called Interface Verification Testing has also been used as an alternative to fixed-base testing for verification of Space Shuttle payload math models [10, 16, 17]. Free-free data is supplemented with additional data obtained by exciting a single interface degree of freedom while the structure is is freely suspended. The additional information that is obtained in this test provides the residual flexibility and is reflected in the location of the zeros of the inertance frequency response function. This set of data can be used to verify the constrained payload math model. The authors also mention the problem of accurately measuring the residual information, since the residual information is typically on the order of $1.0\ E^{-6}$ in./lb, and all of the modal curve fit error is contained in the residual curve fit.

Recent attempts have also been made to design interface connections that simulate the payload attachment mechanism. The concept is to have the test fixture, or flexure, designed to be very stiff in the restrained trunion degrees of freedom and flexible in the un-restrained degrees of freedom. Chung, Sernaker, and Peebles [18] suggest that to ensure that the restrained and un-restrained degrees of freedom do not couple, the axial stiffness should be at least three orders of magnitude greater than the stiffness in bending directions. The flexure should also be designed to transmit the load properly and to minimize

interaction with the test article. Mühlbauer, Troidl, and Dillinger have designed a flexure using cylindrical rods with flexible sections at each end that act as elastic hinges for an interface degree of freedom [19]. One such flexure is used at each trunion interface attachment and these flexures have been used for several verification tests with good results reported.

## 2.2 Structural System Identification

Structural system identification is the process of using experimentally acquired data to obtain some sort of useful model of the test article that characterizes the dynamics of the structure. System identification algorithms have been formulated in both the time domain and the frequency domain, and each has its own advantages and disadvantages [20]. A comparison and evaluation of several identification algorithms and the test requirements needed to satisfy the assumptions of each as applied to the Galileo spacecraft is given in Reference [21].

The most important advantage of time-domain techniques is that they are generally better conditioned numerically than an equivalent frequency-domain implementation [22]. This is believed to be due to the power to which the frequency values are raised in the frequency-domain equations of motion, which increases the dynamic range of the numerical data. For this reason, most frequency domain estimation methods generally work better for narrow frequency band analysis. Frequency-domain algorithms based on orthogonal polynomials have attempted to alleviate this problem [23]. Frequency-domain algorithms have the advantage that they can compensate for the effects of out-

of-band modes, or residual dynamic effects, while time-domain methods cannot represent residual effects [24].

Experimental models have traditionally been obtained by experimental modal analysis techniques, which attempt to identify the modal parameters of the structure, that is, the natural frequencies, damping factors, natural mode shapes, modal participation factors, and the residual mass and stiffness [5]. The response of the system is described in terms of a linear superposition of the characteristic solution of the differential equations. The modal parameters are then obtained by curve-fitting the measured data.

Another approach to obtain the experimental model is to estimate the system matrices, that is, to identify the mass, damping, and stiffness matrices directly from measured system responses. This approach is referred to as Direct System Parameter Identification (DSPI) [25]. The matrices are estimated directly from the measured input and output data. An eigenvalue decomposition of the estimated matrices results in the desired modal parameters.

### 2.2.1 Time-Domain Identification Algorithms

For time-domain system identification, much effort has recently been put forth to develop state-space realization procedures. Most notable among these is the Eigensystem Realization Algorithm (ERA) by Juang and Pappa [26] and its derivatives [27, 28]. A widely used time-domain identification algorithm in the modal test community is the Polyreference algorithm [29]. In Ref. [30], Juang relates the algorithmic properties of the Polyreference algorithm to a state-space canonical-form realization.

Since all vibration test data is discrete in nature, all time-domain linear system realization procedures begin with the assumption that a finite order discrete state-space model of the system exists, and that it is of the form

$$\begin{aligned} \dot{x}(k+1) &= Ax(k) + Bu(k) \\ y(k) &= Cx(k) + Du(k) \end{aligned} \tag{2.2}$$

where $x$ is the $N \times 1$ state vector, $u$ is the $m \times 1$ input vector, $y$ is the $l \times 1$ output vector, $A$ is the $N \times N$ state transition matrix, $B$ is the $N \times m$ input influence matrix, $C$ is the $l \times N$ output influence matrix, $D$ is the $l \times m$ matrix corresponding to direct input/output feedthrough, and $k$ is the time sample index. Note that the $C$ and $D$ matrices in Eq. 2.2 are not the same as the ones in Equation 2.1. The solution for the output $y(k)$ to an arbitrary input $u(k)$ is given by

$$y(k) = \sum_{i=0}^{k} Y(k-i)u(i) \tag{2.3}$$

where $Y(i)$ are the discrete-time impulse response functions, which are referred to as *Markov parameters*. The Markov parameters are related to the state-space matrices by

$$Y(k) = \begin{cases} D & k = 0 \\ CA^{k-1}B & k > 0 \end{cases} \tag{2.4}$$

Given a measurement sequence of Markov parameters, the system realization problem is to find a minimal-order realization of the state-space matrices that best approximates the given Markov sequence.

The main problems in system realization are determination of the model order and the state-space parameters. The Eigensystem Realization Algorithm provides a systematic approach for determining a minimal-order

model of a given accuracy and for determination of the discrete state-space model. The algorithm uses a discrete-time shift of the Markov parameters to form a *Hankel matrix*, which is defined as

$$H_{qd}(k) = \begin{bmatrix} Y(k+1) & Y(k+2) & \cdots & Y(k+d) \\ Y(k+2) & Y(k+3) & \cdots & Y(k+d+1) \\ \vdots & \vdots & \vdots & \vdots \\ Y(k+q) & Y(k+q+1) & \cdots & Y(k+q+d-1) \end{bmatrix} \qquad (2.5)$$

where $q$ and $d$ are arbitrary integers. The rank of $H_{qd}(0)$ is estimated from a singular value decomposition, and the largest $N$ singular values are selected to determine the model order. The discrete state-space matrices are formed from the left and right singular vectors and the $H_{qd}(1)$ Hankel matrix. Once the state-space matrices are known, the modal parameters can be extracted.

Su and Juang [31] developed a time-domain algorithm for system identification at the substructure level. A procedure is presented to determine and assemble substructure Markov parameters. Using the Markov parameters, substructure transfer functions can be computed and used to determine substructure state-space models. A procedure is also outlined to couple the substructure state-space models to obtain an analysis model for the entire assembled structure. The resulting model describes the dynamics of the substructures when the appropriate interface compatibility and equilibrium conditions are enforced. The authors note that to enforce compatibility and equilibrium conditions at the substructure interface locations, co-located sensors and actuators are needed at all of the interface degrees of freedom.

The common basis normalized structural identification (CBSI) procedure developed by Alvin and Park [32] uses the Eigensystem Realization

Algorithm, or any other state-space-based system identification technique, as a precursor to determine a second-order structural dynamics model from a minimal-order discrete state-space model. The authors point out that for the solution of the system realization problem, there are an infinite number of equivalent realizations for the given data. A transformation is developed to determine the underlying physically based structural model from the mathematical state-space identified model. The realized model, after the transformation, has a one-to-one correspondence with the physical parameters of the system and can be used to determine the mass, damping, and stiffness matrices of the system.

### 2.2.2 Frequency-Domain Identification Algorithms

Leuridan, et al., present a frequency-domain DPSI approach that utilizes a straightforward linear estimation to identify the system matrices [25]. Beginning with the frequency-domain equations of motion

$$
\begin{bmatrix} M & C & K \end{bmatrix} \left\{ \begin{array}{c} -\omega^2 X(\omega) \\ j\omega X(\omega) \\ X(\omega) \end{array} \right\} = DF(\omega) \tag{2.6}
$$

the system matrices are solved for directly. However in its present form, Eq. 2.6 cannot be solved very easily. A technique developed in Ref. [33] is used to rewrite the matrix of unknowns as a vector and cast Eq. 2.6 in the more familiar and readily solvable form $Ax = b$. However, the resulting equations are highly ill-conditioned, and numerical techniques should be used to minimize the effects of the ill-conditioning. An advantage of the method is that it uses all of the measurement data from multiple inputs simultaneously in the identification

procedure. By doing so, it takes advantage of redundant information in the data and reduces the influence of measurement noise errors. However, the authors point out that if the input frequency data does not fit the model or does not contain enough information to form a complete model, the method will become unstable and diverge.

One of the earliest algorithms to identify the system matrices relates the matrices to measured complex modes and frequencies [34]. A similar approach is also presented by Balmès [35]. The equations of motion must be cast in first-order form to include the effects of damping in the ensuing eigenproblem. Just as in the second-order eigenvalue problem, two orthogonality conditions result. After some algebraic manipulation and employing the two orthogonality conditions, the following expressions are arrived at for the mass, damping, and stiffness matrices:

$$M = (\Psi\Lambda\Psi^T)^{-1}, C = -M\Psi\Lambda^2\Psi^T M, \text{ and } K = -(\Psi\Lambda^{-1}\Psi^T)^{-1} \qquad (2.7)$$

where $\Psi$ is the normalized displacement partition of the complex modal matrix, and $\Lambda$ is a diagonal matrix of the complex eigenvalues. An expression, $\Psi\Psi^T = 0$, referred to as the properness condition, is also presented in the derivation of Equation 2.7. The properness condition implies that the measured mode shapes are consistent with measured displacement quantities, and this constraint must be satisfied in order for the solution of the inverse problem to be physically consistent in the determination of the mass and stiffness matrices. The algorithm uses the pole and residue information obtained from some other algorithm to estimate the complex mode shapes and frequencies. The scaling of the complex modes is accomplished through information associ-

ated with a drive-point transfer function. A least-squares estimation is used to minimize the phase of the complex mode shapes since it is assumed that the complex modes should be mostly real. To enforce the properness condition, a constraint minimization problem must be solved for the final estimation of the complex modes before the system matrices are computed. In the current formulation, this algorithm allows for only a single input to be used in the scaling procedure. However, most vibration tests employ multiple inputs, so some sort of yet-to-be-defined averaging algorithm of the co-located sensor information is required before this method can be used with multiple-input test data.

A frequency-domain direct identification algorithm developed by Lembregts [36, 37] uses a state-space formulation to solve for system matrices. The equations of motion are written in first order form as

$$\left\{ \begin{array}{c} \ddot{x} \\ \dot{x} \end{array} \right\} = \left[ \begin{array}{cc} -\tilde{A}_1 & -\tilde{A}_2 \\ I & 0 \end{array} \right] \left\{ \begin{array}{c} \dot{x} \\ x \end{array} \right\} + \left[ \begin{array}{c} M^{-1}D \\ 0 \end{array} \right] f(t) \qquad (2.8)$$

where $\tilde{A}_1 = M^{-1}C$, $\tilde{A}_2 = M^{-1}K$, and $D$ is the force distribution matrix. A Laplace transformation is used to derive an expression to determine $\tilde{A}_1$ and $\tilde{A}_2$ from the measured frequency response data. The ensuing first-order algebraic eigenvalue problem

$$\left[ \begin{array}{cc} \tilde{A}_1 & \tilde{A}_2 \\ I & 0 \end{array} \right] \left[ \begin{array}{c} \Theta\Lambda \\ \Theta \end{array} \right] = \left[ \begin{array}{c} \Theta\Lambda \\ \Theta \end{array} \right] \Lambda \qquad (2.9)$$

is then solved to identify the modal parameters. The algorithm does allow for simultaneous use of multiple input data and also can include terms to compensate for residual effects. Before the identification procedure begins, an optimal model order is selected and a singular value decomposition is performed on the measured frequency response data to condense the data to the appropriate

18

model order. In order to compensate for noise in the data, measurement error, and residual effects, the model order is selected to be greater than the number of physical modes present in the data . In this algorithm, an assumption is made that the number of observable modes is less than or equal to the number of output measurement locations. This is a fundamental limitation of this technique. In test situations, this implies that the frequency band over which data is being measured must be narrow enough so that there are fewer modes than output measurements.

Recently, a Unified Matrix Polynomial Approach (UMPA) [38]–[40] has been developed to show that many modal parameter estimation methods can be reformulated in a consistent framework. The Unified Matrix Polynomial Approach is a direct parameter identification method and allows multiple-input systems. The model is described in the Laplace domain by a rational fraction polynomial of the form

$$\left(\sum_{i=0}^{n}[A_i]s^i\right)\{X(s)\} = \left(\sum_{i=0}^{m}[B_i]s^i\right)\{F(s)\} \qquad (2.10)$$

where $[A_i]$ and $[B_i]$ are the unknown UMPA coefficient matrices, $n$ and $m$ are the model orders of the input and output, and $s$ is the Laplace variable ($s = j\omega$). The coefficient matrices are estimated from the measured input-output data using a total least squares estimation having the form

$$\begin{bmatrix} A_0 & A_1 & A_2 & B_0 \end{bmatrix} \begin{bmatrix} X(\omega) \\ j\omega X(\omega) \\ -\omega^2 X(\omega) \\ -F(\omega) \end{bmatrix} = 0 \qquad (2.11)$$

where $A_0 = K$, $A_1 = C$, $A_2 = M$, and $B_0 = D$. A description of the total least squares method is given in Chapter 5. Once the coefficient matrices

are estimated, the modal parameters are estimated by solving the algebraic eigenvalue problem of Equation 2.9.

Frequently, in structural dynamics testing the number of output measurements is less than the number of modes in the frequency bandwidth over which the test is being performed. As previously mentioned, some identification algorithms require that the number of sensors be equal to or greater than the number of observable modes. To get around this problem of spatial truncation, Alvin, Peterson, and Park [41] developed a method to determine minimal-order mass and stiffness matrices when the number of observable modes is greater than the number of available sensors. The resulting minimal-order matrices express contributions of all modes that are observable from the available sensors. The measured physical degrees of freedom are augmented with a set of generalized coordinates which possess information about the residual dynamics of the system. A singular value decomposition of the residual dynamic matrix is used to determine the rank deficiency of the reduced stiffness, and the required minimal-rank augmentation is the number of nonzero singular values. The minimal-order mass and stiffness matrices are formed by augmenting the mode shapes with the singular vectors. A drawback of this method is that it assumes that a set of mass-normalized mode shapes can be measured, and it is these real normal modes that are used to compute the minimal-order mass and stiffness matrices.

A procedure for identification of modal parameters using both time- and frequency-domain procedures is described in Reference [24]. The model order is selected using time-domain procedures, and the modal parameters are

estimated by using frequency-domain procedures that are able to represent residual effects. To determine the number of modes present in the data, the singular values of the frequency response function matrix are examined and a modal indicator function is also used. The size of the Hankel matrix is selected by observing the convergence of its singular values while varying the number of rows and columns of the Hankel matrix. Once the singular values converge and the size of the Hankel matrix is chosen, the model order is varied from 1/2 to 4 times the number of modes observed in the data. Modal quality indicators are then used to eliminate poles and to study the convergence of modal frequencies and damping ratios. The modal vectors are extracted from the converged poles in a least squares frequency-domain curve fit. The frequency-domain curve fit includes an improper term as an unknown, which compensates for the fact that discrete state-space models cannot represent the effect of modes above the Nyquist frequency. The resulting minimal-order model achieves good accuracy in both the time domain and the frequency domain.

## 2.3 Conclusions

This chapter has presented numerous testing methods and structural system identification algorithms. Each one has its own inherent advantages and disadvantages. The selection of one method or algorithm over another depends in large part on the structure under investigation, the purpose for which the identification is being performed, and on the experience of the structural dynamicist. There is an obvious need for a new identification procedure that can overcome many of the previously discussed shortcomings. One such algorithm is discussed in the next chapter.

# Chapter 3

# A Proposed Frequency-Domain Substructure System Identification Algorithm

The Substructure System Identification (SSID) algorithm is a new frequency-domain identification method that can be used to obtain a linear viscous-damped model of a substructure[1]. Every interface degree of freedom is either actively excited by a shaker with the input measured or is supported by the test stand with the reaction forces measured. The substructure is "isolated" from the test stand by measuring the reaction force; thus the substructure can be identified. In addition, test stand dynamics are automatically taken into account, so there is no need for a separate modal test or finite element model of the test stand. This procedure makes it possible to obtain not only the fixed-interface modal data for a Craig-Bampton substructure model, but also the data associated with the constraint modes.

An overview of the theoretical derivation of the proposed SSID algorithm, which is a two-step identification process, is provided in this Chapter. A complete description of the algorithm is given in Reference [4].

---

[1] Although designed especially to facilitate accurate testing of substructures, the algorithm can be considered to be a "general-purpose" structural system identification algorithm.

21

## 3.1 Identification of $M^{-1}C$ and $M^{-1}K$

Assume that the substructure has viscous damping and that the total number of motion transducers (accelerometers) is at least twice the expected number of normal modes in the frequency range of interest[2]. Every interface degree of freedom is to have a co-located actuator/sensor (force/accelerometer) pair. In addition, there are to be motion sensors (accelerometers) at selected interior degrees of freedom.

Let the equations of motion in physical coordinates and the output equation be

$$M\ddot{x} + C\dot{x} + Kx = Dp(t)$$
$$y = S\ddot{x} \tag{3.1}$$

where $x \in R^{N_x}$ is the displacement vector; $p \in R^{N_p}$ is the input force vector; $y \in R^{N_v}$ is the output measurement vector; $M$, $C$, and $K$ are the system mass, damping, and stiffness matrices; $D$ is the force distribution matrix, and $S$ is the acceleration sensor distribution matrix. For the present discussion, we will assume that the above $N_x$-degree-of-freedom model represents a reduced-order model of the structure. Let the coordinates be partitioned in the following manner:

$$x \equiv \left\{ \begin{array}{c} x_i \\ x_b \end{array} \right\} \equiv \left\{ \begin{array}{c} x_i \\ x_f \\ x_r \end{array} \right\} \tag{3.2}$$

---

[2]This restriction may be relaxed by the method described in Section 6.4.

where $f$ stands for forced DOFs (i.e., DOFs where there is an active force input); $r$ stands for reaction DOFs (i.e., interface DOFs where the tested substructure reacts against the support structure); $i$ stands for interior DOFs (i.e., not a DOF where and active force is applied or a reaction is measured); and $b$ stands for boundary DOFs, the combination of $f$-coordinates and $r$-coordinates. These sets of coordinates are illustrated in Fig. 3.1.
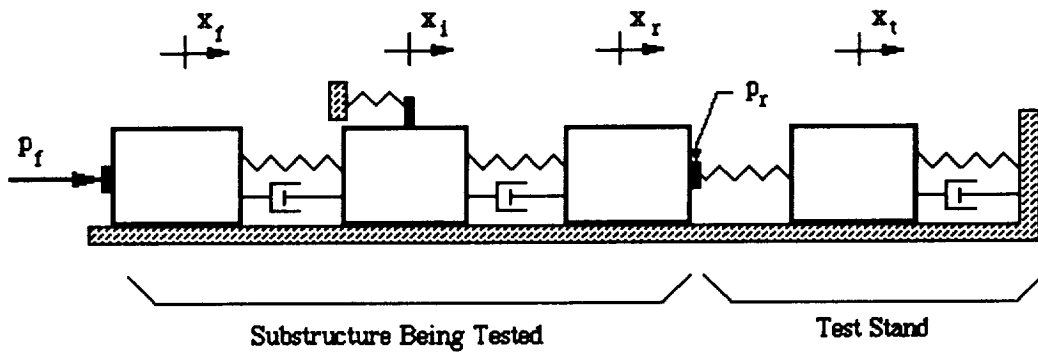


Figure 3.1: Substructure Model – Vibration Test Configuration

Equation 3.1a can be written in the following partitioned form (damping is omitted here):

$$
\begin{bmatrix} M_{ii} & M_{if} & M_{ir} \\ M_{fi} & M_{ff} & M_{fr} \\ M_{ri} & M_{rf} & M_{rr} \end{bmatrix} \begin{Bmatrix} \ddot{x}_i \\ \ddot{x}_f \\ \ddot{x}_r \end{Bmatrix} + \begin{bmatrix} K_{ii} & K_{if} & K_{ir} \\ K_{fi} & K_{ff} & K_{fr} \\ K_{ri} & K_{rf} & K_{rr} \end{bmatrix} \begin{Bmatrix} x_i \\ x_f \\ x_r \end{Bmatrix} = [D]\,p(t) \quad (3.3)
$$

Let us consider the complex frequency response of the substructure due to excitation at frequency $\omega_k$, but with the interior DOFs force-free. Then,

$$
p_k(t) \equiv \begin{Bmatrix} p_f(t) \\ p_r(t) \end{Bmatrix}_k = P(\omega_k)e^{j\omega_k t} \equiv \begin{Bmatrix} F(\omega_k) \\ R(\omega_k) \end{Bmatrix} e^{j\omega_k t} \quad (3.4)
$$

(From Eq. 3.4 onward, the vectors can be complex.) The complex displacement response can be written as

$$x_k(t) = X(\omega_k)e^{j\omega_k t} \tag{3.5}$$

and similar expressions can be obtained for velocity, etc. Then, the frequency-domain version of Eq. 3.1a can be written as

$$\left[ M + \left( \frac{1}{j\omega_k} \right) C + \left( \frac{1}{-\omega_k^2} \right) K \right] A(\omega_k) = \begin{bmatrix} D_f & D_r \end{bmatrix} \left\{ \begin{array}{c} F(\omega_k) \\ R(\omega_k) \end{array} \right\} \tag{3.6}$$

The experimental data input to the algorithm is complex, but the system matrices to be identified are real. To insure that real matrices will be determined, a procedure from Ref. [42] is used. After some algebraic manipulation, the following equation is obtained for estimating the matrices $\hat{C}$, $\hat{K}$, $\hat{D}_f$ and $\hat{D}_r$:

$$\begin{bmatrix} \hat{C} & \hat{K} & \hat{D}_f & \hat{D}_r \end{bmatrix} \begin{bmatrix} \Re\left[\dfrac{H_{af}}{j\omega}\right] & \Im\left[\dfrac{H_{af}}{j\omega}\right] \\ \Re\left[\dfrac{H_{af}}{-\omega^2}\right] & \Im\left[\dfrac{H_{af}}{-\omega^2}\right] \\ -\Re[H_{ff}] & -\Im[H_{ff}] \\ -\Re[H_{rf}] & -\Im[H_{rf}] \end{bmatrix} = \begin{bmatrix} -\Re[H_{af}] & -\Im[H_{af}] \end{bmatrix} \tag{3.7}$$

where

$$\hat{C} = M^{-1}C \ , \quad \hat{K} = M^{-1}K \ , \quad \hat{D}_f = M^{-1}D_f \ , \quad \text{and} \quad \hat{D}_r = M^{-1}D_r \tag{3.8}$$

and the $H$ matrices are measured frequency response function (FRF) matrices and $\Re[\cdot]$ and $\Im[\cdot]$ denote the real part and the imaginary part of the given quantity, respectively. The data used in Eq. 3.7 is stacked in the following manner:

$$
\left[\frac{H_{af}}{j\omega}\right] \equiv \begin{bmatrix} \frac{1}{j\omega_1}H_{a_1f_1}(\omega_1) & \cdots & \frac{1}{j\omega_1}H_{a_1f_{N_f}}(\omega_1) & \cdots & \frac{1}{j\omega_{N_\omega}}H_{a_1f_{N_f}}(\omega_{N_\omega}) \\ \frac{1}{j\omega_1}H_{a_2f_1}(\omega_1) & \cdots & \frac{1}{j\omega_1}H_{a_2f_{N_f}}(\omega_1) & \cdots & \frac{1}{j\omega_{N_\omega}}H_{a_2f_{N_f}}(\omega_{N_\omega}) \\ & & \vdots & & \\ \frac{1}{j\omega_1}H_{a_{N_x}f_1}(\omega_1) & \cdots & \frac{1}{j\omega_1}H_{a_{N_x}f_{N_f}}(\omega_1) & \cdots & \frac{1}{j\omega_{N_\omega}}H_{a_{N_x}f_{N_f}}(\omega_{N_\omega}) \end{bmatrix}
$$

$$(3.9)$$

The other partitions of the data in Eq. 3.7 are formed similarly.

A least squares solution or a total least squares solution of Eq. 3.7 is required. A further discussion of least squares solution procedures is given in Chapter 5. The effects of noise on the input and output signals can be minimized by averaging the FRFs in Eq. 3.7 rather than the force and response spectra of Eq. 3.6.

## 3.2 Identification of $M$, $C$, and $K$

In the previous section, an algorithm was described for identifying the system matrices $\hat{C}$, $\hat{K}$, and $\hat{D}$, which are defined by Eqs. 3.7. From the system matrices $\hat{C}$, $\hat{K}$, and $\hat{D}$, we wish to determine the system matrices $M$, $C$, $K$, and $D$, especially the first three. The first step is to perform an eigensolution using the matrices identified from Eq. 3.7. Let $N_s \equiv 2N_x$, and let us define the state variable

$$z \equiv \left\{ \begin{array}{c} x \\ \dot{x} \end{array} \right\} \tag{3.10}$$

and state matrices

$$\hat{A}_s = \left[ \begin{array}{cc} \hat{C} & I \\ I & 0 \end{array} \right], \ \hat{B}_s = \left[ \begin{array}{cc} \hat{K} & 0 \\ 0 & -I \end{array} \right], \ \hat{D}_s = \left[ \begin{array}{c} \hat{D} \\ 0 \end{array} \right] \tag{3.11}$$

Then the following eigenproblem is solved for the complex eigenvalues $\lambda_r$ and the complex eigenvectors $\hat{\theta}_r$:

$$[\lambda_r \hat{A}_s + \hat{B}_s] \hat{\theta}_r = 0 \qquad r = 1, \ldots, N_s \tag{3.12}$$

To determine the system matrices $M$, $C$, and $K$, a mode-superposition representation of the complex frequency response can be employed. Using the eigenvectors, $\hat{\theta}_r$, let the mode-superposition solution for the states $z$ be

$$z(t) = \sum_{r=1}^{N_s} \hat{\theta}_r \gamma_r(t) = \hat{\Theta} \Gamma(t) \tag{3.13}$$

where orthogonality holds in the following form:

$$\hat{\Theta}^T A_s \hat{\Theta} = \text{diag}(\tilde{a}_r) \ , \quad \hat{\Theta}^T B_s \hat{\Theta} = \text{diag}(\tilde{b}_r) \tag{3.14}$$

with

$$A_s = \left[ \begin{array}{cc} C & M \\ M & 0 \end{array} \right] \ , \quad B_s = \left[ \begin{array}{cc} K & 0 \\ 0 & -M \end{array} \right] \tag{3.15}$$

The following modal-response equations are obtained:

$$\tilde{a}_r \dot{\gamma}_r(t) + \tilde{b}_r \gamma_r(t) = \hat{\theta}_r^T D_s p(t) \tag{3.16}$$

The mode-superposition solution leads, eventually, to the following acceleration frequency response:

$$A_k = -\omega_k^2 X_k = \sum_{r=1}^{N_s} \left(\frac{1}{\tilde{a}_r}\right) \left[R_{kr}\left\{\hat{\theta}_x\right\}_r \left\{\hat{\theta}_x\right\}_r^T\right] DP_k \qquad (3.17)$$

where

$$P_k \equiv \left\{ \begin{array}{c} F(\omega_k) \\ R(\omega_k) \end{array} \right\} \qquad (3.18)$$

$$R_{kr} = \left(\frac{-\omega_k^2}{j\omega_k - \lambda_r}\right) \qquad (3.19)$$

As in deriving Eq. 3.7, assume that averaged frequency-response data are available at $N_\omega$ frequencies, so Eq. 3.17, averaged at each of these frequencies, leads to the following equation:

$$G_{af} = \sum_{r=1}^{N_s} \left(\frac{1}{\tilde{a}_r}\right) \left[R_{kr}\left\{\hat{\theta}_x\right\}_r \left\{\hat{\theta}_x\right\}_r^T\right] [D_f D_r] \left[ \begin{array}{c} G_{ff} \\ G_{rf} \end{array} \right] \qquad (3.20)$$

If Eq. 3.20 is postmultiplied by $G_{ff}^{-1}$, the following expression for the accelerance FRF is obtained:

$$H_{af}(\omega_k) = \sum_{r=1}^{N_s} \left(\frac{1}{\tilde{a}_r}\right) \left[R_{kr}\left\{\hat{\theta}_x\right\}_r \left\{\hat{\theta}_x\right\}_r^T\right] [D_f D_r] \left[ \begin{array}{c} I_{ff} \\ H_{rf} \end{array} \right] \qquad (3.21)$$

Now, the left-hand and right-hand sides of Eq. 3.21 are matrices of dimension $N_x \times N_f$. Let $f_j$ indicate the $j$th column of each side of this equation. Then, write the $j$th column of Eq. 3.21 in the form

$$H_{af_j} = \sum_{r=1}^{N_s} \left(\frac{1}{\tilde{a}_r}\right) \left[R_{kr}\left\{\hat{\theta}_x\right\}_r \left\{\hat{\theta}_x\right\}_r^T\right] [D_f D_r] \left\{ \begin{array}{c} I_{ff_j} \\ H_{rf_j} \end{array} \right\} \qquad (3.22)$$

Finally, let Eq. 3.22 be repeated for each of the $N_\omega$ frequencies and $N_f$ forces, and the resulting equations stacked vertically to form the following equation:

$$\left\{ \begin{array}{c} \left\{ \begin{array}{c} H_{af_1}(\omega_1) \\ \vdots \\ H_{af_1}(\omega_{N_\omega}) \end{array} \right\} \\ \vdots \\ \left\{ \begin{array}{c} H_{af_{N_f}}(\omega_1) \\ \vdots \\ H_{af_{N_f}}(\omega_{N_\omega}) \end{array} \right\} \end{array} \right\} = \left[ \begin{array}{c} \left[ \begin{array}{cccc} E_{11} & E_{12} & \cdots & E_{1,N_s} \\ & & \vdots & \\ E_{N_\omega,1} & E_{N_\omega,2} & \cdots & E_{N_\omega,N_s} \end{array} \right]_{f_1} \\ \vdots \\ \left[ \begin{array}{cccc} E_{11} & E_{12} & \cdots & E_{1,N_s} \\ & & \vdots & \\ E_{N_\omega,1} & E_{N_\omega,2} & \cdots & E_{N_\omega,N_s} \end{array} \right]_{f_{N_f}} \end{array} \right] \left\{ \begin{array}{c} 1/\tilde{a}_1 \\ \vdots \\ 1/\tilde{a}_{N_s} \end{array} \right\}$$

$$\tag{3.23}$$

where

$$[E_{kr}]_{f_j} = \left[ R_{kr} \left\{ \hat{\theta}_x \right\}_r \left\{ \hat{\theta}_x \right\}_r^T \right] \{ D_{f_j} + D_r H_{rf_j} \} \tag{3.24}$$

Equation 3.23 is the key equation that is required to estimate the system matrices $M$, $C$, and $K$. It is used to obtain least squares estimates of the $N_s$ modal parameters $\tilde{a}_r$. The corresponding modal parameters $\tilde{b}_r$ can then be computed from

$$\tilde{b}_r = -\lambda_r \tilde{a}_r \qquad r = 1, \ldots, N_s \tag{3.25}$$

With these values of $\tilde{a}_r$ and $\tilde{b}_r$, the state matrices $A_s$ and $B_s$, defined by Eqs. 3.15, are computed by using Eqs. 3.14, written in the form

$$\begin{aligned} A_s &= \hat{\Theta}^{-T} \text{diag}(\tilde{a}_r) \hat{\Theta}^{-1} \\ B_s &= \hat{\Theta}^{-T} \text{diag}(\tilde{b}_r) \hat{\Theta}^{-1} \end{aligned} \tag{3.26}$$

Finally, the system matrices $M$, $C$, and $K$ are obtained by referring to Eqs. 3.15 and extracting the appropriate partitions of the $A_s$ and $B_s$ matrices that are obtained from Eq. 3.26.

# Chapter 4

# Reduced-Order Analytical Models

As was discussed in the previous chapter, the output of the Substructure System Identification algorithm is the set of characteristic matrices that represent the substructure. Since data can be measured only at a limited number of locations, it is not possible to measure all of the degrees of freedom of a continuous structure. The resulting model is spatially incomplete and can be considered to be a "reduced-order" model of the infinite degree of freedom structure. To relate the resulting SSID matrices to some analytical reduced-order models, several analytical model-reduction methods are discussed and compared in this chapter.

Model reduction is an attempt to reduce the size of an analytical model but still retain the essential dynamic characteristics of the model. An overview of model reduction methods is presented in Section 4.1. In Section 4.2, the Guyan reduction technique is discussed. Section 4.3 describes various other reduction methods in use. Finally, a Craig-Bampton type reduced-order model that is suitable for test-analysis correlation is presented in Section 4.4.

## 4.1 Review of Model Reduction Literature

The finite element method has become a very useful tool in the analysis of modern structures. Stress analysis, failure analysis, internal loads pre-

diction, and design modification usually require very fine discretizations, which can lead to finite element models on the order of tens of thousands (or more) degrees of freedom. Coarse finite element discretizations are not suitable, since they usually do not possess sufficient detail for accurate representations of the mass and stiffness of the structure.

To verify that the FEM is sufficiently accurate to predict the structure's response, the FEM must be test validated. The accuracy of the FEM is often assessed by comparing the modal parameters of the analytical model to those extracted using vibration test data. Test and analysis natural frequencies can be compared directly. However, the modal vectors cannot be readily compared since the FEM will have many more degrees of freedom than the test configuration will have accelerometers. In order to compare the FEM results with the test results, the test vectors need to be expanded to the analytical space or the analytical vectors need to be reduced to the test degrees of freedom. The former has a severe drawback in that errors present in the FEM model that is to be validated are introduced into the test modes that are assumed to reflect the true structure. This corruption of the test data will generally lead to errors in the model validation process. In addition, there are greater computational costs associated with model expansion than with model reduction.

The second approach results in a reduced representation of the FEM, a *test-analysis model* (TAM). This leads to a one-to-one relationship between the TAM degrees of freedom and the number of accelerometers in the test configuration. A number of procedures for generating reduced-order models

have been developed in the past. The reduction methods are based on Ritz-type transformations of the form

$$B = T^T A T \tag{4.1}$$

where $A$ is the original matrix, $B$ is the new matrix, and $T$ is the transformation matrix. The differences between methods lie in the transformation, or interpolation shapes, used to represent the motion of the non-instrumented, or omitted, degrees of freedom in terms of the measured, or retained, degrees of freedom. The measured degrees of freedom will be referred to as the $a$-set (active degrees of freedom) and the omitted degrees of freedom will be referred to as the $o$-set.

The model reduction can be done at the system level or at the component level using component mode synthesis (CMS) methods. The two approaches used most often in system model reduction are Guyan, or static, reduction and modal reduction. The modal reduction approach lends itself very easily to component-mode-synthesis based substructuring methods. Static and modal reduction methods differ in both accuracy and robustness, terms which are defined in Reference [43]. Reference [43] defines accuracy as the measure of the capacity of the reduced-order model to predict the modal frequencies and mode shapes of the FEM. Robustness is defined as a measure of the TAM's ability to show orthogonality of test modes when the FEM has inaccuracies.

## 4.2 Guyan Reduction

The simplest and most straightforward reduction procedure is the Guyan, or static, reduction method [44]. This method is very useful for gener-

ating test-analysis models since the measured degrees of freedom can be selected as the ones to be retained in the reduction process. However, the Guyan reduction method is quite sensitive to the selection of omitted degrees of freedom and often results in poor accuracy if there is inertia associated with the omitted degrees of freedom. Various authors have devised ways for automated selection of the best degrees of freedom to retain [45, 46].

The principal assumption of the Guyan reduction procedure is that inertial forces associated with omitted degrees of freedom are negligible in comparison with the elastic forces transmitted to the omitted degrees of freedom by the motion of the retained degrees of freedom. The mathematical statement of the above assumption is based on solving a static problem of the form:

$$\begin{bmatrix} K_{oo} & K_{oa} \\ K_{ao} & K_{aa} \end{bmatrix} \left\{ \begin{array}{c} x_o \\ x_a \end{array} \right\} = \left\{ \begin{array}{c} f_o \\ f_a \end{array} \right\} \tag{4.2}$$

If there are no loads applied at the omitted degrees of freedom, the upper partition of Eq. 4.2 can be solved, giving

$$x_o = -K_{oo}^{-1} K_{oa} x_a \tag{4.3}$$

This yields the following Guyan transformation matrix from the original degrees of freedom to the $a$-set degrees of freedom:

$$T_{static} = \begin{bmatrix} -K_{oo}^{-1} K_{oa} \\ I \end{bmatrix} \tag{4.4}$$

The $r$th column of the transformation matrix represents the static displacement of the structure when the $r$th $a$-set degree of freedom has a unit displacement and the remaining $a$-set degrees of freedom have zero displacement. This displacement type of shape is commonly referred to as a constraint mode. If

the modal shapes in the frequency range of interest can be expressed as linear combinations of the constraint modes, the Guyan model will be a good approximation.

In the above transformation, it was assumed that there are no forces applied to the omitted degrees of freedom. This is not an accurate assumption if the omitted degrees of freedom possess significant mass. If the omitted degrees of freedom possess large mass-to-stiffness ratios, the omitted inertia terms will be nontrivial, and will cause errors in the natural frequencies and mode shapes of the reduced-order model.

## 4.3   Other Model-Reduction Methods

Since the introduction of the Guyan model reduction method, various attempts have been made to improve upon the Guyan reduction method. A method developed by O'Callahan [47], called the Improved Reduced System (IRS), includes a static approximation to the dynamic inertia terms of the omitted degrees of freedom:

$$T_{IRS} = T_{static} + T_{dynamic} \tag{4.5}$$

where

$$T_{dynamic} = \left[ \begin{array}{c} K_{oo}^{-1}[M_{oa} + M_{oo}T_{static}]M_{static}^{-1}K_{static} \\ I \end{array} \right] \tag{4.6}$$

where $M_{static} = T_{static}^{T}MT_{static}$, $K_{static} = T_{static}^{T}KT_{static}$, and $M$ and $K$ are the original FEM mass and stiffness matrices, respectively. The resulting eigensolution of the reduced-order IRS model is generally more accurate than that obtained using the original Guyan method, but it is still an approximation

of the original FEM dynamics. The original IRS method is applicable for global, or system, models and is not directly applicable for substructure models. Flanigan describes an extension of the IRS method which works with dynamic substructures to create substructure level TAMs [48].

An analysis of the robustness of the IRS method has been given by Gordis [49]. He points out that even though the IRS TAM may provide better estimates of the mode shapes and natural frequencies than the Guyan method, the static TAM may provide better orthogonality of the test modes. This is due to the approximation of the inertia terms by the IRS method and is dependent upon the degrees of freedom that are retained. The retained degrees of freedom should be selected so that the lowest frequency of the modes of the omitted system is above the frequency range of interest; otherwise the approximation of the inertia term will be poorly conditioned.

Kammer introduced a TAM methodology that is a modal reduction method [50]. The advantage of this method is that it produces an increase in accuracy of the natural frequencies and mode shapes. This method provides an exact transformation between the FEM degrees of freedom and the TAM degrees of freedom by using the target modes of interest as the basis of the transformation to relate the omitted degrees of freedom to the retained degrees of freedom. The modal transformation is given by

$$T_{modal} = \Phi_t \Phi_{ta}^g \tag{4.7}$$

$$\Phi_{ta}^g = (\Phi_{ta}^T \Phi_{ta})^{-1} \Phi_{ta}^T \tag{4.8}$$

where the columns of $\Phi_t$ are the target modes, and $\Phi_{ta}^g$ is the generalized inverse of the target modes partitioned to the retained degrees of freedom. This same

transformation was also presented by O'Callahan as the System Equivalent Reduction/Expansion Process (SEREP) [51]. The resulting reduced-order model is in physical coordinates. When the number of target modes used to form the modal transformation is equal to the number of active degrees of freedom, the modal mass and stiffness matrices contain an exact description of the FEM's dynamics for the modes of interest, that is, the natural frequencies and mode shapes are exactly the same as those of the original model. To ensure that Eq. 4.8 is numerically well conditioned, the active degrees of freedom chosen should render the target modes linearly independent and observable.

The static TAM is more robust than the modal TAM in situations where the modes of the test article differ significantly from those measured during the vibration test. This is true even when the modal TAM accurately predicts the natural frequencies. The modal reduction method uses a small number of FEM mode shapes to develop the transformation matrix and this is more limiting than the static methods which use constraint modes for each $a$-set degree of freedom [43]. Kammer [52], and Bhatia and Allemang [53], point out that in some cases, the use of a modal TAM in test-analysis orthogonality and cross-orthogonality computation can result in larger off-diagonal terms than those produced by a "less accurate" static TAM. The authors hypothesize that the discrepancies between the test mode shapes and the FEM mode shapes are due to the modal TAM's poor representation of residual modes. Here, residual modes are those modes that are not included in the transformation matrix.

In an effort to extend the capabilities of the modal TAM method to include an improved representation of the residual dynamics, Kammer devel-

oped the a new method called the hybrid TAM [52]. The hybrid TAM combines the robustness of the static TAM with the accuracy of the modal TAM. Using the target modes, an oblique projector matrix is formed to divide the vector-space containing the TAM dynamics into two complimentary subspaces. The projector matrix, $P$, can be expressed as

$$P = \Phi\Phi^T T_{modal}^T M T_{modal} \tag{4.9}$$

where $\Phi$ is the matrix of FEM mode shapes, $T_{modal}$ is the modal transformation matrix (Eq. 4.7), and $M$ is the original FEM mass matrix. Note that the last three terms are just the modal TAM mass matrix. The transformation matrix for the hybrid TAM can be expressed as a combination of the Guyan and modal transformation matrices

$$T_{hybrid} = T_{static} + (T_{modal} - T_{static})P \tag{4.10}$$

This TAM preserves the exact representation of the target modes and also produces a more accurate representation of the residual modes.

In an approach very similar to Ref. [52], Bhatia and Allemang [53] also develop a transformation that preserves the exact FEM target modes and includes residual mode information. However, their projector matrix is written as

$$P = \begin{bmatrix} \Phi_{ta} & 0 \end{bmatrix} \begin{bmatrix} \Phi_{ta} & \Phi_{ra} \end{bmatrix}^{-1} \tag{4.11}$$

where $\Phi_{ta}$ is the $a$-set partition of the target modes and $\Phi_{ra}$ is the $a$-set partition of the residual subspace. The residual mode information is obtained from the system flexibility matrix and the target modes; thus the residual modes are

38

never computed directly. The residual information is obtained from

$$\Phi_r = G - \Phi_t[diag(\lambda_t^2)]\Phi_t^T \qquad (4.12)$$

where $G = K^{-1}$ is the system flexibility matrix, $\Phi_t$ are the target modes, and $[diag(\lambda_t^2)]$ is a diagonal matrix containing the target natural frequencies.

## 4.4   Craig-Bampton Reduced-Order Models

Component mode synthesis (CMS), or substructuring, is an alternative approach for model reduction. In the CMS approach, the FEM is first divided into several smaller substructures. Each substructure is itself reduced to a smaller number of degrees of freedom. The reduced degrees of freedom include physical coordinates at substructure interface locations and generalized coordinates that represent the component modes of the substructure. Once the substructures are analyzed, the components are coupled together to form the full system model.

The Craig-Bampton method, a variant of the Hurty method [54], is the most popular CMS method, and its derivation is described in Reference [55]. The transformation in the Craig-Bampton method involves component-level fixed-interface normal modes augmented with a set of constraint modes. This results in a model that is statically exact at the boundary locations. This method is usually more efficient and more accurate than a static reduction when the same number of degrees of freedom are retained.

### 4.4.1 Craig-Bampton Model Reduction

The $N$ physical degrees of freedom of the substructure are first partitioned into two sets, the boundary, or interface, degrees of freedom and the interior degrees of freedom:

$$x = \left\{ \begin{array}{c} x_i \\ x_b \end{array} \right\} \tag{4.13}$$

where $x_b$ are the boundary degrees of freedom and $x_i$ are the interior degrees of freedom[1]. Omitting damping, the equations of motion are written as

$$\left[ \begin{array}{cc} M_{ii} & M_{ib} \\ M_{bi} & M_{bb} \end{array} \right] \left\{ \begin{array}{c} \ddot{x}_i \\ \ddot{x}_b \end{array} \right\} + \left[ \begin{array}{cc} K_{ii} & K_{ib} \\ K_{bi} & K_{bb} \end{array} \right] \left\{ \begin{array}{c} x_i \\ x_b \end{array} \right\} = \left\{ \begin{array}{c} f_i \\ f_b \end{array} \right\} \tag{4.14}$$

The Craig-Bampton method uses the Ritz transformation

$$x = T_{CB_1} q \tag{4.15}$$

where

$$T_{CB_1} = \left[ \begin{array}{cc} \Phi_n & \Psi_c \\ 0 & I \end{array} \right] \tag{4.16}$$

$$\Psi_c = -K_{ii}^{-1} K_{ib} \tag{4.17}$$

and $q$ is a vector of generalized coordinates having the form

$$q = \left\{ \begin{array}{c} q_i \\ x_b \end{array} \right\} \tag{4.18}$$

The first column-partition of the Craig-Bampton transformation matrix contains the fixed-interface normal modes. This describes the motion of

---

[1] Although originally developed as a component mode synthesis method, the method can be considered to be a general model-reduction method by simply letting $\underline{i} \rightarrow \underline{o}$ and $\underline{b} \rightarrow \underline{a}$. That is, let "interior" coordinates be more general "omitted" DOFs and, likewise, let "boundary" coordinates be more general "active" coordinates.

the interior degrees of freedom relative to the boundary degrees of freedom in terms of the normal modes of the substructure with the boundary degrees of freedom fixed. The fixed-interface normal modes are obtained by solving the eigenproblem for the interior degrees of freedom

$$(K_{ii} - \omega_r^2 M_{ii})\phi_r = 0 \tag{4.19}$$

or

$$K_{ii}\Phi_n = M_{ii}\Phi_n\Lambda_n \tag{4.20}$$

where the subscript $r$ denotes the $r$th fixed-interface normal mode. The second column-partition of the transformation matrix contains the constraint modes. These are similar to the constraint modes described previously. The $r$th constraint mode is defined by producing a unit displacement at the $r$th boundary degree of freedom with all other boundary degrees of freedom constrained and with all interior degrees of freedom unconstrained.

The final reduced-order matrices obtained are a combination of physical (boundary) coordinates and generalized modal coordinates. These generalized coordinates cannot be used directly for test-analysis correlation and therefore must be transformed into suitable physical coordinates.

### 4.4.2 Craig-Bampton Models in Physical Coordinates

The transformation from generalized coordinates to physical coordinates for Craig-Bampton models is described by Huang and Craig [56]. The interior physical degrees of freedom are partitioned via

$$\{x_i\} = \left\{ \begin{array}{c} x_r \\ x_o \end{array} \right\} \tag{4.21}$$

where $x_r$ are the degrees of freedom where measurements will be made during the vibration test and $x_o$ are the omitted degrees of freedom. The equations of motion can be rewritten as

$$\begin{bmatrix} M_{rr} & M_{ro} & M_{rb} \\ M_{or} & M_{oo} & M_{ob} \\ M_{br} & M_{bo} & M_{bb} \end{bmatrix} \begin{Bmatrix} \ddot{x}_r \\ \ddot{x}_o \\ \ddot{x}_b \end{Bmatrix} + \begin{bmatrix} K_{rr} & K_{ro} & K_{rb} \\ K_{or} & K_{oo} & K_{ob} \\ K_{br} & K_{bo} & K_{bb} \end{bmatrix} \begin{Bmatrix} x_r \\ x_o \\ x_b \end{Bmatrix} = \begin{Bmatrix} f_r \\ f_o \\ f_b \end{Bmatrix} \quad (4.22)$$

Then, Eq. 4.15 can be written as

$$\begin{Bmatrix} x_r \\ x_o \\ x_b \end{Bmatrix} = T_{CB_1} q = \begin{bmatrix} \Phi_r & \Psi_r \\ \Phi_o & \Psi_o \\ 0 & I \end{bmatrix} \begin{Bmatrix} q_i \\ x_b \end{Bmatrix} \quad (4.23)$$

This leads to the transformation matrix $T_{CB_2}$ relating the generalized coordinates to physical coordinates to be used during the test:

$$T_{CB_2} = \begin{bmatrix} (\Phi_{nr}^T \Phi_{nr})^{-1} \Phi_{nr}^T & -(\Phi_{nr}^T \Phi_{nr})^{-1} \Psi_{cr}^T \\ 0 & I \end{bmatrix} \quad (4.24)$$

A similar approach was developed by Kammer [57], but Huang and Craig point out that the contribution of the constraint modes to the transformation matrix $T_{CB_2}$ was not included in Kammer's formulation of the transformation.

The order of the Craig-Bampton model is determined by how many fixed-interface normal modes are used to augment the constraint modes when forming the transformation matrices. If the desired size of the reduced-order model is $k$, then the number of fixed-interface normal modes retained is $n_m = k - n_b$. Typically, only the lowest $n_m$ fixed-interface normal modes are kept. This results in a Craig-Bampton model that accurately predicts the lowest $k$ modes of the substructure. However, if the target modes are not the lowest consecutive modes, then the analytical modes from the Craig-Bampton model will not necessarily correlate well with the target test modes.

In order for the Craig-Bampton model to represent the target modes, a proper set of fixed-interface normal modes must be selected. This set consists of the fixed-interface normal modes that contribute most to the target modes. The selection process is accomplished in the same manner that was used in Ref. [58] to determine which coordinates to select as the rigid-body coordinates to solve a semidefinite eigenvalue problem. Gaussian elimination or other factorization methods can be performed on $\Phi_{nr}$ with pivot selection being used to determine which columns of $\Phi_{nr}$ contribute most to the target modes. Full column and row pivoting is necessary in the event that one of the retained interior degrees of freedom lies along a node line of a fixed-interface normal mode. It was observed, however, that this selection technique was dependent upon the scaling of the fixed-interface normal modes and further study is needed to remove the scaling dependence.

A Craig-Bampton test-analysis model suitable for correlation with the test modes can be obtained by choosing the fixed-interface normal modes that contribute most to the test modes. The final form of the transformations defining the Craig-Bampton TAM are given by

$$M_{CB} = T_{CB_2}^T T_{CB_1}^T M T_{CB_1} T_{CB_2} \tag{4.25}$$

$$K_{CB} = T_{CB_2}^T T_{CB_1}^T K T_{CB_1} T_{CB_2} \tag{4.26}$$

$$f_{CB} = T_{CB_2}^T T_{CB_1}^T f \tag{4.27}$$

where the transformation matrices contain the proper set of fixed-interface normal modes.

# Chapter 5

# Computational Aspects of the SSID Algorithm

This chapter describes some of the computational considerations associated with the SSID algorithm. Section 5.1 contains a description of various methods of solution for a set of linear, algebraic equations. The ill-conditioning associated with frequency-domain identification procedures and a possible remedy for this problem are discussed in Section 5.2. The topic of model order determination is addressed in Section 5.3.

## 5.1 Least Squares Methods

The solution of systems of linear, algebraic equations is involved in the key mathematical steps in the Substructure System Identification algorithm for accurately identifying the substructure. The method of solution can drastically affect the resulting identified system. The methods of solution used in the numerical simulations in this report are the least squares (LS) method and the total least squares (TLS) method. A brief explanation of the methods and of their differences is given here.

The least squares method and the more recent total least squares method are both mathematical modeling procedures used to solve an under- or over-determined linear system of equations of the form

$$AX = B \qquad (5.1)$$

where $A$ is an $m \times n$ data matrix, $X$ is an $n \times d$ matrix of unknowns, and $B$ is an $m \times d$ matrix of observations. A set of under-determined equations results when there are more unknown parameters than equations; for the over-determined system, there are more equations than unknowns. Unless $B$ belongs to the range of $A$, $R(A)$ (i.e., the set is compatible), the over-determined system of equations has no unique solution. This case, which results when the data contains noise, will be denoted by

$$AX \approx B \qquad (5.2)$$

The approximation symbol is used to emphasize that the data (i.e., $A$ and/or $B$) may be contaminated by noise. If there is no noise in the data, then the equality is valid. The least squares method and the total least squares method seek a solution that minimizes the error, $\epsilon$, between the true system model and the measured data. The solution obtained depends on the error model and on the weighting of the data used by each method. If the noise does not match the error model, a biased estimate of the solution will result. An unbiased estimate is one that, on the average, neither tends to over-estimate nor under-estimate the true solution.

Figure 5.1 geometrically illustrates the error models used in the two methods. By depicting the least squares and total least squares methods as measures of goodness-of-fit, the least squares problem is one of minimizing the sum of the squared distances along a single coordinate axis. Whereas the total least squares problem seeks to minimize the sum of the squares of the perpendicular distances of the observed data from the fitted line to provide the best fit.
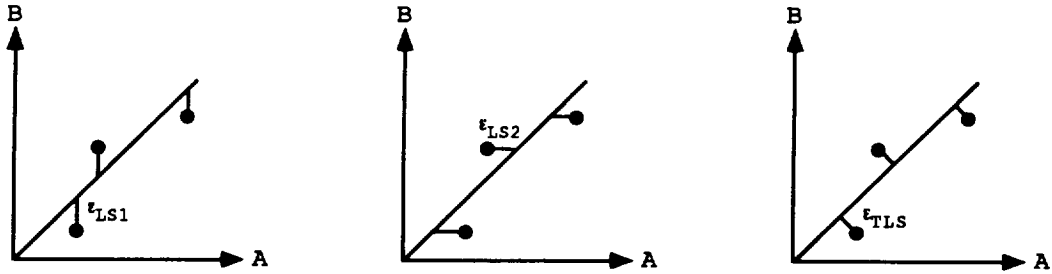
Figure 5.1: LS and TLS Error Models

## 5.1.1 The Least Squares Method

Perhaps the best known method of solution for an over-determined system of linear equations is the least squares method. For simplicity, consider the case when $d = 1$. The accuracy of the least squares solution is independent of the number of right-hand-side vectors used in the computation. In the classical least squares approach, the measurements of the variables in the data matrix $A$ are assumed to be free of error; hence all errors are confined to the observation vector $b$. A least squares estimation could also be made assuming that the observation vector is exactly known and the data matrix contains errors. The least squares method will result in an unbiased estimate if the error model of the given data is of either of the following two forms:

$$Ax = \{b_0 + \Delta b\} \tag{5.3}$$

$$[A_0 + \Delta A]x = b \tag{5.4}$$

where $A_0$ is the true data matrix, $b_0$ is the true observation vector, and $\Delta A$ and $\Delta b$ are the corresponding errors. In most situations, Eq. 5.3 is the form that is assumed, so it will be used here in the following discussion. It is assumed that the errors $\Delta b_i$ and $\Delta A_{ij}$, $i = 1, \ldots, m$ and $j = 1, \ldots, n$ are uncorrelated

random variables with zero mean and equal variance. This assumes that any necessary preprocessing measures on the data such as scaling and centering have been performed in advance.

The classical least squares estimate is equivalent to minimizing the sum of the squares of the differences, or the 2-norm, between the measured observation vector $b$ and an estimated observation vector $\hat{b}$. The least squares problem seeks to min $\|b - \hat{b}\|_2$ where $\hat{b}$ is the orthogonal projection of $b$ onto the $R(A)$. This amounts to perturbing the observation vector $b$ by a minimum amount $\Delta\hat{b}$ so that $\hat{b} = b - \Delta\hat{b}$ can be predicted by the columns of $A$, that is, $\hat{b}$ lies in the $R(A)$. The minimum perturbation, $\Delta\hat{b}$, is the called the least squares correction. The resulting least squares solution, assuming that $A$ is of rank $n$, is

$$\hat{x} = (A^T A)^{-1} A^T\, b \tag{5.5}$$

In addition to the above normal-equation solution, the least squares solution can also formulated using other techniques, such as the singular value decomposition or the Q-R decomposition.

The main assumption made in the classical least squares estimation is that errors only occur in the observation vector $b$ and that the data matrix $A$ is independent of noise. However, this assumption is frequently unrealistic: sampling errors, modeling errors, instrument errors and human errors may imply inaccuracies of the data matrix $A$ as well. This will cause the least squares solution to yield a biased estimate.

## 5.1.2 The Total Least Squares Method

The total least squares method [61] was developed to provide estimates that are generated from a system of linear equations where it is assumed that both the data matrix $A$ and the observation matrix $B$ contain noise. The error model for the total least squares method is of the form

$$[A_0 + \Delta A]\{X\} \approx [B_0 + \Delta B] \tag{5.6}$$

The error criterion again assumes that the errors are uncorrelated random variables with zero mean and equal variance.

The total least squares problem is formulated by rewriting Eq. 5.1 as a homogeneous system of linear equations

$$[A; B] \begin{bmatrix} X \\ -I \end{bmatrix} \approx 0 \tag{5.7}$$

The approximation symbol is again used to emphasize that the data is contaminated by noise. If there is no noise in the data, the right hand side of Eq. 5.7 will be identically zero. The total least squares problem seeks to $\min \| [A; B] - [\hat{A}; \hat{B}] \|_F$ subject to $\hat{B} \in R(\hat{A})$, where $\hat{A}$ and $\hat{B}$ are the total least squares approximations of $A$ and $B$ required to make the set of equations compatible. The Frobenius norm, $\| \cdot \|_F$, is a measure of the size of an $m \times n$ matrix; similar to the vector 2-norm, which measures the length of a vector. Again, for simplicity, assume that $d = 1$.

The solution to this homogeneous system of linear equations is orthogonal to the row space of the augmented data matrix, that is, it is equal to the nullspace of the augmented data matrix. The nullspace of a matrix consists

of all vectors $\hat{x}$ such that $[A; b]\hat{x} = 0$. There are numerous methods that can be used to divide the augmented data matrix into a system subspace and a null subspace, but the numerically stable singular value decomposition is most often used.

Singular value decomposition methods are based on the following theorem of linear algebra [59]: Any $m \times n$ matrix $Z$ can be written as the product of an $m \times m$ column-orthogonal (or unitary if $Z$ is complex) matrix $U$, an $m \times n$ diagonal matrix $\Sigma$ with non-negative elements, and the transpose (Hermitian) of an $n \times n$ orthogonal matrix $V$, that is,

$$Z = U\Sigma V^T \tag{5.8}$$

Assuming that $Z$ is of rank $r$ where ($r \leq \min\{m, n\}$), then [60]:

- The columns of $U$ are called the left singular vectors of $Z$ and are the eigenvectors of $ZZ^T$.

- The first $r$ columns of $U$ form the column space of $Z$.

- The last $m - r$ columns of $U$ form the nullspace of $Z^T$.

- The diagonal elements of $\Sigma$ are the singular values ($\sigma_i$, $i = 1, \ldots, n$) of $Z$ sorted in descending order. The rank of $Z$ is equal to the number of non-zero singular values.

- The singular values squared are the eigenvalues to both $ZZ^T$ and $Z^T Z$.

- The columns of $V$ are called the right singular vectors of $Z$ and are the eigenvectors of $Z^T Z$.

- The first $r$ columns of $V$ form the row space of $Z$.

- The last $n - r$ columns of $V$ form the nullspace of $Z$.

Notice that the columns of $U$ and $V$ give orthonormal bases for all four fundamental matrix subspaces.

The singular value decomposition expresses a matrix as a linear combination of rank-one matrices. The best rank $p$ $(p < r)$ approximation of matrix $Z$ is obtained by retaining the first $p$ terms of this decomposition, which corresponds to the $p$ largest singular values. The error of this approximation is the smallest among all rank $p$ matrices, and is equal to the next singular value $\sigma_{p+1}$ when the 2-norm is used to measure the error.

Let the singular value decomposition of the augmented data matrix $[A; b]$ be given by

$$[A; b] = U\Sigma V^T \tag{5.9}$$

where $U$ is an $m \times m$ matrix, $\Sigma$ is an $m \times (n + 1)$ matrix, and $V$ is an $(n + 1) \times (n + 1)$ matrix. If there were no errors in $A$ and $b$, $b$ would lie in the space defined by the columns of $A$ and the set would be compatible. The rank of matrix $[A; b]$ would be $n$ and the corresponding total least squares correction would be zero. The total least squares solution could be determined from the last right singular vector. However, since $A$ and $b$ contain errors, the matrix $[A; b]$ is of rank $n + 1$ and there is no nonzero vector in the nullspace of $[A; b]$, $N([A; b])$. To obtain a compatible set, the rank of matrix $[A; b]$ must be reduced to $n$. The best rank $n$ approximation of $[A; b]$ is given by

$$[\hat{A}; \hat{b}] = U\hat{\Sigma} V^T \tag{5.10}$$

where $\hat{\Sigma} = \text{diag}(\sigma_1, \ldots, \sigma_n, 0)$. The total least squares minimal correction is thus $\sigma_{n+1} = \min \|[A; b] - [\hat{A}; \hat{b}]\|_F$. The approximate set of equations is now compatible and its solution is given by the only vector $v_{n+1}$ that belongs to $N([\hat{A}; \hat{b}])$. The total least squares solution is obtained by scaling $v_{n+1}$ so that its last component is -1 or

$$\begin{bmatrix} \hat{x} \\ -1 \end{bmatrix} = \frac{-1}{v_{n+1,n+1}} v_{n+1} \tag{5.11}$$

If the rank of the nullspace is greater than one, multiple estimates of the solution vector will exist. This occurs whenever $\sigma_n = \sigma_{n+1}$, or more generally if $\sigma_p > \sigma_{p+1} = \cdots = \sigma_{n+1}$ with $p < n$. This situation also occurs whenever the system of equations is under-determined. Instead of accepting all the solutions as estimates and then performing some type of averaging, a linear combination of the estimates will be used to find the minimum norm total least squares solution.

In the case when $v_{n+1,n+1} = 0$, the total least squares problem may fail to have a solution. This type of problem is referred to as a *nongeneric* problem in the literature. Nongeneric problems occur whenever $A$ is rank-deficient, or when the set of equations is highly conflicting. A total least squares solution may still be found by imposing an additional constraint $\begin{bmatrix} \hat{x} \\ -1 \end{bmatrix} \perp v_{n+1}$.

A generalization of these results can be made to allow for multiple right-hand sides, that is, for $d > 1$, where $B \in R^{n \times d}$. For example, using

Eq. 5.7, Eq. 3.7 can be written as

$$
\begin{bmatrix} \hat{C} & \hat{K} & \hat{D}_f & \hat{D}_r & I \end{bmatrix}
\left\{
\begin{array}{c}
(\frac{1}{j\omega_k})A(\omega_k) \\
(\frac{1}{-j\omega_k^2})A(\omega_k) \\
-F(\omega_k) \\
-R(\omega_k) \\
A(\omega_k)
\end{array}
\right\} \approx 0
\tag{5.12}
$$

The singular value decomposition of matrix $[A; B]$ can be computed as:

$$
[A; B] = U\Sigma V^T = [U_1; U_2]
\begin{bmatrix} \Sigma_1 & 0 \\ 0 & \Sigma_2 \end{bmatrix}
\begin{bmatrix} V_{11} & V_{12} \\ V_{21} & V_{22} \end{bmatrix}^T
\tag{5.13}
$$

where $U$ is an $m \times m$ matrix, $\Sigma$ is an $m \times (n + d)$ diagonal matrix, and $V$ is an $(n + d) \times (n + d)$ matrix. When the rank of matrix $[A; B]$ is greater than $n$, the set is incompatible. The last $d$ singular values, $\sigma_{n+1}, \ldots, \sigma_{n+d}$, are not equal to zeros. The total least squares method forces the equations to be compatible by setting the last $d$ singular values to zero. These are the smallest singular values and are due mainly to the noise in the data. Again, this is the minimal correction to the augmented matrix $[A; B]$. The right singular vectors corresponding to the last $d$ singular values define the nullspace of the augmented matrix and form the total least squares solution. After being properly scaled, the solution is

$$
\hat{X} = -V_{12}V_{22}^{-1}
\tag{5.14}
$$

In practical applications, a threshold value must be set to determine which of the singular values should be set to zero. The threshold value depends in part on the quality of the measurement data. Estimations for the noise level on the data, if such data is available, can be used to determine this minimum value. Note that the ratio $\frac{\sigma_1}{\sigma_n}$ cannot exceed the precision limit of the machine [62].

### 5.1.3 The Scaled Total Least Squares Method

In both of the methods previously discussed, it is assumed that any necessary preprocessing of the data, such as scaling and centering, have been performed in advance. This ensures that the measurement data used in the computation is equalized in magnitude and will result in the best unbiased solution.

The data matrix in Eq. 5.12 can be decomposed into two matrices by using the total least squares error model given in Eq. 5.6,

$$\begin{bmatrix} X & I \end{bmatrix}^H Z \approx 0 \tag{5.15}$$

where

$$X^H = \begin{bmatrix} \hat{C} & \hat{K} & \hat{D}_f & \hat{D}_r \end{bmatrix} \tag{5.16}$$

and

$$Z = Z_0 + E = \left\{ \begin{array}{c} (\frac{1}{j\omega_k})A_0(\omega_k) \\ (\frac{1}{-\omega_k^2})A_0(\omega_k) \\ -F_0(\omega_k) \\ -R_0(\omega_k) \\ A(\omega_k) \end{array} \right\} + \left\{ \begin{array}{c} (\frac{1}{j\omega_k})E_a(\omega_k) \\ (\frac{1}{-\omega_k^2})E_a(\omega_k) \\ -E_f(\omega_k) \\ -E_r(\omega_k) \\ E_a(\omega_k) \end{array} \right\} \tag{5.17}$$

where $Z_0$ is the true error-free measurement data and $E$ is the measurement error matrix. Inspection of Eq. 5.17 reveals that some sort of scaling of the measured data is needed before use in the system identification process. For the frequency range from 10 Hz to 200 Hz, the multiplicative factors associated with the errors range from 1 to $6 \times 10^{-7}$. Therefore, in order to achieve the best unbiased estimation, the data matrix $Z$ should be scaled so that the noise is row-wise equalized.

To perform this equalization, Li, et al. [39, 40] utilized a scaling procedure that is referred to as the *scaled total least squares* method (STLS). For the examples given in Refs. [39, 40], the STLS method results in better estimates than do the least squares method and the total least squares method without scaling. However, the scaled total least squares method assumes that an estimate of the error matrix is available. In test situations, this information is usually not known. A more practical scaling method is thus needed, but Eq. 5.17 emphasizes the need for proper scaling of the measurement data.

It is important to remember that least squares and total least squares are only two possible techniques for estimating the unknown parameters of a linear system. The total least squares method does, however, give the best estimates (in a statistical sense) when the error of the system satisfies the total least squares error model [61].

## 5.2 Narrow-Band Data Processing

It has been mentioned previously that frequency-domain identification algorithms generally result in better estimations when used as narrow-band identification procedures [36]. This is believed to be due to the exponent in the frequency-domain equations of motion. However, sometimes not all of the target modes lie within a narrow frequency band. For instance, the target modes may span a frequency range of 2 kHz or more. Terms in the resulting equations of motion would vary by a minimum of 8 orders of magnitude, and this could lead to the data being ill-conditioning. In the SSID algorithm, the first estimation procedure, (i.e., the solution of Eq. 3.7) is more prone to ill-

conditioning than is the second step (i.e., the solution of Eq. 3.23) since this step uses accelerance, mobility, and receptance frequency response functions.

In the original formulation of the SSID algorithm [3], all of the measured data was to be processed simultaneously. As just pointed out, this could lead to numerical difficulties. To alleviate this problem, a concept referred to as *band processing* has been employed. The basic idea behind band processing is to work with narrow bands of frequency data individually, and thus avoid some of the conditioning problems. In this manner, experimental data spanning several decades could be processed incrementally, for example 500 Hz at a time, by the SSID algorithm until all of the data has been included in the identification.

The band processing is implemented in the SSID algorithm as follows. First, the experimental data is acquired in the usual manner covering as many decades as necessary to obtain all of the desired modes. The data is then divided into suitable bandwidths of overlapping frequency bands. The overlap allows redundant processing of all of the data; in effect, all of the data is processed twice. Then, the SSID algorithm is used to process each frequency band individually though the solution of the state-space eigenvalue problem, Equation 3.12. From each complex-conjugate pair of eigenvalues, a natural frequency and damping factor can be computed by

$$\zeta_r = \frac{-\Re(\hat{\lambda}_r)}{|\hat{\lambda}_r|} \quad r = 1, \ldots, N_x \tag{5.18}$$

$$\omega_r = \frac{\Im(\hat{\lambda}_r)}{\sqrt{1 - \zeta_r^2}} \quad r = 1, \ldots, N_x \tag{5.19}$$

This step is repeated until all of the frequency bands have been processed.

The next step is to separate the structural roots from the computational, or noise, roots. In this study, four criteria were used to distinguish between the physical modes and computational modes.

1. To graphically aid in the selection process, the estimated natural frequencies and the frequency bands are plotted versus the entire frequency bandwidth. Any estimated frequencies lying outside of the given frequency band are discarded.

2. Roots with negative damping values are discarded.

3. The *modal phase collinearity* (MPC) is computed for each complex-conjugate pair of mode shapes. Those modes with less than a specified MPC value are discarded. The value is dependent upon the level of noise in the measurement signal and the quality of the data.

4. If the root is not repeated in another frequency band, it is discarded. Thus, the need for the overlapping frequency bands. True structural roots will be estimated in multiple frequency bands, while computational ones are highly unlikely to be repeated in multiple frequency bands.

The flow chart in Figure 5.2 summarizes the steps in the band processing procedure.

The modal phase collinearity is an index developed by Juang and Pappa [26] that measures the linear functional relationship between the real and imaginary parts of the mode shape coefficients. It based on the assumption that for lightly damped structures, the estimated mode shapes from Eq. 3.12 should
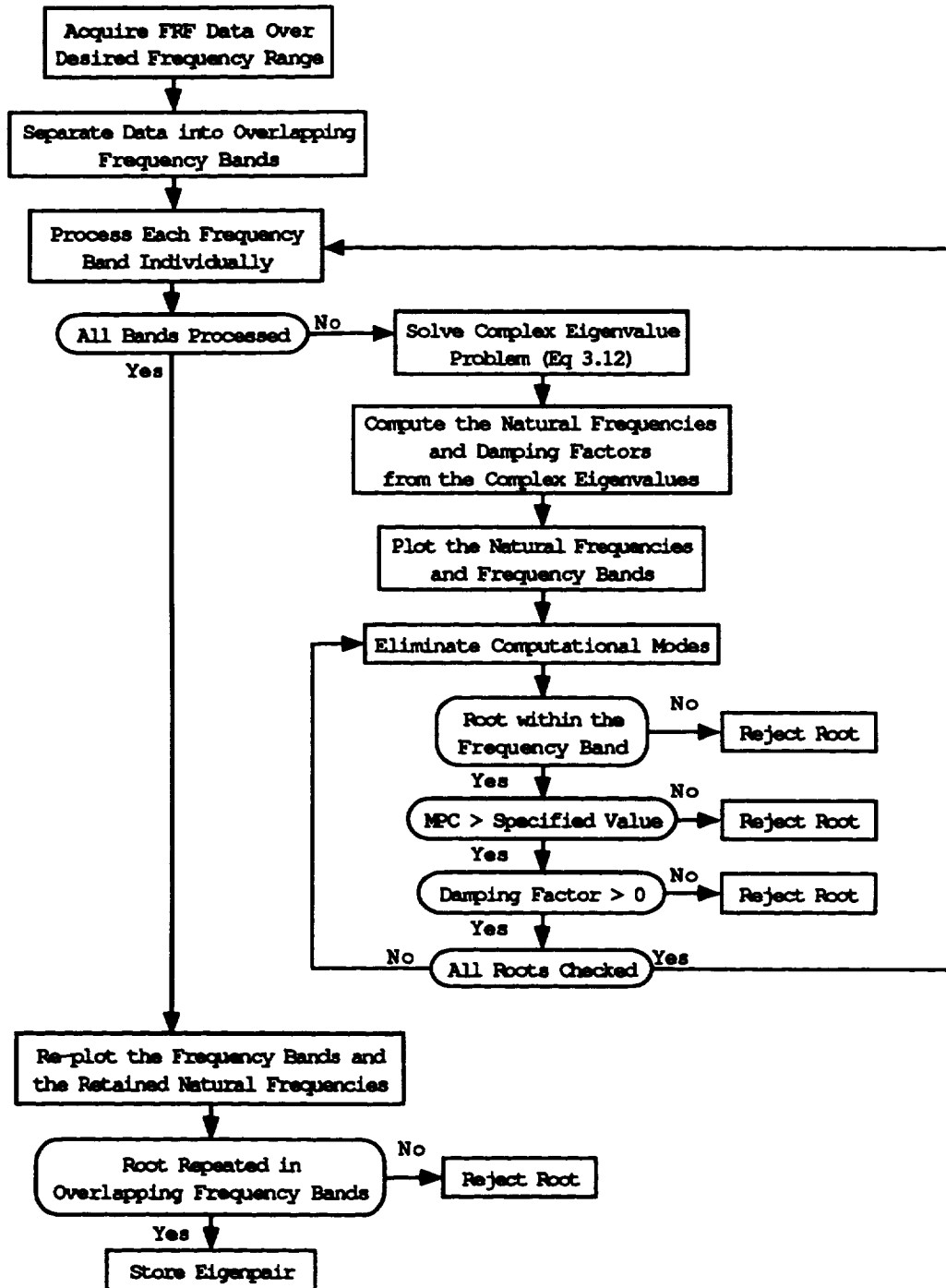
Figure 5.2: Band Processing Flow Chart

be close to normal, that is, the phase angle between the complex coefficients of the same mode shape should either be $0°$ or $\pm 180°$. The MPC index is computed from

$$MPC = \frac{\|\tilde{\theta}_{Re}\|^2 + \tilde{\theta}_{Re}^T \tilde{\theta}_{Im} \frac{2(e^2+1)\sin^2 \alpha - 1}{e}}{\|\tilde{\theta}_{Re}\|^2 + \|\tilde{\theta}_{Im}\|^2} \quad (5.20)$$

where

$$\tilde{\theta} = \hat{\theta} - \frac{\sum_{i=1}^{N_x} \hat{\theta}_i}{N_x} \quad (5.21)$$

$$e = \frac{\|\tilde{\theta}_{Im}\|^2 - \|\tilde{\theta}_{Re}\|^2}{2\tilde{\theta}_{Re}^T \tilde{\theta}_{Im}} \quad (5.22)$$

and

$$\alpha = \arctan(|e| + \sqrt{1 + e^2}) \quad (5.23)$$

and $\| \cdot \|$ represents the Euclidian norm of a vector. An MPC index of near unity indicates a normal mode, while a low index indicates a "noise mode." It should be noted that the MPC assumes real normal mode behavior of the given structure, which is valid for most structures.

Once the computational roots are eliminated and the physical roots stored, the SSID algorithm can proceed to identify the system matrices just as before using the remaining structural roots. Any of the repeated roots and corresponding eigenvectors can be selected from a given frequency band for use in the second part of the SSID algorithm since the eigenvectors are arbitrarily scaled. The scaling used to determine the system matrices arises from the solution for the $\tilde{a}$ coefficients in Equation 3.23.

In the band processing simulations included in the Chapter 6, three different approaches where used to estimate the $\tilde{a}_r$ values. The first was to solve Eq. 3.23 and estimate the $\tilde{a}$ coefficients using all the FRF data in a given

frequency band from which the root was selected. This approach is referred to as BP1 in Section 6.3. The second approach is similar to the first, except that only data near resonance is used in the estimation of the $\bar{a}_r$ values. This approach is referred to as BP2. The third approach is to use the data obtained near the resonances of all of the selected roots simultaneously in Eq. 3.23; this is referred to as BP3. The first two approaches provide a *local* estimation, while the last is a *global* one since data from multiple frequency bands is used simultaneously.

Band processing also holds the potential of significant computational savings. Since the computations are done band by band with a much smaller amount of data, each frequency band could be processed simultaneously on a parallel-processing computer. For tests where a large number of frequency lines are obtained, this could prove to be very cost effective.

## 5.3 Model Order Determination

Perhaps the most important, and most difficult, part of system identification is the determination of the proper model order. For structures with a very high modal density, there are typically more modes in the frequency bandwidth than there are output sensors. For many system identification algorithms, including the SSID algorithm, this poses a serious problem that they are unequipped to handle. In its present formulation, the model order is limited to the number of output sensors. This is the only serious drawback of the method.

For the case when there are more modes present than sensors, the size

of the model must be expanded. An attempt to expand the size of the identification has been developed using pseudo degrees of freedom. The additional degrees of freedom are obtained by stacking the data used in Eq. 3.7 differently. The input frequency spectrum is divided in half, into a low-frequency spectrum and a high-frequency spectrum. In Eq. 3.9, the low-frequency response is then stacked on top of the high-frequency response as shown:

$$
\left[\frac{H_{af}}{j\omega}\right] \equiv
\begin{bmatrix}
\frac{1}{j\omega_1}H_{a_1 f_1}(\omega_1) & \cdots & \frac{1}{j\omega_{N_e}}H_{a_1 f_{N_f}}(\omega_{N_e}) \\
& & \vdots \\
\frac{1}{j\omega_1}H_{a_{N_x} f_1}(\omega_1) & \cdots & \frac{1}{j\omega_{N_e}}H_{a_{N_x} f_{N_f}}(\omega_{N_e}) \\
\frac{1}{j\omega_{N_{e+1}}}H_{a_1 f_1}(\omega_{N_{e+1}}) & \cdots & \frac{1}{j\omega_{N_\omega}}H_{a_1 f_{N_f}}(\omega_{N_e}) \\
& & \vdots \\
\frac{1}{j\omega_{N_{e+1}}}H_{a_{N_x} f_1}(\omega_{N_{e+1}}) & \cdots & \frac{1}{j\omega_{N_\omega}}H_{a_{N_x} f_{N_f}}(\omega_{N_\omega})
\end{bmatrix}
\tag{5.24}
$$

where $N_e = \frac{N_\omega}{2}$. Stacking the data in this manner essentially doubles the order of the model.

Thus, although the lower partition of data is measured at the same physical coordinates as the upper partition of lower-frequency data, the system modes that contribute to the two sets of data are not identical. The lower partition is referred to as data from pseudo degrees of freedom. After Eq. 3.7 is solved using the expanded model, the state-space eigenvalue problem, Eq. 3.12, is solved. However, the details of the second step of the algorithm, the identification of the system matrices, have yet to be resolved. Further research is needed in this area. Section 6.4 presents results obtained by processing through the first step of the SSID algorithm employing pseudo degrees of freedom.

# Chapter 6

# Numerical Simulations

This chapter describes the numerical simulations used to study the Substructure System Identification algorithm. The simulations presented here focus on model-reduction and the SSID algorithm's ability to identify a valid reduced-order structural model. This is a problem that should be addressed by all system identification algorithms, since spatial truncation is inevitable in test situations. A proof-of-concept example and examples using lumped-parameter models are given in References [3, 63].

In Section 6.1, a description of the analytical model and an overview of the simulations are given. The results from several simulations are presented in Section 6.2. Results from simulations employing band processing are included in Section 6.3. Section 6.4 presents the results when the model order is expanded by the introduction of pseudo degrees of freedom. The SSID reduced-order models are compared to other TAMs in Section 6.5.

## 6.1 Model Description and Overview of Simulations

The analytical model used in the simulations is a 52-DOF FEM of the "Payload Simulator" in the Structural Dynamics Laboratory at The University of Texas at Austin. This is a model of the structure that was used in a previous study to measure the reaction forces at the substructure-test stand interface

locations [64]. The physical structure consists of two 60-in.-long aluminum box beams connected by two 20-in. cross-beams at either end.

The FEM consists of 18 nodes and 20 beam elements and is illustrated in Figure 6.1. The physical structure undergoes motion primarily in the Z direction, so all of the X and Y translations and Z rotations are constrained in the finite element model. The two cross-beams at each end of the physical structure are connected by very short rods, and were originally modeled with NASTRAN ROD elements. However, this proved to be too stiff, so the rod elements were replaced with multi-point constraints constraining the Z-translational degree of freedom of nodes 9 and 10 to nodes 18 and 17, respectively. The payload simulator is supported by soft springs at nodes 11, 13, 14, and 16 to simulate a bungee cord suspension system. Table 6.1 lists the undamped natural frequencies of the finite element model. The three lowest modes are the rigid body modes of the structure.

The three interface degrees of freedom for this structure are the Z-translational degrees of freedom at nodes 4, 8, and 18. For the simulations presented in this section active excitation was used at all of the interface degrees of freedom, that is, no reaction forces were measured

All of the simulations were performed in MATLAB© [65] running on a workstation. The mass and stiffness matrices were generated by and output from NASTRAN, and were then converted to a binary "MAT-file" readable by MATLAB©. To simulate viscous damping in the structure, modal damping at a level of 2% was added to all of the modes to obtain a physical damping matrix for the finite element model.

Table 6.1: Undamped Natural Frequencies of the Payload Simulator

| Number | Frequency (Hz) | Number | Frequency (Hz) |
|--------|---------------|--------|---------------|
| 1* | 1.1564 | 27 | 1690.4 |
| 2* | 6.0642 | 28 | 1702.2 |
| 3* | 10.783 | 29* | 2029.1 |
| 4* | 18.127 | 30* | 2031.2 |
| 5* | 109.49 | 31 | 2079.9 |
| 6* | 127.14 | 32 | 2104.3 |
| 7* | 137.82 | 33 | 2272.3 |
| 8* | 156.87 | 34 | 2289.9 |
| 9* | 297.66 | 35 | 2746.6 |
| 10* | 304.47 | 36 | 2750.7 |
| 11 | 512.54 | 37 | 2840.2 |
| 12 | 521.24 | 38 | 2842.6 |
| 13 | 567.89 | 39 | 2943.9 |
| 14 | 570.46 | 40 | 2945.1 |
| 15 | 570.46 | 41 | 3403.3 |
| 16 | 583.43 | 42 | 3406.0 |
| 17* | 606.45 | 43 | 5017.1 |
| 18* | 631.08 | 44 | 5018.5 |
| 19 | 1073.0 | 45 | 7060.1 |
| 20 | 1078.6 | 46 | 7061.7 |
| 21* | 1190.4 | 47 | 8887.0 |
| 22* | 1193.3 | 48 | 8888.5 |
| 23 | 1341.5 | 49 | 11972. |
| 24 | 1342.4 | 50 | 11973. |
| 25 | 1342.4 | 51 | 14727. |
| 26 | 1342.6 | 52 | 14727. |

*Target Modes—modes dominated by Z-translations

Figure 6.1: Payload Simulator Finite Element Model

To generate the "experimental data" used in the simulations, the fre-

quency response functions were generated by solving Eq. 3.6 for $A(\omega_k)$ given $M$,

$C$, $K$, and $F(\omega_k)$. Except as noted, the input forcing function at each frequency

$\omega_k$ consisted of three independent unit forces applied in the Z-translational di-

rection at nodes 4, 8, and 18 respectively. This data was then used as the input

to the SSID algorithm to identify $M$, $C$, and $K$ from the simulated measured

acceleration responses, $A(\omega_k)$, and force inputs, $F(\omega_k)$. The input data used

for the simulations presented in sections 6.2.4 and 6.3 contains additive noise

while the input data for the other simulations is noise-free.

## 6.2 Simulation Results

### 6.2.1 Identification of the Full-Order Model

The first simulation demonstrates the algorithm's ability to identify structural models without any corrupting effects of noise, or of frequency truncation or spatial truncation. In order to identify all 52 modes, it was necessary to apply both forces and moments since the payload simulator is capable of deforming in translational and rotational directions. The inputs were $F_z$ at node 4, $M_x$ at node 17, and $M_y$ at 18. The identification of the full-order model was based on 128 evenly spaced frequency lines ranging from 1 Hz to 15000 Hz. Computer memory constraints prohibited a finer frequency resolution.

The results of the full-order identification are shown in Figs. 6.2–6.6. The individual entries of the estimated matrices were compared to those of the original matrices and the results are shown in Figs. 6.2–6.4. The SSID algorithm successfully identified the mass, damping, and stiffness matrices of the original structure to within 0.25%. The undamped natural frequencies were computed from the identified mass and stiffness matrices, and all 52 natural frequencies of the original structure were identified to within 8-digit accuracy. Figure 6.5 is a comparison between the exact drive point FRF at node 4 and one synthesized using the resulting identified $M$, $C$, and $K$ matrices; Fig. 6.6 shows the difference between the two FRFs.

### 6.2.2 Identification of Reduced-Order Models

In the previous simulation, the SSID algorithm was successfully able to identify the system matrices of the full-order 52 degree of freedom model

when all of the modes of the system were included. In a test environment, this would require response measurements at all 52 degrees of freedom, including the rotational degrees of freedom. However, it is impractical and impossible to measure the response of all of the degrees of freedom of a continuous structure. Therefore, spatial truncation is inevitable.

The following simulations demonstrate the ability of the SSID algorithm to predict the dynamic characteristics of a structure when only a limited number of accelerometers, or other appropriate output devices, are available. The resulting identified model is referred to as a reduced-order model. Three different reduced-order models where used in the simulations. The number of degrees of freedom, or measurement locations, used for the reduced-order models was 10, 12 and 16 degrees of freedom.

It is desired that the reduced-order models be able to represent the target modes of interest. The target modes to be identified are the rigid-body modes and other "global" modes of the structure (i.e., modes where localized bending predominates or where rotational DOFs predominate are excluded). These modes are indicated by an asterisk in Table 6.1. Note that the target modes are not just the lowest consecutive modes of the system, but are modes which are spaced throughout the spectrum.

The Effective Interface method [66] was used for the process of selecting which degrees of freedom were to be "measured," or retained, during the numerical simulations. The Effective Interface Method is an iterative sensor placement process that maximizes the observability of the target modes by maximizing the determinant of the Fisher information matrix. The Fisher

information matrix is formed by

$$F = \Phi_{ta}^T \Phi_{ta} \qquad (6.1)$$

where $\Phi_{ta}$ are the target modes partitioned to the retained degrees of freedom. The method examines the effect that the removal of each degree of freedom would have on the Fisher information matrix and removes one degree of freedom at a time. Table 6.2 summarizes the nodes selected by the Effective Interface Method for use as response locations for the three different reduced-order model sizes. In each case, the Effective Interface Method selected the Z-translational degree of freedom at the nodes listed in Table 6.2.

Table 6.2: Reduced-Order Model Measurement Sensor Locations

| Model Size | Measurement Locations |
|---|---|
| 10 | 1, 2, 3, 4, 5, 6, 7, 8, 17, 18 |
| 12 | 1, 4, 5, 8, 11, 12, 13, 14, 15, 16, 17, 18 |
| 16 | 1, 2, 3, 4, 5, 6, 7, 8, 11, 12, 13, 14, 15, 16, 17, 18 |

## 6.2.3 Effect of Input Frequency Spectrum on the SSID Algorithm

For each of the reduced-order models, three different input frequency ranges were used to generate test data. This was done to determine how the SSID algorithm handles residual information. As was mentioned previously, the identified model depends on the frequency range. For each model size, better results can be obtained by adjusting the frequency range until the best frequency range is found. In a test environment, the "best" frequency range is unknown, so three input frequency ranges were arbitrarily selected. The different frequency ranges are summarized in Table 6.3. For each frequency

range, the frequency lines are equally spaced between the minimum frequency and the maximum frequency. The third input frequency range uses 1024 frequency lines instead of 512 since the frequency spacing using 512 would have been approximately 4 Hz and was considered too large to identify modes space 2–3 Hz apart, which modes 21–22 and 29–30 are.

Table 6.3: Input Frequency Spectrums

| Number | Minimum Frequency (Hz) | Maximum Frequency (Hz) | Number of Frequency Lines | $\Delta f$ (Hz) |
|--------|------------------------|------------------------|---------------------------|-----------------|
| 1 | 1 | 300 | 512 | 0.584 |
| 2 | 1 | 650 | 512 | 1.267 |
| 3 | 1 | 2100 | 1024 | 2.050 |

Table 6.4 compares the estimated undamped natural frequencies of the 10-DOF model for the different input frequency ranges. The estimated damping factors are given in Table 6.5. The damping factors are computed from the solution of the state space eigenproblem of Eq. 3.12. For the 10-DOF model, the best results are obtained for the frequency range of 1–300 Hz, which encompasses the first nine modes of the original system. As the maximum frequency is increased to include more modes, the resulting models tend to overestimate the natural frequencies and do a much poorer job estimating the damping factors, especially the lowest one.

The resulting drive-point FRFs at node 4 from each 10-DOF model are shown in Figure 6.7. For the input frequency range of 1–300 Hz, the estimated response is almost identical to that of the response of the original 52 degree of freedom model. The response of the identified model corresponding to the other two input frequency ranges overestimates the response near the

first mode. This is presumably caused by response of the higher modes, which the 10-DOF model is unable to represent. The 10-DOF model is trying to "fit" the response of the higher modes and thus overestimates near the first mode. Additionally, these two models do not estimate the amplitude of the true response near the resonances and anti-resonances as well as the first case does.

In the FRF comparisons included in this report, the damping matrix used to form the synthesized FRFs was identified from the appropriate partition of $A_s$ in Equation 3.15. Another damping matrix could also be formed by using the estimated damping factors and the real normal modes from the identified mass and stiffness matrices. For a given identified model, this "modal" damping matrix generally overestimated the response at high frequencies while the identified damping matrix from Eq. 3.15 underestimates the response. A representative example is shown in Figure 6.8.

To determine how the identified eigenvectors relate to the original ones, the Modal Assurance Criteria (MAC) [5] was computed. The MAC is not a true orthogonality check but is a scalar quantity that indicates the degree of independence between two mode shapes. The first 30 exact eigenvectors were partitioned to the retained degrees of freedom and compared to the eigenvectors obtained from the eigensolution of the identified mass and stiffness matrices. For all three 10-DOF models, the identified eigenvectors had MAC values of 0.99 or greater for the corresponding target mode and values of less than 0.05 for the remaining eigenvectors.

The estimated undamped natural frequencies and damping factors

Table 6.4: Estimated Natural Frequencies — 10-DOF Model vs Input Frequency Spectrum

| Exact Freq. (Hz) | Fmax=300 Hz | | Fmax=650 Hz | | Fmax=2100 Hz | |
|---|---|---|---|---|---|---|
| | Freq. (Hz) | Percent Error | Freq. (Hz) | Percent Error | Freq. (Hz) | Percent Error |
| 1.1564 | 1.1552 | 1.116e–01 | 1.1301 | 2.281e+00 | 1.1453 | 9.633e–01 |
| 606.42 | 6.0647 | 6.755e–03 | 6.0648 | 9.276e–03 | 6.0786 | 2.359e–01 |
| 10.783 | 10.784 | 7.202e–03 | 10.956 | 1.604e+00 | 10.924 | 1.305e+00 |
| 18.127 | 18.126 | 5.608e–03 | 18.133 | 3.268e–02 | 18.462 | 1.850e+00 |
| 109.49 | 109.49 | 3.624e–03 | 109.60 | 1.032e–01 | 109.44 | 4.352e–02 |
| 127.14 | 127.12 | 1.203e–02 | 127.02 | 9.223e–02 | 128.04 | 7.052e–01 |
| 137.82 | 137.83 | 4.228e–03 | 137.84 | 1.609e–02 | 137.73 | 6.875e–02 |
| 156.87 | 156.87 | 1.263e–03 | 156.78 | 5.782e–02 | 156.88 | 7.647e–03 |
| 297.66 | 297.52 | 4.736e–02 | 296.70 | 3.230e–01 | 308.08 | 3.502e+00 |
| 304.47 | 303.74 | 2.376e–01 | 304.12 | 1.127e–01 | 309.89 | 1.781e+00 |

Table 6.5: Estimated Damping Factors — 10-DOF Model vs Input Frequency Spectrum

| Exact Damp. Ratio | Fmax=300 Hz | | Fmax=650 Hz | | Fmax=2100 Hz | |
|---|---|---|---|---|---|---|
| | Damp. Ratio | Percent Error | Damp. Ratio | Percent Error | Damp. Ratio | Percent Error |
| 0.02 | 0.01974 | 1.291e+00 | 0.02674 | 3.369e+01 | 0.04127 | 1.063e+02 |
| 0.02 | 0.01987 | 6.368e–01 | 0.01902 | 4.921e+00 | 0.09362 | 3.681e+02 |
| 0.02 | 0.01895 | 5.240e+00 | 0.01163 | 4.183e+01 | 0.06398 | 2.199e+02 |
| 0.02 | 0.01971 | 1.469e+00 | 0.01919 | 4.028e+00 | 0.07168 | 2.584e+02 |
| 0.02 | 0.02000 | 1.109e–02 | 0.02010 | 5.074e–01 | 0.02017 | 8.340e–01 |
| 0.02 | 0.01992 | 3.767e–01 | 0.01951 | 2.458e+00 | 0.02673 | 3.367e+01 |
| 0.02 | 0.02000 | 1.677e–02 | 0.01992 | 3.855e–01 | 0.02126 | 6.288e+00 |
| 0.02 | 0.01997 | 1.290e–01 | 0.02034 | 1.724e+00 | 0.02180 | 9.002e+00 |
| 0.02 | 0.01994 | 2.949e–01 | 0.02227 | 1.133e+01 | 0.00683 | 6.587e+01 |
| 0.02 | 0.01970 | 1.474e+00 | 0.02033 | 1.644e+00 | 0.00714 | 6.432e+01 |

of the 12-DOF model for the different input frequency ranges are listed in Tables 6.6 and 6.7. The corresponding FRFs are shown in Figure 6.9. For the 12-DOF model, the best results are obtained for the frequency ranges 1–300 Hz and 1–650 Hz. Note that the model corresponding to the input frequency range of 1–300 Hz was able to correctly estimate the system's response for modes 11 and 12 even though they are above the 300 Hz upper limit of the FRF data. The synthesized FRFs for these two models match very closely to those of the exact response, except near the response of the 12th mode. Here, the model corresponding to the first frequency range underestimates the response while the model corresponding to the 2nd input frequency range overestimates the magnitude of the response.

The identified model corresponding to the third input frequency range, which includes all 16 target modes, overestimates the 11th and 12th natural frequencies and also does a much poorer job of estimating the damping factors. Again, the response of this model overestimates the response around the first mode and does a much poorer job of estimating response near the resonances and anti-resonances than do the models corresponding to the first two input frequency ranges. MAC values were also computed for the 12-DOF models with the same results as before, that is, near-perfect correlation between the identified modes and the target FEM modes.

The estimated undamped natural frequencies and damping factors of the 16-DOF model for the different input frequency spectrums are listed in Tables 6.8 and 6.9, and the corresponding FRFs are shown in Figure 6.10. For the first 10 natural frequencies and damping factors, the identified model corre-

Table 6.6: Estimated Natural Frequencies — 12-DOF Model vs Input Frequency Spectrum

| Exact | Fmax=300 Hz | | Fmax=650 Hz | | Fmax=2100 Hz | |
|---|---|---|---|---|---|---|
| Freq. (Hz) | Freq. (Hz) | Percent Error | Freq. (Hz) | Percent Error | Freq. (Hz) | Percent Error |
| 1.1564 | 1.1564 | 1.465e–03 | 1.1563 | 1.560e–02 | 1.1577 | 1.073e–01 |
| 6.0642 | 6.0642 | 3.454e–05 | 6.0643 | 6.787e–04 | 6.0620 | 3.767e–02 |
| 10.783 | 10.783 | 8.332e–06 | 10.783 | 2.530e–03 | 10.785 | 1.427e–02 |
| 18.127 | 18.127 | 1.780e–06 | 18.127 | 2.632e–03 | 18.112 | 7.970e–02 |
| 109.49 | 109.49 | 5.694e–04 | 109.49 | 2.860e–03 | 109.54 | 4.366e–02 |
| 127.14 | 127.14 | 1.377e–04 | 127.19 | 4.276e–02 | 127.30 | 1.261e–01 |
| 137.82 | 137.82 | 7.153e–05 | 137.82 | 7.165e–04 | 137.83 | 5.248e–03 |
| 156.87 | 156.86 | 8.364e–05 | 156.86 | 7.596e–03 | 156.87 | 4.080e–03 |
| 297.66 | 296.64 | 6.828e–03 | 296.99 | 2.239e–01 | 299.29 | 5.461e–01 |
| 304.47 | 304.58 | 3.859e–02 | 304.41 | 1.833e–02 | 305.56 | 3.598e–01 |
| 606.45 | 602.08 | 7.211e–01 | 605.93 | 8.683e–02 | 616.79 | 1.704e+00 |
| 631.08 | 614.86 | 2.570e+00 | 609.92 | 3.353e+00 | 643.57 | 1.979e+00 |

sponding to the 1–300 Hz input frequency range performed the best. However, this model does not estimate the last four natural frequencies and damping values very well. As shown by the MAC values in Table 6.10, the last two modes do not correspond to the any of the target modes. The poor estimation of the higher frequencies is also indicated in the corresponding synthesized FRF in Figure 6.10.

The 16-DOF model corresponding to the second input frequency spectrum estimates the first 12 frequencies very well. However, this model also identifies a frequency at 582.31 Hz, which agrees well with the 15th mode of the original 52 degrees of freedom model. This mode shape is similar to the 2nd anti-symmetric bending mode of the structure, mode 9, except that the maximum displacement in the mode shape occurs in the X-rotational degree of

Table 6.7: Estimated Damping Factors — 12-DOF Model vs Input Frequency Spectrum

| Exact | Fmax=300 Hz | | Fmax=650 Hz | | Fmax=2100 Hz | |
|---|---|---|---|---|---|---|
| Damp. Ratio | Damp. Ratio | Percent Error | Damp. Ratio | Percent Error | Damp. Ratio | Percent Error |
| 0.02 | 0.02000 | 9.909e-03 | 0.02006 | 2.965e-01 | 0.01782 | 1.088e+01 |
| 0.02 | 0.02000 | 2.023e-03 | 0.01995 | 2.550e-01 | 0.01854 | 7.309e+00 |
| 0.02 | 0.02000 | 4.948e-03 | 0.02025 | 1.257e+00 | 0.01558 | 2.209e+01 |
| 0.02 | 0.02000 | 9.197e-04 | 0.01936 | 3.193e+00 | 0.01929 | 3.524e+00 |
| 0.02 | 0.02000 | 1.234e-02 | 0.02003 | 1.563e-01 | 0.01985 | 7.721e-01 |
| 0.02 | 0.02000 | 6.847e-03 | 0.02012 | 6.068e-01 | 0.01855 | 7.255e+00 |
| 0.02 | 0.02000 | 1.396e-03 | 0.01999 | 4.555e-02 | 0.01982 | 8.789e-01 |
| 0.02 | 0.02000 | 5.182e-03 | 0.02000 | 4.095e-03 | 0.02000 | 5.835e-03 |
| 0.02 | 0.01999 | 7.062e-02 | 0.01982 | 8.829e-01 | 0.03171 | 5.855e+01 |
| 0.02 | 0.02004 | 2.125e-01 | 0.01989 | 5.649e-01 | 0.02753 | 3.764e+01 |
| 0.02 | 0.02003 | 1.565e-01 | 0.01979 | 1.029e+00 | 0.01807 | 9.641e+00 |
| 0.02 | 0.02003 | 1.735e-01 | 0.02774 | 3.869e+01 | 0.02286 | 1.432e+01 |

freedom at nodes 9, 10, 17, and 18. The inclusion of this mode is the suspected reason for the error in the estimation of the last 4 natural frequencies and for the error in the synthesized FRF for frequencies greater than 700 Hz.

The identified model corresponding to the input frequency range of 1-2100 Hz represents the dynamic characteristics of the original structure the best overall. All 16 natural frequencies are identified to within 1.0% and all of the MAC values are near unity for the corresponding target modes and less than 0.05 for the remaining ones. The synthesized FRF matches the exact response almost exactly, except at very high frequencies, where it underestimates the magnitude of the true response.

As indicated by the preceding simulations, the SSID-identified ma-

trices are frequency-dependent. The best estimation of a given model order is when the input frequency range contains only the corresponding number of modes. For this reason, in the remaining simulations, the 10-DOF model was estimated using the first input frequency spectrum, the second input frequency range was used to estimate the 12-DOF model, and the 1-2100 Hz input frequency spectrum was used to estimate the 16-DOF model.

Table 6.8: Estimated Natural Frequencies — 16-DOF Model vs Input Frequency Spectrum

| Exact Freq. (Hz) | Fmax=300 Hz | | Fmax=650 Hz | | Fmax=2100 Hz | |
|---|---|---|---|---|---|---|
| | Freq. (Hz) | Percent Error | Freq. (Hz) | Percent Error | Freq. (Hz) | Percent Error |
| 1.1564 | 1.1564 | 5.902e–05 | 1.1564 | 6.472e–03 | 1.1507 | 4.948e–01 |
| 6.0642 | 6.0642 | 3.468e–06 | 6.0642 | 4.260e–06 | 6.0628 | 2.430e–02 |
| 10.783 | 10.783 | 3.174e–08 | 10.794 | 1.013e–01 | 10.807 | 2.165e–01 |
| 18.127 | 18.127 | 3.659e–08 | 18.124 | 1.280e–02 | 18.115 | 6.439e–02 |
| 109.49 | 109.49 | 1.992e–05 | 109.48 | 5.737e–03 | 109.49 | 1.539e–03 |
| 127.14 | 127.14 | 1.238e–07 | 127.16 | 1.745e–02 | 127.15 | 7.669e–03 |
| 137.82 | 137.82 | 2.793e–05 | 137.82 | 2.366e–04 | 137.82 | 2.866e–03 |
| 156.87 | 156.87 | 4.226e–05 | 156.86 | 4.682e–03 | 156.86 | 5.341e–03 |
| 297.66 | 297.66 | 1.745e–06 | 296.70 | 3.218e–01 | 297.61 | 1.796e–02 |
| 304.47 | 304.47 | 2.041e–05 | 304.47 | 7.440e–04 | 304.41 | 1.745e–02 |
| 606.45 | 606.15 | 5.092e–02 | 582.31 | — | 606.24 | 3.595e–02 |
| 631.08 | 613.54 | 2.779e+00 | 606.53 | 1.319e–02 | 626.89 | 6.648e–01 |
| 1190.4 | 1047.1 | 1.204e+01 | 625.76 | 8.430e–01 | 1189.4 | 8.538e–02 |
| 1193.3 | 1159.3 | 2.852e+00 | 1023.9 | 1.399e+01 | 1192.3 | 8.922e–02 |
| 2029.1 | 1526.7 | 2.476e+01 | 1154.6 | 3.243e+00 | 2017.0 | 5.990e–01 |
| 2031.2 | 1682.3 | 1.718e+01 | 1773.3 | 1.261e+01 | 2017.6 | 6.686e–01 |

For each of the reduced-order models, a "pseudo" drive-point FRF was estimated and compared to the original model. Using the identified system matrices, a drive-point FRF was estimated even though no force was actually

Table 6.9: Estimated Damping Factors — 16-DOF Model vs Input Frequency Spectrum

| Exact Damp. Ratio | Fmax=300 Hz | | Fmax=650 Hz | | Fmax=2100 Hz | |
|---|---|---|---|---|---|---|
| | Damp. Ratio | Percent Error | Damp. Ratio | Percent Error | Damp. Ratio | Percent Error |
| 0.02 | 0.02000 | 4.237e-04 | 0.01997 | 1.263e-01 | 0.01980 | 1.022e+00 |
| 0.02 | 0.02000 | 4.263e-05 | 0.02000 | 7.409e-03 | 0.02104 | 5.179e+00 |
| 0.02 | 0.02000 | 3.668e-06 | 0.01859 | 7.034e+00 | 0.01824 | 8.789e+00 |
| 0.02 | 0.02000 | 6.994e-06 | 0.01893 | 5.333e+00 | 0.02055 | 2.754e+00 |
| 0.02 | 0.02000 | 7.646e-04 | 0.01999 | 6.403e-02 | 0.02009 | 4.696e-01 |
| 0.02 | 0.02000 | 3.306e-06 | 0.01884 | 5.778e+00 | 0.01882 | 5.911e+00 |
| 0.02 | 0.02000 | 8.368e-05 | 0.02000 | 4.057e-03 | 0.01993 | 3.678e-01 |
| 0.02 | 0.02000 | 5.035e-04 | 0.01999 | 6.897e-02 | 0.01993 | 3.481e-01 |
| 0.02 | 0.02000 | 1.471e-04 | 0.01966 | 1.682e+00 | 0.02157 | 7.847e+00 |
| 0.02 | 0.02000 | 2.141e-04 | 0.02000 | 1.538e-03 | 0.01980 | 9.997e-01 |
| 0.02 | 0.02000 | 2.160e-02 | 0.02089 | 4.473e+00 | 0.02018 | 8.870e-01 |
| 0.02 | 0.01996 | 2.145e-01 | 0.02002 | 1.099e-01 | 0.02593 | 2.964e+01 |
| 0.02 | 0.01775 | 1.126e+01 | 0.02698 | 3.492e+01 | 0.02031 | 1.552e+00 |
| 0.02 | 0.02034 | 1.185e+00 | 0.02041 | 2.049e+00 | 0.01923 | 3.830e+00 |
| 0.02 | 0.02135 | 6.742e+00 | 0.02017 | 8.743e-01 | 0.01549 | 2.257e+01 |
| 0.02 | 0.02094 | 4.685e+00 | 0.02716 | 3.580e+01 | 0.01571 | 2.145e+01 |

Table 6.10: Maximum MAC Values for 16-DOF Model vs Input Frequency Spectrum

| TAM Mode | Fmax=300 Hz | | Fmax=650 Hz | | Fmax=2100 Hz | |
|---|---|---|---|---|---|---|
| | FEM Mode | Max MAC | FEM Mode | Max MAC | FEM Mode | Max MAC |
| 1 | 1 | 1.0000 | 1 | 1.0000 | 1 | 1.0000 |
| 2 | 2 | 1.0000 | 2 | 1.0000 | 2 | 1.0000 |
| 3 | 3 | 1.0000 | 3 | 1.0000 | 3 | 1.0000 |
| 4 | 4 | 1.0000 | 4 | 1.0000 | 4 | 1.0000 |
| 5 | 5 | 1.0000 | 5 | 1.0000 | 5 | 1.0000 |
| 6 | 6 | 1.0000 | 6 | 1.0000 | 6 | 1.0000 |
| 7 | 7 | 1.0000 | 7 | 1.0000 | 7 | 1.0000 |
| 8 | 8 | 1.0000 | 8 | 1.0000 | 8 | 1.0000 |
| 9 | 9 | 1.0000 | 9 | 1.0000 | 9 | 1.0000 |
| 10 | 10 | 1.0000 | 10 | 1.0000 | 10 | 1.0000 |
| 11 | 18 | 0.9987 | 15 | 0.8721 | 17 | 1.0000 |
| 12 | 17 | 0.9344 | 17 | 1.0000 | 18 | 0.9970 |
| 13 | 20 | 0.6239 | 18 | 0.9552 | 21 | 0.9999 |
| 14 | 21 | 0.6639 | 28 | 0.6244 | 22 | 0.9999 |
| 15 | 32 | 0.7196 | 21 | 0.8891 | 30 | 0.9999 |
| 16 | 27 | 0.6063 | 27 | 0.3830 | 29 | 0.9992 |

applied at the degree of freedom during the identification of the model. The results of the comparisons are shown in Figures 6.11–6.13. As can been seen, good agreement is obtained between the estimated and the exact pseudo drive-point FRF. This suggests that interface information could possibly be obtained without applying a force or measuring a reaction force at the interface degrees of freedom.

### 6.2.4  Effect of Noise on the SSID Algorithm

In the simulations presented in the Section 6.2.1 through 6.2.3, the exact 52-DOF FRF data was used. The only "errors" that were introduced in the SSID processing of the exact FRF data was due to spatial and/or frequency truncation of the measured data. However, measured FRF data always contains some type of random error, or noise. The noise, for example, could be due to transducer error, signal processing and conditioning error, or other errors and uncertainties present in the measurement process. Therefore, for an identification algorithm to be applicable to test data, it must be robust enough to handle less than perfect data. The main concern of the simulations presented in this section is the numerical stability of the SSID algorithm in the presence of noise.

The noise added to the simulated FRF data was uniformly distributed, pure random, and zero mean. A noise level of 2% was used in the simulations in this study. The noise level is the percent of the root-mean-square (RMS) value of the random noise to the RMS value of the noise free-signal. Acceleration is usually measured as the output of the structure, so the magnitude of the noise

is proportional to the magnitude of each accelerance FRF spectrum, not the receptance frequency response. A random phase error was also introduced; the maximum error on the phase was 2°. A typical "measured" response is shown in Figure 6.14. To reduce the effect of the noise, signal averaging was used, just as averaging would be employed in an actual test. The measured FRFs were averaged over 40 samples.

The three least squares methods discussed in the previous Chapter were used to solve the over-determined system of equations, Eq. 3.7. No acceptable solution for any of the reduced-order models was ever obtained using the ordinary least squares method. The standard MATLAB least squares solver, which performs a Q-R decomposition, was used to solve the over-determined system of equations. The resulting identified system matrices were not positive definite, and typically yielded complex estimates for the undamped natural frequencies. Increasing the number of averages did not significantly improve the resulting solution. Figure 6.15 is a representative least squares solution and estimation of the drive-point FRF. This result indicates that in the implementation of the SSID algorithm for use in test environments, a TLS solver will be necessary.

A comparison of the estimations resulting from the different methods of solution for the 10-DOF model are shown Tables 6.11 and 6.12. Except for the first and the last mode, both methods of solution predict the undamped natural frequencies to within 1%. The STLS method gives slightly more accurate results, which is to be expected. For the 1st mode, which is where the noise affects the signal the most, the STLS estimation is much more accurate than

the TLS estimation. However, the STLS method does not accurately estimate the damping factors for the last three modes.

The corresponding FRFs are shown in Figure 6.16. Again, both methods of solution predict the response of the structure very well. The STLS method performs better than the TLS method in the low frequency response, while the TLS solution is more accurate than the STLS solution at higher frequencies. The TLS solution also overestimates the response near resonance for modes 4 and 5.

Table 6.11: Estimated Natural Frequencies — 10-DOF Model vs Solution Method

| Exact Freq. (Hz) | Noise Free | | TLS | | STLS | |
|---|---|---|---|---|---|---|
| | Freq. (Hz) | Percent Error | Freq. (Hz) | Percent Error | Freq. (Hz) | Percent Error |
| 1.1564 | 1.1552 | 1.116e–01 | 1.3706 | 1.852e+01 | 1.1795 | 1.989e+00 |
| 6.0642 | 6.0647 | 6.755e–03 | 6.0654 | 1.969e–02 | 6.0633 | 1.639e–02 |
| 10.783 | 10.784 | 7.202e–03 | 10.799 | 1.434e–01 | 10.780 | 2.786e–02 |
| 18.127 | 18.126 | 5.608e–03 | 18.139 | 6.756e–02 | 18.118 | 4.946e–02 |
| 109.49 | 109.49 | 3.624e–03 | 109.54 | 4.068e–02 | 109.55 | 5.016e–02 |
| 127.14 | 127.12 | 1.203e–02 | 127.01 | 1.040e–01 | 127.05 | 7.012e–02 |
| 137.82 | 137.83 | 4.228e–03 | 137.85 | 2.018e–02 | 137.85 | 1.861e–02 |
| 156.87 | 156.87 | 1.263e–03 | 157.19 | 2.003e–01 | 157.33 | 2.947e–01 |
| 297.66 | 297.52 | 4.736e–02 | 299.96 | 7.711e–01 | 299.45 | 6.012e–01 |
| 304.47 | 303.74 | 2.376e–01 | 312.42 | 2.612e+00 | 315.90 | 3.754e+00 |

Comparisons of the results for the 12-DOF model are shown Tables 6.13 and 6.14 and in Figure 6.17. The same general trend is observed in this case as for the 10-DOF model. The STLS method provides a slightly better estimation of the dynamic characteristics of the original structure than the TLS solution for the low-frequency response. Both solutions overestimate

Table 6.12: Estimated Damping Factors — 10-DOF Model vs Solution Method

| Exact | Noise Free | | TLS | | STLS | |
|---|---|---|---|---|---|---|
| Damp. Ratio | Damp. Ratio | Percent Error | Damp. Ratio | Percent Error | Damp. Ratio | Percent Error |
| 0.02 | 0.01974 | 1.291e+00 | 0.01700 | 1.502e+01 | 0.02018 | 9.057e-01 |
| 0.02 | 0.01987 | 6.368e-01 | 0.01990 | 4.851e-01 | 0.01994 | 3.019e-01 |
| 0.02 | 0.01895 | 5.240e+00 | 0.01895 | 5.226e+00 | 0.01918 | 4.099e+00 |
| 0.02 | 0.01971 | 1.469e+00 | 0.01967 | 1.645e+00 | 0.01978 | 1.096e+00 |
| 0.02 | 0.02000 | 1.109e-02 | 0.01993 | 3.698e-01 | 0.01899 | 5.025e+00 |
| 0.02 | 0.01992 | 3.767e-01 | 0.01876 | 6.221e+00 | 0.01921 | 3.956e+00 |
| 0.02 | 0.02000 | 1.677e-02 | 0.02057 | 2.860e+00 | 0.01988 | 5.937e-01 |
| 0.02 | 0.01997 | 1.290e-01 | 0.02319 | 1.595e+01 | 0.02265 | 1.326e+01 |
| 0.02 | 0.01994 | 2.949e-01 | 0.01963 | 1.841e+00 | 0.01451 | 2.744e+01 |
| 0.02 | 0.01970 | 1.474e+00 | 0.03474 | 73.68e+01 | 0.03621 | 8.103e+01 |

the response of the structure for frequencies greater than the input frequency range of 1–650 Hz.

For the case of the 16-DOF model in the presence of noise, none of the three solution methods was able to provide an acceptable solution. The identified system matrices were not positive definite for any of the three methods of solution. The erroneous solutions are more than likely due to the power to which the additive noise terms are raised in the frequency-domain equations of motion. This unsuccessful identification provides support to the claim that frequency-domain system identification methods work best as narrow-band estimation procedures. Further evidence is provided by the successful identification employing the band processing approach, the results of which are listed in Table 6.17.

Table 6.13:  Estimated Natural Frequencies — 12-DOF Model vs Solution Method

| Exact | Noise Free | | TLS | | STLS | |
|---|---|---|---|---|---|---|
| Freq. (Hz) | Freq. (Hz) | Percent Error | Freq. (Hz) | Percent Error | Freq. (Hz) | Percent Error |
| 1.1564 | 1.1563 | 1.560e–02 | 1.2983 | 1.226e+01 | 1.1701 | 1.182e+00 |
| 6.0642 | 6.0643 | 6.787e–04 | 6.0660 | 2.812e–02 | 605.85 | 9.405e–02 |
| 10.783 | 10.783 | 2.530e–03 | 10.957 | 1.605e+00 | 10.830 | 4.323e–01 |
| 18.127 | 18.127 | 2.632e–03 | 18.761 | 3.500e+00 | 18.221 | 5.221e–01 |
| 109.49 | 109.49 | 2.860e–03 | 109.43 | 5.631e–02 | 109.46 | 2.827e–02 |
| 127.14 | 127.19 | 4.276e–02 | 127.61 | 3.710e–01 | 127.49 | 2.772e–01 |
| 137.82 | 137.82 | 7.165e–04 | 137.70 | 8.719e–02 | 137.73 | 6.834e–02 |
| 156.87 | 156.86 | 7.596e–03 | 156.66 | 1.359e–01 | 156.71 | 1.057e–01 |
| 297.66 | 296.99 | 2.239e–01 | 291.23 | 2.160e+00 | 295.51 | 7.223e–01 |
| 304.47 | 304.41 | 1.833e–02 | 304.49 | 6.377e–03 | 304.96 | 1.610e–01 |
| 606.45 | 605.93 | 8.683e–02 | 600.29 | 1.016e+00 | 603.69 | 4.558e–01 |
| 631.08 | 609.92 | 3.353e+00 | 653.34 | 3.528e+00 | 654.15 | 3.656e+00 |

Table 6.14:  Estimated Damping Factors — 12-DOF Model vs Solution Method

| Exact | Noise Free | | TLS | | STLS | |
|---|---|---|---|---|---|---|
| Damp. Ratio | Damp. Ratio | Percent Error | Damp. Ratio | Percent Error | Damp. Ratio | Percent Error |
| 0.02 | 0.02006 | 2.965e–01 | 0.01737 | 1.312e+01 | 0.02002 | 9.185e–02 |
| 0.02 | 0.01995 | 2.550e–01 | 0.01975 | 1.225e+00 | 0.01989 | 5.410e–01 |
| 0.02 | 0.02025 | 1.257e+00 | 0.02139 | 6.977e+00 | 0.02225 | 1.127e+01 |
| 0.02 | 0.01936 | 3.193e+00 | 0.01758 | 1.211e+01 | 0.01717 | 1.413e+01 |
| 0.02 | 0.02003 | 1.563e–01 | 0.02158 | 7.932e+00 | 0.02105 | 5.268e+00 |
| 0.02 | 0.02012 | 6.068e–01 | 0.01935 | 3.234e+00 | 0.01856 | 7.178e+00 |
| 0.02 | 0.01999 | 4.555e–02 | 0.02171 | 8.545e+00 | 0.02154 | 7.699e+00 |
| 0.02 | 0.02000 | 4.095e–03 | 0.02102 | 5.094e+00 | 0.02089 | 4.474e+00 |
| 0.02 | 0.01982 | 8.829e–01 | 0.02975 | 4.876e+01 | 0.02880 | 4.400e+01 |
| 0.02 | 0.01989 | 5.649e–01 | 0.02251 | 1.254e+01 | 0.02257 | 1.285e+01 |
| 0.02 | 0.01979 | 1.029e+00 | 0.02351 | 1.754e+01 | 0.01557 | 2.215e+01 |
| 0.02 | 0.02774 | 3.869e+01 | 0.06257 | 2.128e+02 | 0.06822 | 2.411e+02 |

## 6.3   Results of Narrow-Band Processing

This section presents the results of simulations where the band processing approach described in Section 5.2 was used in the identification procedure. The band processing approach was motivated by the unsuccessful identification of the 16-DOF model in the previous section. First, the method was applied to the 16-DOF model using noise-free data to determine if the idea would yield valid results. Then the data containing noise was used.

The same simulated FRF data that was used in Section 6.2.3 for the 16-DOF model, with the input frequency spectrum of 1–2100 Hz and 1024 equally spaced frequency lines, is used here. Following the procedure outlined in Section 5.2, the frequency data was divided into 100-Hz frequency bands with 50-Hz overlap, which results in 41 frequency bands. For each frequency band, the SSID identification proceeded through the solution of Eq. 3.12. The estimated natural frequencies computed using Eq. 5.19 are plotted in Figures 6.18–6.19. The vertical lines indicate the target-mode frequencies. Note that even though each frequency band spans only 100 Hz, the frequencies outside of a given band are also correctly identified. This is true only when noise-free data is used, as is evident when Figs. 6.18–6.19 and 6.21–6.22 are compared. However, the out-of-band frequencies will be discarded by virtue of the first selection criterion listed in Section 5.2. The roots in bands 1, 3, 6, 13, 24, and 40 were selected as the identified modal parameters, and the remaining portion of the SSID was then carried out to identify the system matrices.

The three different approaches described in Section 5.2 for solving Eq. 3.23 were used to solve for the scale factors $\bar{a}$. These approaches are referred

to as BP1, BP2, and BP3 respectively. The BP1 estimates did not yield positive definite system matrices and are not included here. The results from the other two methods are shown in Tables 6.15 and 6.16 and in Figure 6.20. The BP2 estimate provides the best estimation of the natural frequencies. However, the BP2 results tend to overestimate the response at high frequencies, while the response of BP3 is much closer to the one obtained using the original SSID formulation. The reason for the overestimation by the BP2 estimate has yet to be resolved. The estimates of the damping factors are the same for both band processing estimations, since the damping factors are computed from the same identified modal parameters. The difference between BP2 and BP3 is in the data used in Eq. 3.23 for the estimation of the $\bar{a}_r$ coefficients. The band processing method estimates the damping factors very well. The results indicate that the modal parameters, Eq. 3.23, can be estimated band by band, collected and stored, and then used for the final estimation of the system matrices.

The band processing approach was also applied to the noisy data for the 16 degree of freedom model used in the previous section. Using the original SSID formulation, no acceptable solution was ever obtained using any of the three least squares solution methods. The simulated data was divided into the same 41 frequency bands used in the last example and each band was processed through Eq. 3.12. The TLS method was used to solve Eq. 3.7. The estimated natural frequencies are plotted in Figures 6.21 and 6.22. Notice that when noise is applied to the signal, the TLS method tries to fit the data to the corresponding frequency band and most of the frequencies are estimated near the center of the band. This results in the identification of many "noise modes."

Table 6.15: Estimated Natural Frequencies — 16-DOF Noise-Free Model Employing Band Processing

| Exact | SSID | | BP2 | | BP3 | |
|---|---|---|---|---|---|---|
| Freq. (Hz) | Freq. (Hz) | Percent Error | Freq. (Hz) | Percent Error | Freq. (Hz) | Percent Error |
| 1.1564 | 1.1507 | 4.948e–01 | 1.1564 | 2.972e–05 | 1.1564 | 1.826e–05 |
| 6.0642 | 6.0628 | 2.430e–02 | 6.0642 | 2.348e–04 | 6.0642 | 8.340e–04 |
| 10.783 | 10.807 | 2.165e–01 | 10.783 | 1.096e–04 | 10.783 | 6.707e–06 |
| 18.127 | 18.115 | 6.439e–02 | 18.127 | 9.541e–05 | 18.126 | 1.658e–03 |
| 109.49 | 109.49 | 1.539e–03 | 109.49 | 3.223e–03 | 109.49 | 8.542e–04 |
| 127.14 | 127.15 | 7.669e–03 | 127.14 | 2.056e–03 | 127.14 | 1.502e–03 |
| 137.82 | 137.82 | 2.866e–03 | 137.81 | 6.636e–03 | 137.81 | 9.261e–03 |
| 156.87 | 156.86 | 5.341e–03 | 156.87 | 1.868e–03 | 156.87 | 4.088e–04 |
| 297.66 | 297.61 | 1.796e–02 | 297.26 | 1.345e–01 | 297.56 | 3.264e–02 |
| 304.47 | 304.41 | 1.745e–02 | 304.01 | 1.495e–01 | 304.50 | 1.125e–02 |
| 606.45 | 606.24 | 3.595e–02 | 605.12 | 2.202e–01 | 606.46 | 1.323e–03 |
| 631.08 | 626.89 | 6.648e–01 | 630.17 | 1.450e–01 | 629.75 | 2.110e–01 |
| 1190.4 | 1189.4 | 8.538e–01 | 1188.9 | 1.306e–01 | 1195.1 | 3.959e–01 |
| 1193.3 | 1192.3 | 8.922e–02 | 1191.1 | 1.872e–01 | 1196.4 | 2.525e–01 |
| 2029.1 | 2017.0 | 5.990e–01 | 2029.0 | 8.002e–03 | 2144.5 | 5.683e+00 |
| 2031.2 | 2017.6 | 6.686e–01 | 2031.8 | 2.758e–02 | 2171.2 | 6.893e+00 |

Table 6.16: Estimated Damping Factors — 16-DOF Noise-Free Model Employing Band Processing

| Exact | SSID | | BP | |
|---|---|---|---|---|
| Damp. Ratio | Damp. Ratio | Percent Error | Damp. Ratio | Percent Error |
| 0.02 | 0.01980 | 1.022e+00 | 0.02000 | 2.688e−08 |
| 0.02 | 0.02104 | 5.179e+00 | 0.02000 | 1.833e−06 |
| 0.02 | 0.01824 | 8.789e+00 | 0.02000 | 4.289e−09 |
| 0.02 | 0.02055 | 2.754e+00 | 0.02000 | 1.311e−09 |
| 0.02 | 0.02009 | 4.696e−01 | 0.02000 | 4.131e−06 |
| 0.02 | 0.01882 | 5.911e+00 | 0.02000 | 2.508e−08 |
| 0.02 | 0.01993 | 3.678e−01 | 0.02000 | 7.951e−08 |
| 0.02 | 0.01993 | 3.481e−01 | 0.02000 | 1.177e−07 |
| 0.02 | 0.02157 | 7.847e+00 | 0.02000 | 3.463e−06 |
| 0.02 | 0.01980 | 9.997e−01 | 0.02000 | 4.913e−08 |
| 0.02 | 0.02018 | 8.870e−01 | 0.02000 | 1.115e−05 |
| 0.02 | 0.02593 | 2.964e+01 | 0.02000 | 2.233e−02 |
| 0.02 | 0.02031 | 1.552e+00 | 0.02000 | 1.140e−03 |
| 0.02 | 0.01923 | 3.830e+00 | 0.02000 | 3.208e−05 |
| 0.02 | 0.01549 | 2.257e+01 | 0.02000 | 1.718e−03 |
| 0.02 | 0.01571 | 2.145e+01 | 0.02000 | 2.260e−03 |

An index of 0.95 was selected as the MPC criterion. Modes with MPC indices less than this value were rejected as noise modes. After application of the four selection criteria listed in Section 5.2, the selected roots are again plotted, as shown in Figures 6.23 and 6.24.

The results of the identification are shown in Table 6.17 and in Figure 6.25. The results are very encouraging, especially since no acceptable result was previously obtained using this same noisy data. As before, the BP2 solution provides a better estimate of the natural frequencies. The high-frequency response of the BP2 estimation is an overestimation of the true response, while the low-frequency response of the BP3 estimate is an underestimation of the exact response.

Table 6.17: Estimated Modal Parameters — 16-DOF Model Employing Band Processing with Noisy Data

| Exact Freq. (Hz) | BP2 Freq. (Hz) | BP2 Percent Error | BP3 Freq. (Hz) | BP3 Percent Error | Exact Damp. Ratio | BP Damp. Ratio | Percent Error |
|---|---|---|---|---|---|---|---|
| 1.1564 | 1.1435 | 1.116e+00 | 1.4273 | 2.342e+01 | 0.02 | 0.00764 | 6.178e+01 |
| 6.0642 | 6.0579 | 1.054e-01 | 6.1922 | 2.110e+00 | 0.02 | 0.02016 | 7.789e-01 |
| 10.783 | 10.784 | 6.916e-03 | 12.538 | 1.629e+01 | 0.02 | 0.02046 | 2.296e+00 |
| 18.127 | 18.132 | 2.896e-02 | 19.005 | 4.846e+00 | 0.02 | 0.02143 | 7.152e+00 |
| 109.49 | 109.51 | 1.700e-02 | 109.51 | 1.989e-02 | 0.02 | 0.01880 | 5.985e+00 |
| 127.14 | 127.24 | 7.661e-02 | 127.39 | 2.013e-01 | 0.02 | 0.01977 | 1.168e+00 |
| 137.82 | 137.82 | 4.082e-04 | 137.80 | 1.642e-02 | 0.02 | 0.02009 | 4.474e-01 |
| 156.87 | 156.85 | 1.089e-02 | 156.87 | 9.918e-04 | 0.02 | 0.01996 | 1.836e-01 |
| 297.66 | 297.68 | 5.516e-03 | 297.92 | 8.773e-02 | 0.02 | 0.01987 | 6.248e-01 |
| 304.47 | 304.39 | 2.448e-02 | 304.04 | 1.415e-01 | 0.02 | 0.01975 | 1.239e+00 |
| 606.45 | 606.72 | 4.421e-02 | 606.75 | 4.916e-02 | 0.02 | 0.02058 | 2.911e+00 |
| 631.08 | 630.93 | 2.382e-02 | 631.76 | 1.073e-01 | 0.02 | 0.01957 | 2.145e+00 |
| 1190.4 | 1191.1 | 5.449e-02 | 1186.1 | 3.625e-01 | 0.02 | 0.02004 | 1.824e-01 |
| 1193.3 | 1193.1 | 2.350e-02 | 1192.0 | 1.118e-01 | 0.02 | 0.02000 | 1.637e-02 |
| 2029.1 | 2015.9 | 6.522e-01 | 2015.5 | 6.693e-01 | 0.02 | 0.01864 | 6.796e+00 |
| 2031.2 | 2031.8 | 2.709e-02 | 2054.4 | 1.141e+00 | 0.02 | 0.01896 | 5.213e+00 |

The band processing technique was also applied to the remaining two reduced-order models using noisy data. Figures 6.26 and 6.27 show the comparisons of a drive-point FRF for each of the reduced-order models. The data used for the 12-DOF model was divided into 12 overlapping 100-Hz frequency bands. The results are similar to those obtained using the 16-DOF model. In order for the BP2 estimation to yield acceptable results, the 1 Hz data point was omitted. This would be similar to ignoring data with very low coherence values. The low frequency data is still severely corrupted by noise, even after sufficient averaging, and including this point in the BP2 estimation introduced large errors into the estimated frequency response.

For the 10-DOF model, the BP2 estimation of the response is in serious error, as indicated in Figure 6.27. For this model, the simulated data was split into 50-Hz frequency bands with 25-Hz overlap, resulting in 11 frequency bands. The reason for the error in the BP2 estimation is unknown. However, it is possible that the model is too small for use with the band processing technique or the frequency bands may too narrow. More research is needed to determine the width and the number of frequency bands to use for a given model order. The use or development of additional modal quality indicators should also be addressed to help identify and confirm the estimated structural modes. Also, coherence blanking or other measures might be useful in selecting FRF data, or FRFs might be obtained by employing stepped sine-dwell processing.

## 6.4 Pseudo Degrees of Freedom

This section presents the results of augmenting the model order using pseudo degrees of freedom (PDF). For this simulation, the 10-DOF model was used and the the input frequency range was 1–2100 Hz with 1024 equally space frequency lines. Using the pseudo degrees of freedom, the model order was expanded to create a 20-DOF pseudo-degree-of-freedom model, and the identification process through Eq. 3.12 was completed. As mentioned in Section 5.3, the remaining portion of the identification has yet to be defined for pseudo degrees of freedom. No noise was added to the data. Table 6.18 gives a listing of the estimated frequencies from the solution of Eq. 3.12 and compares those to the frequencies obtained using only the original ten degrees of freedom.

Table 6.18: Identified Natural Frequencies Using Pseudo Degrees of Freedom

| Pseudo DOF Model | | | | Original Model | |
|---|---|---|---|---|---|
| Mode Number | Freq. (Hz) | Mode Number | Freq. (Hz) | Mode Number | Freq. (Hz) |
| 1 | 1.1026 | 11 | 304.24 | 1 | 1.1454 |
| 2 | 6.0572 | 12 | 463.91 | 2 | 6.0878 |
| 3 | 10.387 | 13 | 497.10 | 3 | 10.989 |
| 4 | 18.063 | 14 | 1189.8 | 4 | 18.293 |
| 5 | 109.50 | 15 | 1193.2 | 5 | 109.52 |
| 6 | 128.19 | 16 | 1675.1 | 6 | 127.75 |
| 7 | 137.82 | 17 | 1686.4 | 7 | 137.81 |
| 8 | 156.89 | 18 | 1713.0 | 8 | 156.99 |
| 9 | 271.10 | 19 | 2029.5 | 9 | 308.15 |
| 10 | 297.17 | 20 | 2031.6 | 10 | 311.36 |

Using the original 10 degrees of freedom, only the lowest 10 modes could be identified even though more are present in the data. When the order

of the model is expanded by use of pseudo degrees of freedom, the model is able to identify 4 additional target modes, modes 21, 22, 29, and 30, plus some additional computational modes. Some sort of modal quality indicator is needed to distinguish between the physical and computational modes of the PDF model. This approach doubles the model order. In some instances, this may be too large and the model order may need to be decreased from twice the original size. A reduction step would then be required to determine the appropriate model order. The initial results are encouraging, since some of the higher frequencies can be identified using the pseudo degrees of freedom.

The mode shapes from the PDF model are listed in Tables 6.19 and 6.20. The mode shapes listed here are the normal modes of the PDF model. They are obtained by solving the algebraic eigenvalue problem using $\hat{K} = M^{-1}K$, which is obtained from the solution of Equation. 3.7. Note that for the lower frequency modes, the mode shape appears in the lower-frequency partition of the mode shape and the higher frequency mode shapes appear in the high-frequency partition, or in the pseudo degrees of freedom. The pseudo degrees of freedom could possibly be treated as generalized coordinates and then the SSID algorithm could proceed with the identification of the system matrices.

Table 6.19: Mode Shapes of the 10-DOF Model Employing Pseudo Degree of Freedom – Modes 1 through 10

| Mode 1 | Mode 2 | Mode 3 | Mode 4 | Mode 5 | Mode 6 | Mode 7 | Mode 8 | Mode 9 | Mode 10 |
|---|---|---|---|---|---|---|---|---|---|
| 1.000 | -0.997 | -0.967 | 1.000 | -0.274 | -0.996 | -0.058 | -0.294 | 0.483 | -1.000 |
| 0.998 | -0.339 | -1.000 | 0.339 | 0.215 | 0.558 | -0.037 | 0.127 | -0.319 | 0.694 |
| 0.996 | 0.292 | -1.000 | -0.305 | 0.215 | 0.557 | 0.041 | 0.127 | 0.216 | -0.716 |
| 0.994 | 0.951 | -0.968 | -0.967 | -0.274 | -1.000 | 0.057 | -0.294 | -0.908 | 0.919 |
| 1.000 | -0.997 | 0.967 | -1.000 | -0.274 | 0.996 | -0.058 | -0.294 | 0.483 | 1.000 |
| 0.998 | -0.339 | 1.000 | -0.339 | 0.215 | -0.558 | -0.037 | 0.127 | -0.319 | -0.694 |
| 0.996 | 0.292 | 1.000 | 0.305 | 0.215 | -0.557 | 0.041 | 0.127 | 0.216 | 0.716 |
| 0.994 | 0.951 | 0.968 | 0.967 | -0.274 | 1.000 | 0.057 | -0.294 | -0.908 | -0.919 |
| 0.994 | 0.954 | 0.000 | 0.000 | -1.000 | 0.000 | -0.981 | 1.000 | 0.751 | 0.000 |
| 1.000 | -1.000 | 0.000 | 0.000 | -0.999 | 0.000 | 1.000 | 0.999 | -0.465 | 0.000 |
| 0.000 | 0.000 | 0.000 | 0.000 | 0.000 | 0.000 | 0.000 | 0.000 | 0.036 | 0.000 |
| 0.000 | 0.000 | 0.000 | 0.000 | 0.000 | 0.000 | 0.000 | 0.000 | -0.001 | 0.000 |
| 0.000 | 0.000 | 0.000 | 0.000 | 0.000 | 0.000 | 0.000 | 0.000 | 0.002 | 0.000 |
| 0.000 | 0.000 | 0.000 | 0.000 | 0.000 | 0.000 | 0.000 | 0.000 | 0.010 | 0.000 |
| 0.000 | 0.000 | 0.000 | 0.000 | 0.000 | 0.000 | 0.000 | 0.000 | 0.036 | 0.000 |
| 0.000 | 0.000 | 0.000 | 0.000 | 0.000 | 0.000 | 0.000 | 0.000 | -0.001 | 0.000 |
| 0.000 | 0.000 | 0.000 | 0.000 | 0.000 | 0.000 | 0.000 | 0.000 | 0.002 | 0.000 |
| 0.000 | 0.000 | 0.000 | 0.000 | 0.000 | 0.000 | 0.000 | 0.000 | 0.010 | 0.000 |
| 0.000 | 0.000 | 0.000 | 0.000 | 0.000 | 0.000 | 0.000 | 0.000 | -0.001 | 0.000 |
| 0.000 | 0.000 | 0.000 | 0.000 | 0.000 | 0.000 | 0.000 | 0.000 | -1.000 | 0.000 |

Table 6.20: Mode Shapes of the 10-DOF Model Employing Pseudo Degree of Freedom – Modes 11 through 20

| Mode 11 | Mode 12 | Mode 13 | Mode 14 | Mode 15 | Mode 16 | Mode 17 | Mode 18 | Mode 19 | Mode 20 |
|---|---|---|---|---|---|---|---|---|---|
| -1.000 | 0.240 | -0.866 | -0.079 | -0.054 | 1.000 | -0.095 | 0.095 | -0.042 | 0.018 |
| 0.650 | -1.000 | -1.000 | -0.042 | -0.030 | 0.695 | -0.032 | 0.032 | -0.007 | 0.047 |
| -0.672 | 0.760 | 0.367 | -0.023 | -0.020 | -0.147 | -0.046 | 0.046 | -0.037 | -0.047 |
| 0.938 | -0.814 | -0.830 | -0.070 | -0.086 | 0.839 | -0.087 | 0.087 | -0.055 | -0.013 |
| -1.000 | -0.240 | -0.866 | -0.079 | 0.054 | -1.000 | -0.095 | 0.095 | -0.042 | -0.018 |
| 0.650 | 1.000 | -1.000 | -0.042 | 0.030 | -0.695 | -0.032 | 0.032 | -0.007 | -0.047 |
| -0.672 | -0.760 | 0.367 | -0.023 | 0.020 | 0.147 | -0.046 | 0.046 | -0.037 | 0.047 |
| 0.938 | 0.814 | -0.830 | -0.070 | 0.086 | -0.839 | -0.087 | 0.087 | -0.055 | 0.013 |
| -0.511 | 0.000 | 0.282 | 0.018 | 0.000 | 0.000 | 0.074 | -0.074 | 0.019 | 0.000 |
| 0.542 | 0.000 | 0.317 | 0.020 | 0.000 | 0.000 | -0.006 | 0.006 | 0.006 | 0.000 |
| 0.000 | 0.062 | 0.015 | -0.371 | -0.384 | 0.028 | -0.158 | 0.158 | 0.420 | 0.439 |
| 0.000 | 0.080 | 0.034 | -1.000 | -1.000 | -0.054 | -0.080 | 0.080 | 0.995 | 0.995 |
| 0.000 | -0.077 | -0.032 | 0.999 | 1.000 | 0.050 | 0.063 | -0.063 | 1.000 | 1.000 |
| -0.001 | 0.901 | 0.446 | 0.375 | 0.384 | -0.115 | 0.186 | -0.186 | 0.436 | 0.428 |
| 0.000 | -0.062 | 0.015 | -0.371 | 0.384 | -0.028 | -0.158 | 0.158 | 0.420 | -0.439 |
| 0.000 | -0.080 | 0.034 | -1.000 | 1.000 | 0.054 | -0.080 | 0.080 | 0.995 | -0.995 |
| 0.000 | 0.077 | -0.032 | 0.999 | -1.000 | -0.050 | 0.063 | -0.063 | 1.000 | -1.000 |
| -0.001 | -0.901 | 0.446 | 0.375 | -0.384 | 0.115 | 0.186 | -0.186 | 0.436 | -0.428 |
| 0.000 | 0.000 | -0.115 | -0.096 | 0.000 | 0.000 | 1.000 | -1.000 | -0.061 | 0.000 |
| 0.011 | 0.000 | 0.289 | 0.100 | 0.000 | 0.000 | -0.846 | 0.846 | -0.158 | 0.000 |

## 6.5 Comparison of SSID-Identified Models with Existing TAMs

In this section, the SSID-identified reduced-order models are compared to three of the TAM models discussed in Chapter 4: the Guyan model, the Improved Reduction System (IRS) model, and the Craig-Bampton (C-B) model in physical coordinates. The appropriate fixed-interface normal modes for use in the C-B models were selected using the technique described in Section 4.4.2. For each TAM, the estimated natural frequencies and the prediction of the dynamic response are compared for each of the reduced-order model sizes, 10, 12, and 16 degrees of freedom. Orthogonality and cross-orthogonality checks were performed using each TAM, and very good results were found for each TAM, with diagonal values near unity and off-diagonal terms less than 0.1.

Tables 6.21 through 6.23 list the estimated undamped natural frequencies for each of the reduced-order model sizes. Except for the very lowest frequencies, the SSID reduced-order models generally provide a better estimation of the natural frequencies than does the Guyan reduction method. The IRS and C-B models also estimate the lower natural frequencies better than the do SSID models. However, for the middle and higher frequencies of each model size, the SSID-identified model performs as well, if not slightly better, than these other two TAMs.

A comparison of the estimated FRFs for each of the model sizes is given in Figures 6.28–6.30. The physical damping matrix used for each of the TAMs was computed by using the real normal modes estimated by each model and the damping factors estimated by the SSID algorithm for the corresponding

model size and computing a modal damping matrix. As shown in the figures, all four methods represent the dynamic response of the original 52-DOF model very well.

Table 6.21: Estimated Natural Frequencies — 10-DOF TAMs

| SSID | | Guyan | | IRS | | C-B | |
|---|---|---|---|---|---|---|---|
| Freq. (Hz) | Percent Error | Freq. (Hz) | Percent Error | Freq. (Hz) | Percent Error | Freq. (Hz) | Percent Error |
| 1.1552 | 1.116e–01 | 1.1564 | 1.100e–04 | 1.1564 | 3.834e–08 | 1.1564 | 2.352e–06 |
| 6.0647 | 6.755e–03 | 6.0644 | 2.576e–03 | 6.0642 | 1.064e–09 | 6.0643 | 1.660e–04 |
| 10.784 | 7.202e–03 | 10.785 | 1.004e–02 | 10.783 | 1.411e–09 | 10.783 | 3.144e–04 |
| 18.126 | 5.608e–03 | 18.132 | 2.629e–02 | 18.127 | 2.559e–09 | 18.127 | 2.187e–03 |
| 109.49 | 3.624e–03 | 109.56 | 6.129e–02 | 109.49 | 1.043e–05 | 109.52 | 2.261e–02 |
| 127.12 | 1.203e–02 | 127.46 | 2.558e–01 | 127.14 | 3.221e–04 | 127.32 | 1.400e–01 |
| 137.83 | 4.228e–03 | 138.08 | 1.866e–01 | 137.82 | 3.570e–05 | 137.83 | 5.044e–03 |
| 156.87 | 1.263e–03 | 157.25 | 2.436e–01 | 156.87 | 9.836e–04 | 157.06 | 1.194e–01 |
| 297.52 | 4.736e–02 | 309.83 | 4.087e+00 | 297.82 | 5.248e–02 | 300.04 | 7.981e–01 |
| 303.74 | 2.376e–01 | 314.79 | 3.392e+00 | 304.51 | 1.368e–02 | 306.30 | 6.034e–01 |

Table 6.22: Estimated Natural Frequencies — 12-DOF TAMs

| SSID | | Guyan | | IRS | | C-B | |
|---|---|---|---|---|---|---|---|
| Freq. (Hz) | Percent Error | Freq. (Hz) | Percent Error | Freq. (Hz) | Percent Error | Freq. (Hz) | Percent Error |
| 1.1563 | 1.560e–02 | 1.1564 | 4.802e–06 | 1.1564 | 3.876e–08 | 1.1564 | 4.419e–07 |
| 6.0643 | 6.787e–04 | 6.0643 | 8.648e–05 | 6.0642 | 1.052e–09 | 6.0642 | 2.380e–05 |
| 10.783 | 2.530e–03 | 10.783 | 6.218e–04 | 10.783 | 7.343e–10 | 10.783 | 2.519e–04 |
| 18.127 | 2.632e–03 | 18.127 | 2.137e–03 | 18.127 | 1.610e–09 | 18.127 | 1.752e–03 |
| 109.49 | 2.860e–03 | 109.55 | 5.700e–02 | 109.49 | 5.814e–06 | 109.50 | 5.780e–03 |
| 127.19 | 4.276e–02 | 127.40 | 2.055e–01 | 127.14 | 1.957e–04 | 127.28 | 1.120e–01 |
| 137.82 | 7.165e–04 | 137.84 | 1.035e–02 | 137.82 | 9.817e–07 | 137.83 | 4.813e–03 |
| 156.86 | 7.596e–03 | 157.01 | 8.613e–02 | 156.87 | 3.124e–05 | 156.90 | 1.518e–02 |
| 296.99 | 2.239e–01 | 301.40 | 1.257e+00 | 297.76 | 3.218e–02 | 299.54 | 6.327e–01 |
| 304.41 | 1.833e–02 | 306.93 | 8.094e–01 | 304.48 | 3.440e–03 | 304.69 | 7.437e–02 |
| 605.93 | 8.683e–02 | 608.57 | 3.492e–01 | 595.82 | 1.753e+00 | 607.42 | 1.589e–01 |
| 609.92 | 3.353e+00 | 611.20 | 3.151e+00 | 606.46 | 3.901e+00 | 617.48 | 2.155e+00 |

Percent differences were computed between the SSID mass and stiff-

Table 6.23: Estimated Natural Frequencies — 16-DOF TAMs

| SSID | | Guyan | | IRS | | C-B | |
|---|---|---|---|---|---|---|---|
| Freq. (Hz) | Percent Error | Freq. (Hz) | Percent Error | Freq. (Hz) | Percent Error | Freq. (Hz) | Percent Error |
| 1.1507 | 4.948e–01 | 1.1564 | 1.864e–06 | 1.1564 | 3.904e–08 | 1.1564 | 1.242e–07 |
| 6.0628 | 2.430e–02 | 6.0643 | 7.634e–05 | 6.0642 | 1.108e–09 | 6.0642 | 5.057e–06 |
| 10.807 | 2.165e–01 | 10.783 | 3.467e–01 | 10.783 | 7.736e–10 | 10.783 | 2.255e–04 |
| 18.115 | 6.439e–02 | 18.127 | 2.036e–03 | 18.127 | 1.557e–09 | 18.127 | 1.569e–03 |
| 109.49 | 1.539e–03 | 109.50 | 8.567e–03 | 109.49 | 5.435e–06 | 109.49 | 1.934e–03 |
| 127.15 | 7.669e–03 | 127.27 | 1.026e–01 | 127.14 | 1.943e–04 | 127.27 | 1.006e–01 |
| 137.82 | 2.866e–03 | 137.83 | 7.427e–03 | 137.82 | 6.314e–07 | 137.83 | 3.774e–03 |
| 156.86 | 5.341e–03 | 156.91 | 2.329e–02 | 156.87 | 2.836e–05 | 156.88 | 5.222e–03 |
| 297.61 | 1.796e–02 | 299.12 | 4.909e–01 | 297.75 | 3.140e–02 | 299.38 | 5.779e–01 |
| 304.41 | 1.745e–02 | 304.53 | 2.095e–02 | 304.47 | 6.180e–06 | 304.51 | 1.448e–02 |
| 606.24 | 3.595e–02 | 604.31 | 3.535e–01 | 595.50 | 1.807e+00 | 606.61 | 2.544e–02 |
| 626.89 | 6.648e–01 | 607.01 | 3.814e+00 | 606.43 | 3.906e+00 | 617.20 | 2.200e+00 |
| 1189.4 | 8.538e–02 | 1212.4 | 1.848e+00 | 1133.1 | 4.816e+00 | 1189.5 | 7.938e–02 |
| 1192.3 | 8.922e–02 | 1214.1 | 1.738e+00 | 1190.8 | 2.093e–01 | 1191.1 | 1.911e–01 |
| 2017.0 | 5.990e–01 | 2227.5 | 9.774e+00 | 1752.9 | 1.361e+01 | 2029.3 | 7.551e–03 |
| 2017.6 | 6.686e–01 | 2228.7 | 9.721e+00 | 2052.1 | 1.026e+00 | 2035.0 | 1.865e–01 |

ness matrices and those of the other TAMs. Figures 6.31 and 6.32 are representative results from the different comparisons. The only difference is that for the 10-DOF models, the percent differences are slightly smaller and for the 16-DOF models, the differences are slightly larger. The main point is that the mass and stiffness matrices of the various TAM models are noticeably different. They do, however, yield essentially the same natural frequencies and result in the same estimated frequency response functions. Berman points out that multiple solutions of the same model can exist and have significantly different terms in the system matrices [67]. He shows that the stiffness matrix can be written in terms of the modes of the system and that if not all of the modes of the system are included, the estimated stiffness matrix will not be the same as the original stiffness matrix, but will still be representative of the system's

stiffness over a specified frequency range. This leads to the conclusion that, in test situations, it is impossible to identify a unique mass and stiffness matrices. However, the identified matrices still represent the dynamic characteristics of the original structure.

Since the SSID algorithm identifies reduced-order mass and stiffness matrices of the physical system, all the information associated with a Craig-Bampton model is available, including information about the constraint modes. The SSID reduced-order models were put into the Craig-Bampton format and then compared to the corresponding Craig-Bampton analytical models generated from the 52-DOF FEM. Tables 6.24 through 6.26 compare the eigenvalues of the fixed-interface normal modes of the Craig-Bampton models to those obtained from the SSID-identified models in Craig-Bampton format. The data associated with the constraint modes is compared by examining the appropriate partition of the stiffness matrices and is shown in Figures 6.33 through 6.35. As indicated by the results, the SSID-identified models represent the fixed-interface and constraint-mode information very well.

Table 6.24: Comparison of the Eigenvalues of the Fixed-Interface Normal Modes for the 10-DOF Model

| C-B $\Lambda_r$ (rad/sec$^2$) | SSID $\Lambda_r$ (rad/sec$^2$) | Percent Difference |
|---|---|---|
| 6.9895e+03 | 6.9753e+03 | 2.039e−01 |
| 2.4449e+04 | 2.4535e+04 | 3.511e−01 |
| 3.3205e+05 | 3.3086e+05 | 3.602e−01 |
| 3.5364e+05 | 3.5389e+05 | 7.031e−02 |
| 6.9749e+05 | 6.9720e+05 | 4.111e−02 |
| 2.6411e+06 | 2.6397e+06 | 5.427e−02 |
| 2.6885e+06 | 2.6608e+06 | 1.033e+00 |

Table 6.25: Comparison of the Eigenvalues of the Fixed-Interface Normal Modes for the 12-DOF Model

| C-B $\Lambda_r$ (rad/sec$^2$) | SSID $\Lambda_r$ (rad/sec$^2$) | Percent Difference |
|---|---|---|
| 6.9895e+03 | 6.9213e+03 | 9.754e−01 |
| 2.4449e+04 | 2.4325e+04 | 5.092e−01 |
| 3.3205e+05 | 3.2567e+05 | 1.923e+00 |
| 3.5364e+05 | 3.5314e+05 | 1.393e−01 |
| 6.9749e+05 | 6.9726e+05 | 3.244e−02 |
| 2.6411e+06 | 2.5138e+06 | 4.812e+00 |
| 2.6885e+06 | 2.6744e+06 | 5.237e−01 |
| 1.2978e+07 | 9.6505e+06 | 2.564e+01 |
| 1.4456e+07 | 1.3020e+07 | 9.937e+00 |

Table 6.26: Comparison of the Eigenvalues of the Fixed-Interface Normal Modes for the 16-DOF Model

| C-B $\Lambda_r$ (rad/sec$^2$) | SSID $\Lambda_r$ (rad/sec$^2$) | Percent Difference |
|---|---|---|
| 6.9895e+03 | 7.0152e+03 | 3.682e−01 |
| 2.4449e+04 | 2.5629e+04 | 4.825e+00 |
| 3.3205e+05 | 3.3724e+05 | 1.560e+00 |
| 3.5364e+05 | 3.5690e+05 | 9.217e−01 |
| 6.9749e+05 | 6.9884e+05 | 1.944e−01 |
| 2.6411e+06 | 2.6201e+06 | 7.957e−01 |
| 2.6885e+06 | 2.6923e+06 | 1.412e−01 |
| 1.2978e+07 | 1.2986e+07 | 6.287e−02 |
| 1.4456e+07 | 1.3386e+07 | 7.404e+00 |
| 5.3240e+07 | 5.3379e+07 | 2.603e−01 |
| 5.3430e+07 | 5.4037e+07 | 1.138e+01 |
| 1.5448e+08 | 1.4891e+08 | 3.608e+00 |
| 1.5476e+08 | 1.4980e+08 | 3.204e+00 |

## 6.6    SSID Implementation with Reaction Forces Included

This section presents simulations when interface reaction forces were included in data used in the identification of a full-order model of the substructure. In this simulation, reaction forces where measured at all three interface degrees of freedom. At each interface degree of freedom, a 9-DOF test stand was attached to the substructure, resulting in a 79 degree of freedom substructure-test stand assembly. The resulting coupled model is statically determinate. Two independent excitation forces, located at nodes 11 and 16, where used in the identification of the substructure.

The original 52-DOF model was first reduced to the 16 Z-translational

degrees of freedom via Guyan reduction, and the resulting model was considered to be the "true" substructure. The same was done for the coupled 79-DOF substructure-test stand assembly, resulting in a 25-DOF model. Table 6.27 lists the natural frequencies of the substructure-test stand assembly and of the substructure alone. The dynamic response of the coupled system is significantly different from that of the substructure alone. Note that lowest natural frequency of the coupled system is significantly higher than that of the substructure alone. Figure 6.36 compares the response at the same degree of freedom for the substructure-test stand assembly (B structure) to that of the substructure alone (A structure). Rayleigh damping was used instead of modal damping to insure that there was no unwanted damping coupling between the substructure and the test stand.

A frequency spectrum of 1–1000 Hz with 512 equally spaced frequency lines was used for the identification. The results of the simulation are shown in Figures 6.37 through 6.41. The results show that, with noise-free data, the SSID algorithm was able to successfully identify the substructure from the coupled-system data. The system matrices were all identified to less than 0.03%, and the predicted response matches the original response very well. The estimated undamped natural frequencies and damping factors were all identified to within 0.01%. Note that the highest four frequencies were successfully identified even though they are well above the range of the FRF data used in the identification.

Simulations of the full-order model with the reaction forces included were also attempted using noisy data. However, to date none has been successful. One possible reason is the way the noise was applied and the way the

Table 6.27: Undamped Natural Frequencies of the Coupled System and of the Substructure Alone

| B Substructure | | A Substructure | |
|---|---|---|---|
| Number | Frequency (Hz) | Number | Frequency (Hz) |
| 1 | 13.304 | 1 | 1.1564 |
| 2 | 24.775 | 2 | 6.0643 |
| 3 | 90.682 | 3 | 10.783 |
| 4 | 93.526 | 4 | 18.127 |
| 5 | 132.47 | 5 | 109.50 |
| 6 | 253.12 | 6 | 127.27 |
| 7 | 254.95 | 7 | 137.83 |
| 8 | 539.25 | 8 | 156.91 |
| 9 | 541.59 | 9 | 299.12 |
| 10 | 769.29 | 10 | 304.53 |
| 11 | 782.15 | 11 | 604.31 |
| 12 | 1223.4 | 12 | 607.01 |
| 13 | 1224.6 | 13 | 1212.4 |
| 14 | 1277.3 | 14 | 1214.1 |
| 15 | 1415.2 | 15 | 2227.5 |
| 16 | 1416.0 | 16 | 2228.7 |
| 17 | 1561.1 | | |
| 18 | 2230.1 | | |
| 19 | 2231.6 | | |
| 20 | 4080.2 | | |
| 21 | 4080.3 | | |
| 22 | 4081.4 | | |
| 23 | 6118.4 | | |
| 24 | 6118.4 | | |
| 25 | 6118.8 | | |

reaction force was computed. Recall that the noise is applied such that it is proportional to the magnitude of the accelerance FRF. For the coupled system, the acceleration response at low frequencies is very small, while at high frequencies it is several orders of magnitude larger. The opposite is true for the displacement response, and the reaction force was computed as the difference between the displacement of the substructure-test stand interface DOFs multiplied by the coupling reaction-spring constant. Even after averaging, the low frequency acceleration response and the high frequency displacement response, and thus the measured reaction force, are still quite corrupted by the noise and these responses are believed to be very important in these simulations where the reaction forces are included. This indicates that very accurate measurement of the reaction forces will be required for use in the SSID algorithm. An example of a "measured" accelerance FRF of the coupled system is shown in Figure 6.42.

The measured reaction force FRFs due to the force at node 11 that were used in the identification of the full-order, noise-free simulation are presented in Figure 6.43. Note the low response at high frequencies for the interface forces at nodes 4 and 18. To alleviate the problems relating to the reaction forces, several different ideas, such as varying the stiffness of the interface springs, were attempted. Simulations using mass-loaded interfaces were also attempted to increase the magnitude of the measured reaction force at higher frequencies, but none has proved successful.

Additional simulations have been attempted to identify a reduced-order model with the reaction forces included. At this time, no successful

identification of the "payload" used in the present study has been made, and this is still an active area of research. Successful reduced-order-model results have been obtained with the reaction forces included for lumped-parameter models; these can be found in Reference [63].
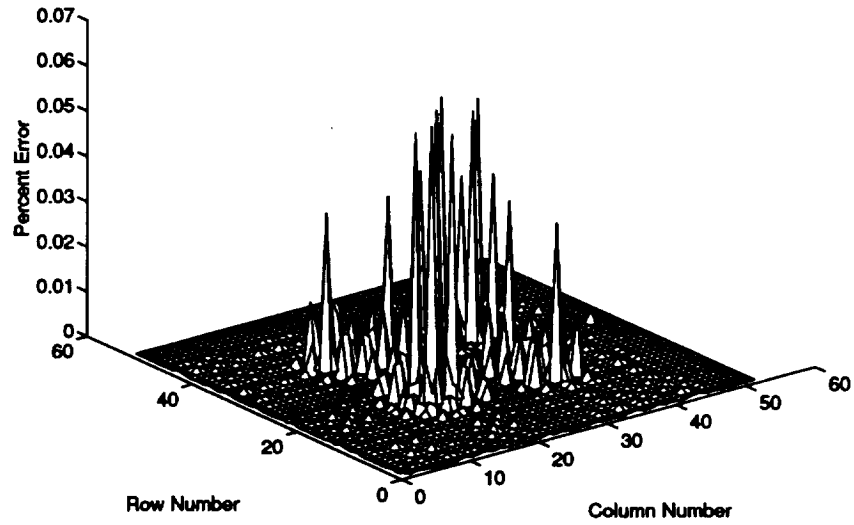
Figure 6.2: Percent Error in the SSID-Estimated Mass Matrix
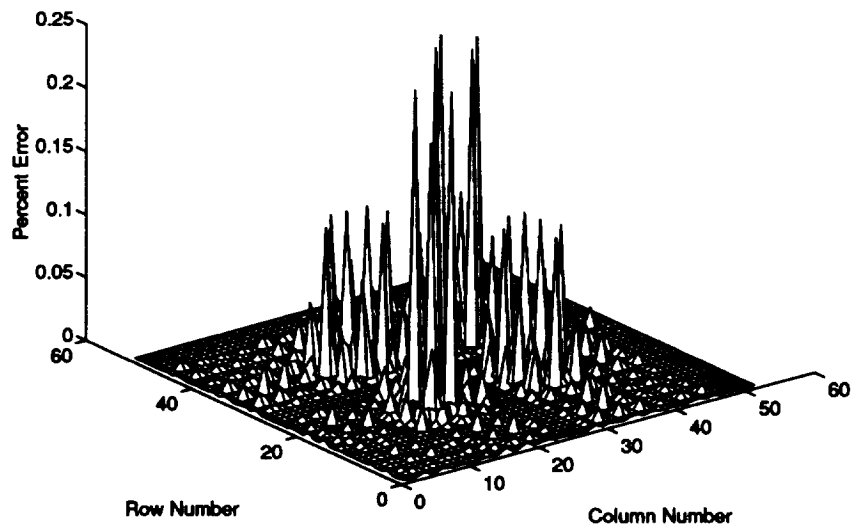


Figure 6.3: Percent Error in the SSID-Estimated Damping Matrix
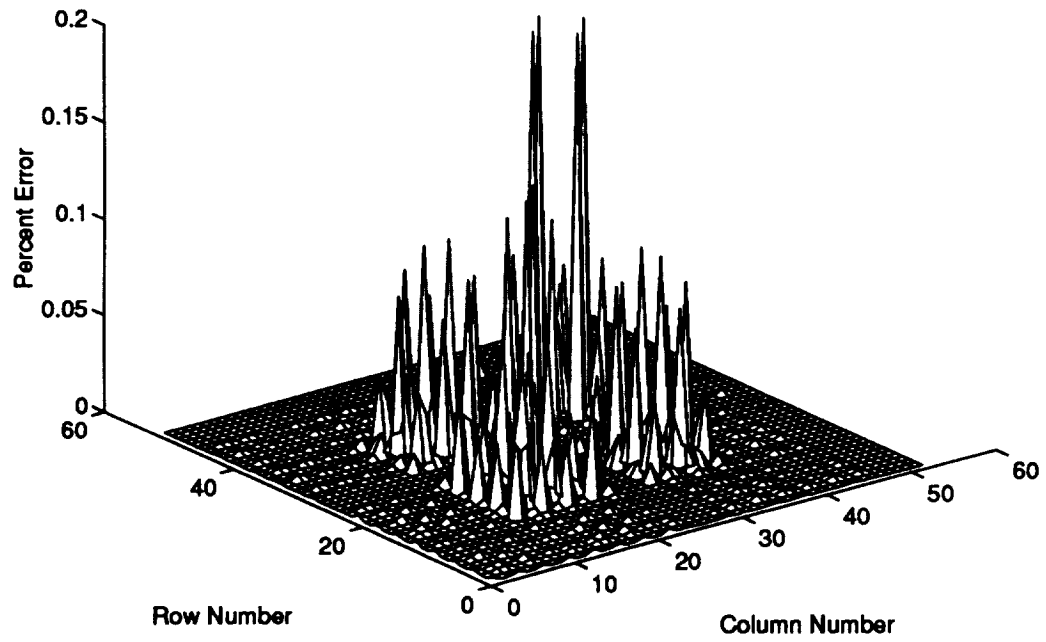
Figure 6.4: Percent Error in the SSID-Estimated Stiffness Matrix
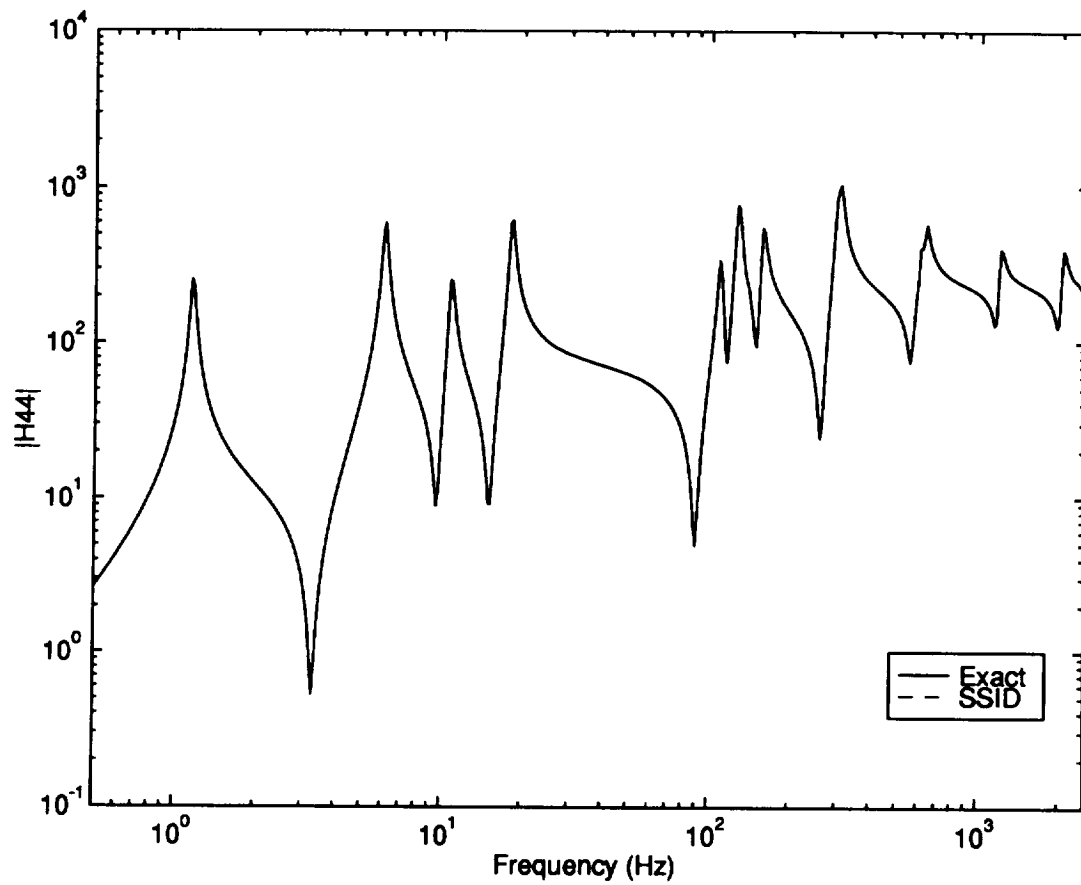
Figure 6.5: Comparison of Drive-Point FRFs for the Full-Order Model
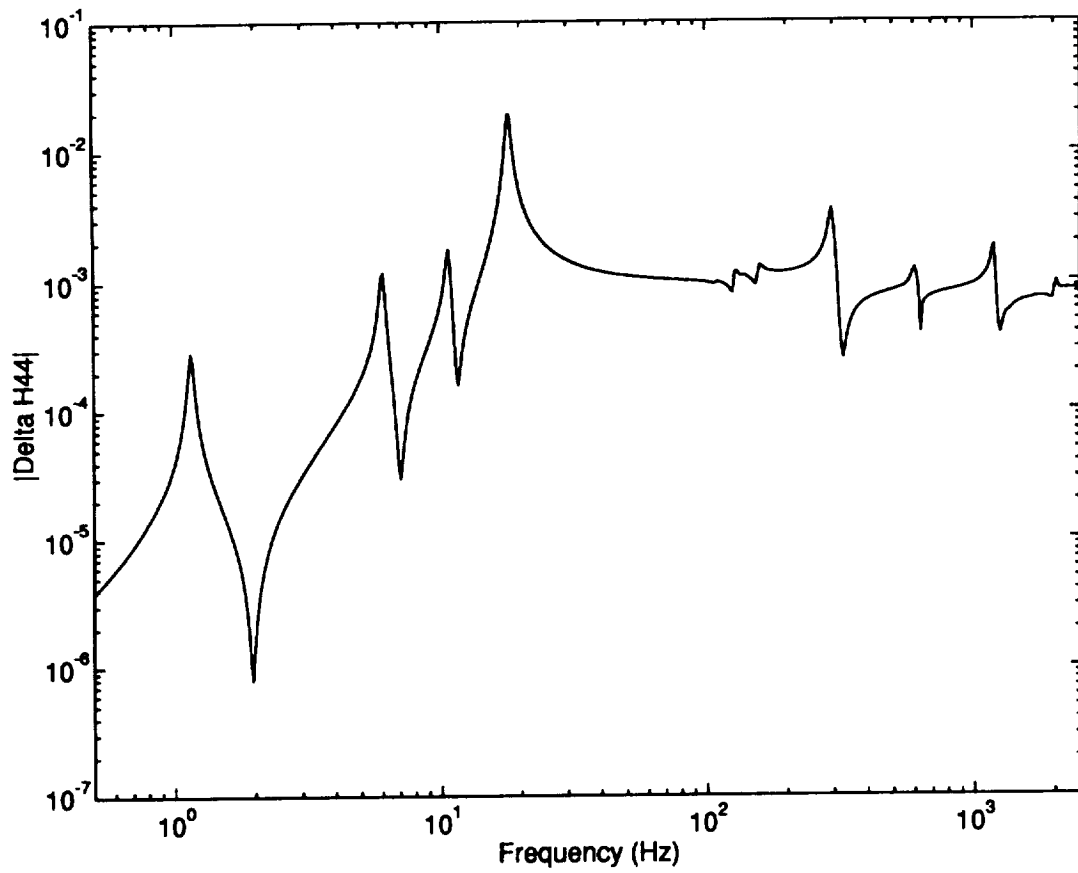
Figure 6.6: Difference between the Exact and Identified Drive-Point FRFs
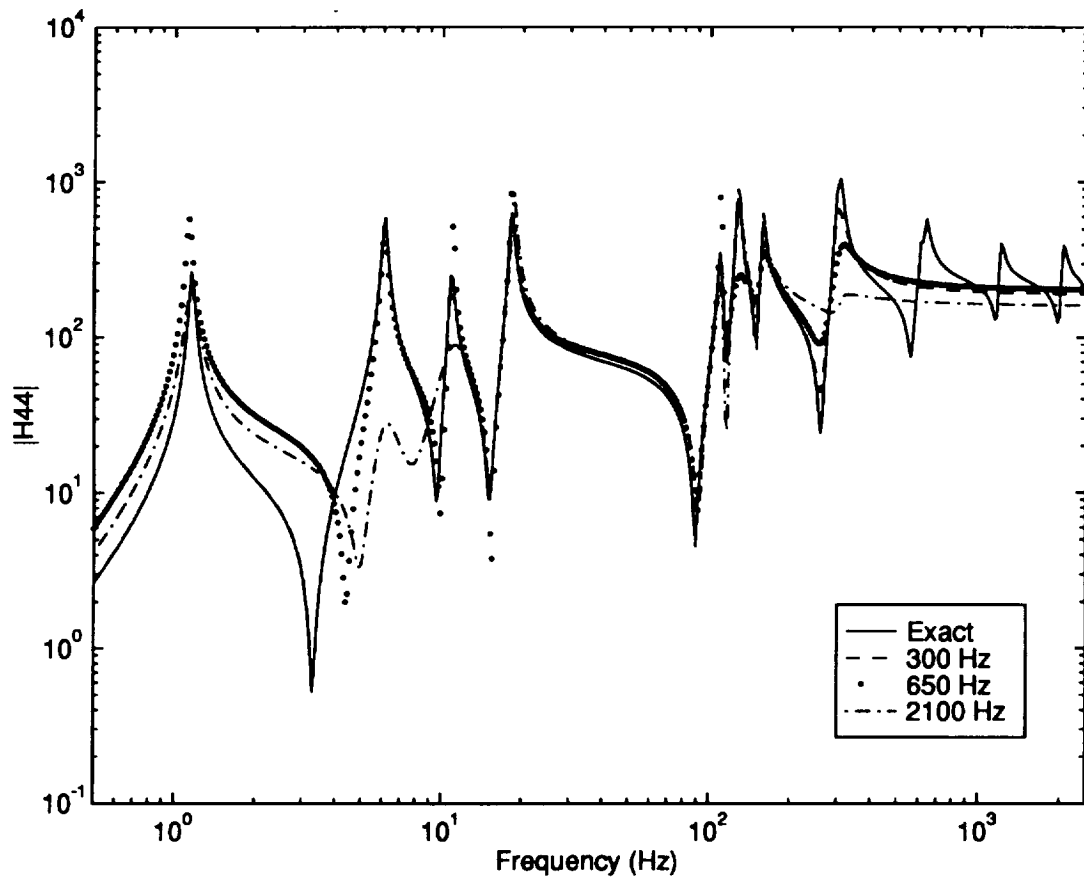
Figure 6.7: Comparison of FRFs for the 10-DOF Model vs Input Frequency Spectrum
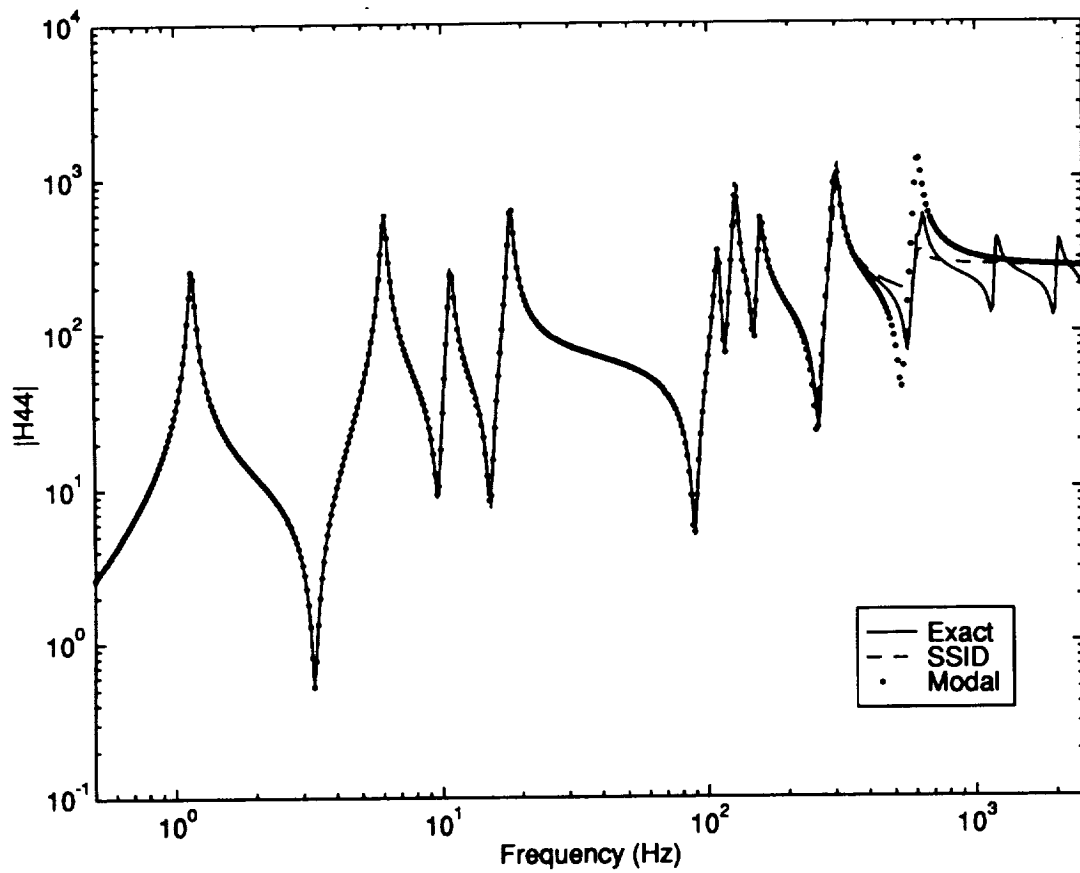
Figure 6.8: Comparison of FRFs Based on Two Different Identified Damping Matrices
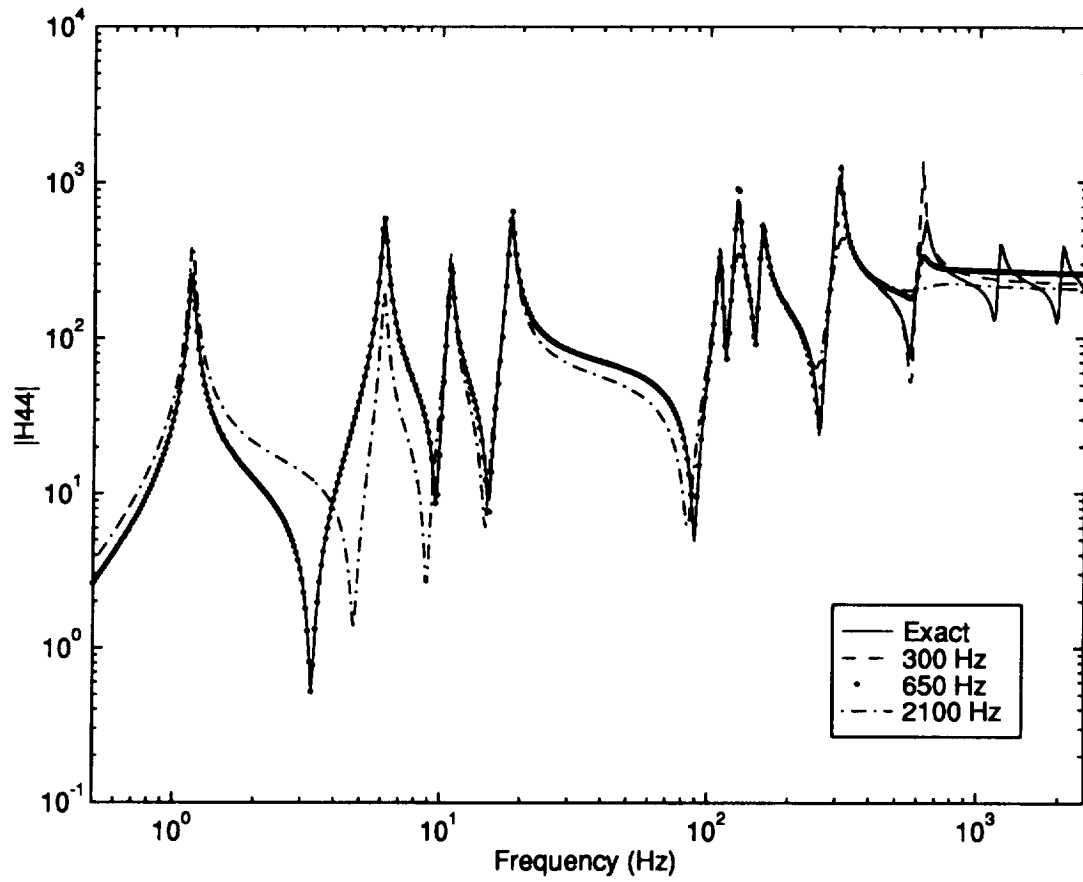
Figure 6.9: Comparison of FRFs for the 12-DOF Model vs Input Frequency
Spectrum
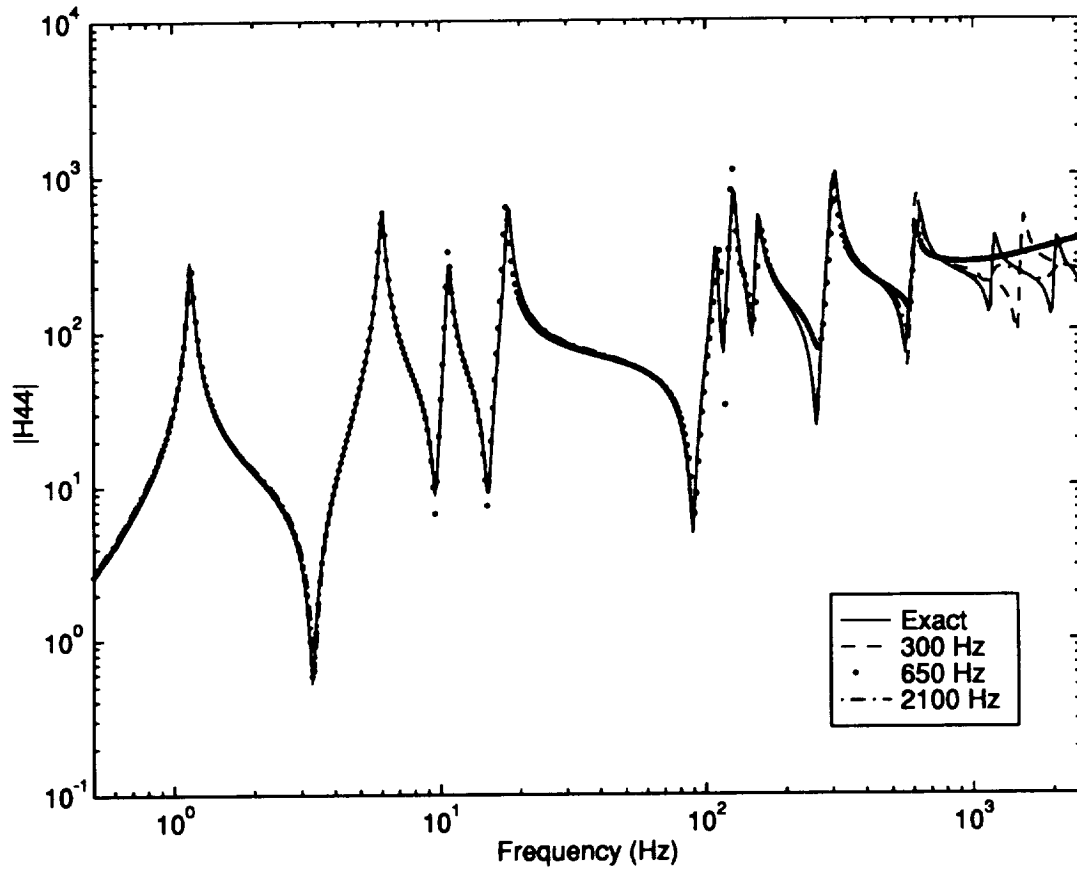
Figure 6.10: Comparison of FRFs for the 16-DOF Model vs Input Frequency Spectrum
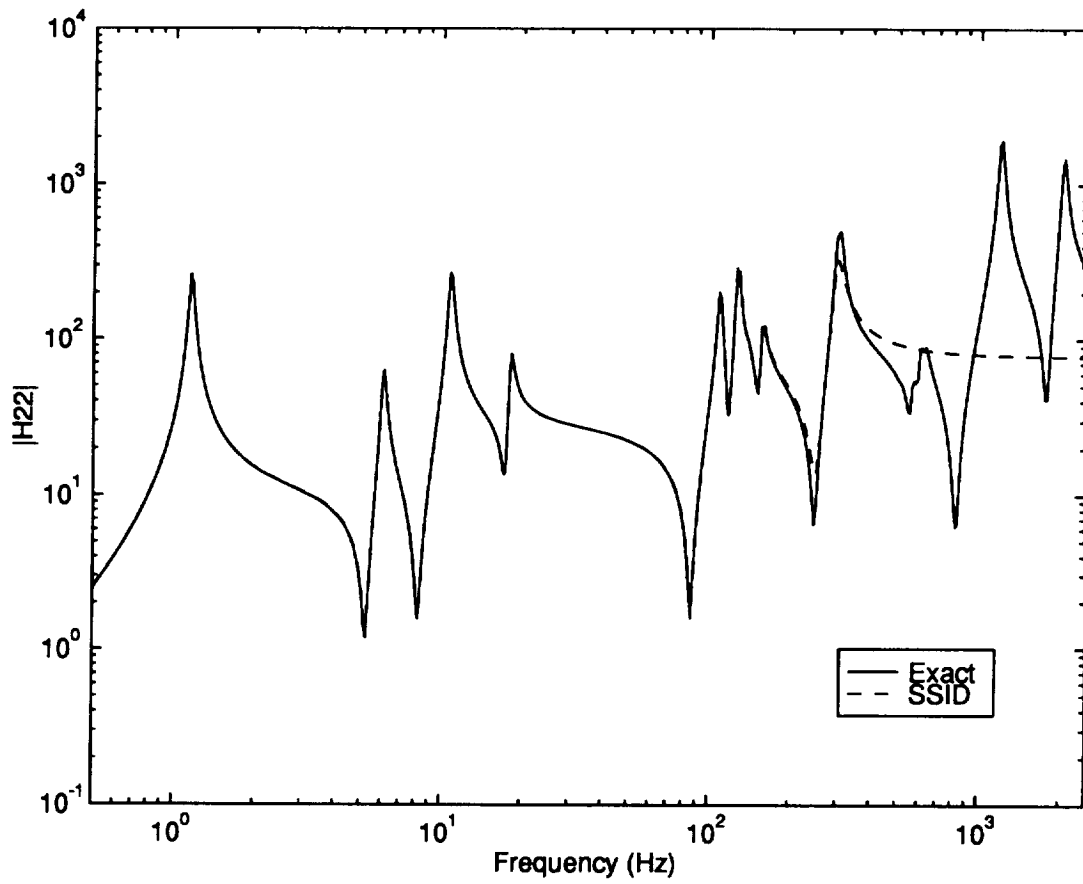
Figure 6.11: Comparison of Pseudo Drive-Point FRFs for 10-DOF Model
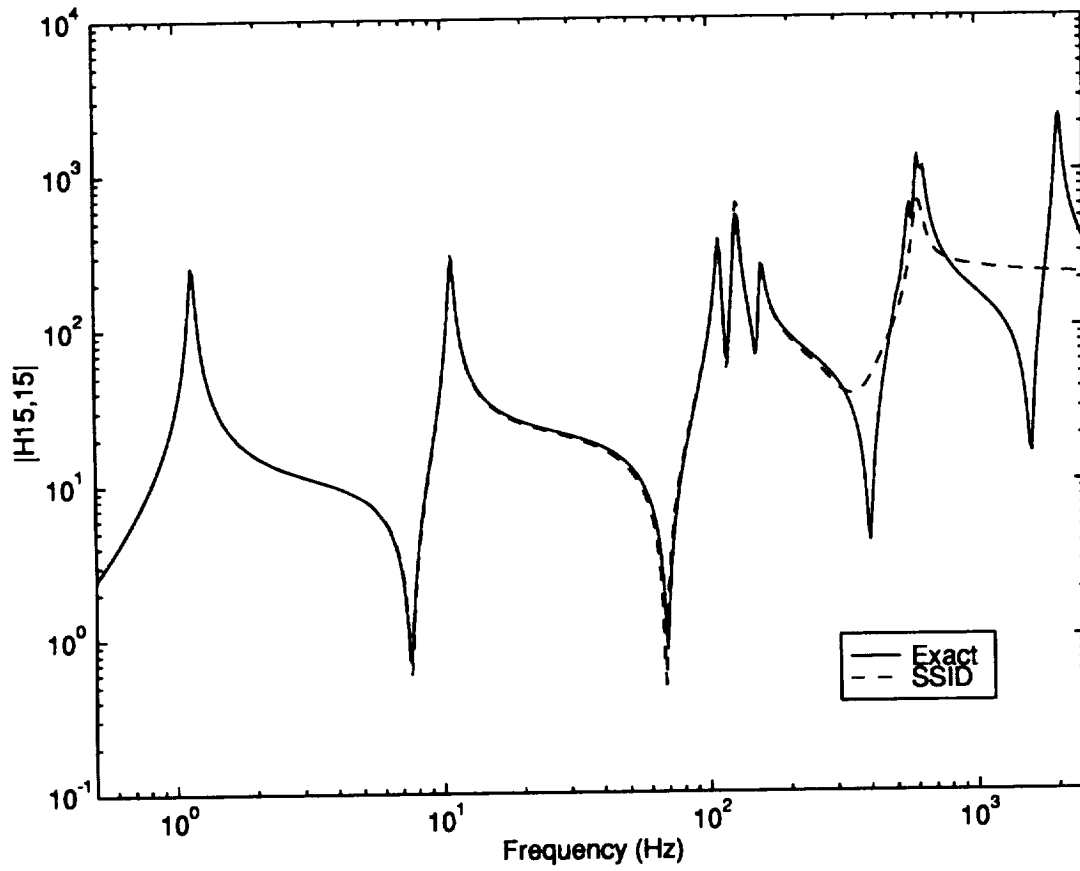
Figure 6.12: Comparison of Pseudo Drive-Point FRFs for 12-DOF Model
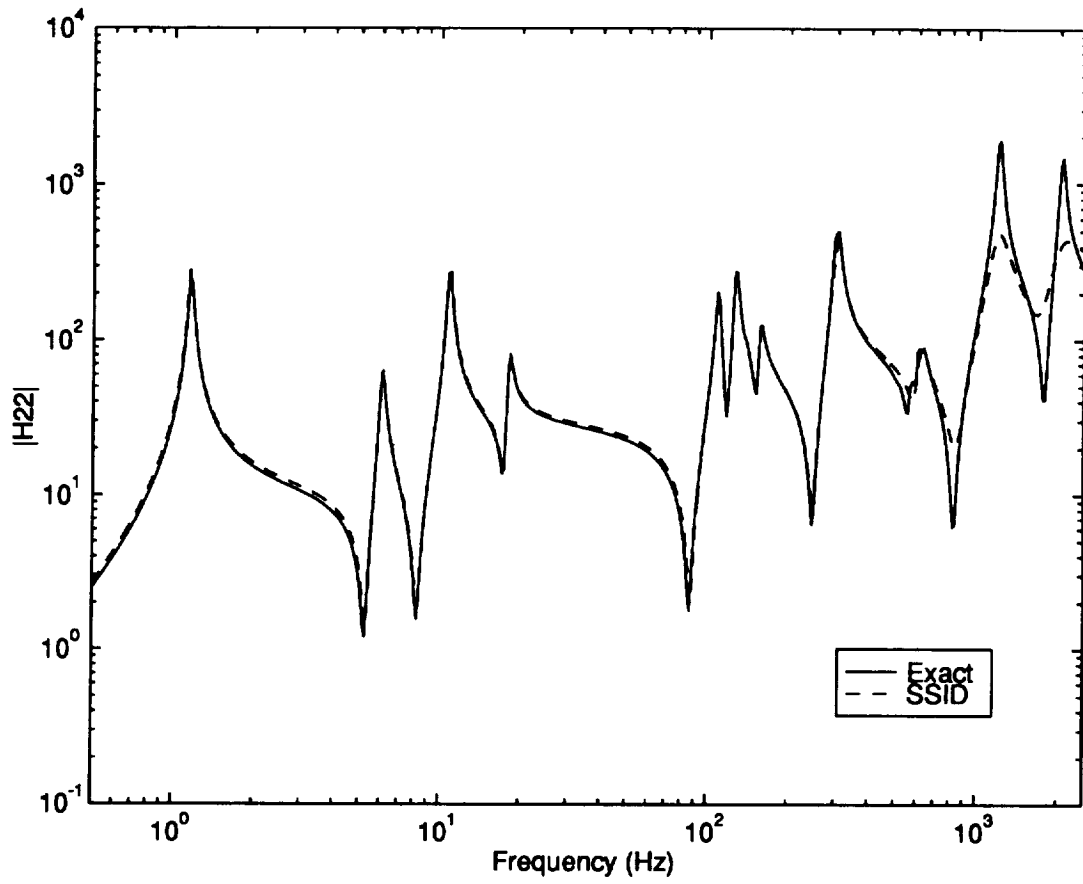
Figure 6.13: Comparison of Pseudo Drive-Point FRFs for 16-DOF Model
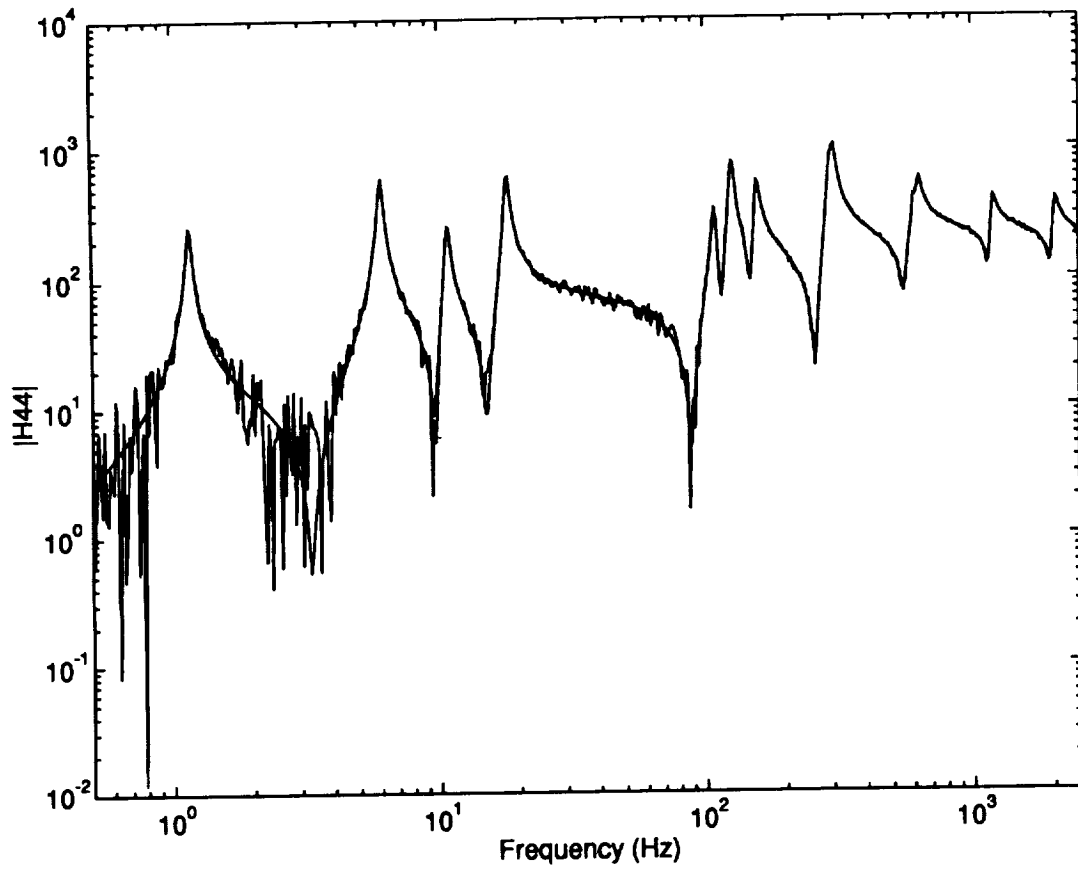
Figure 6.14: Typical "Measured" FRF with Added Noise
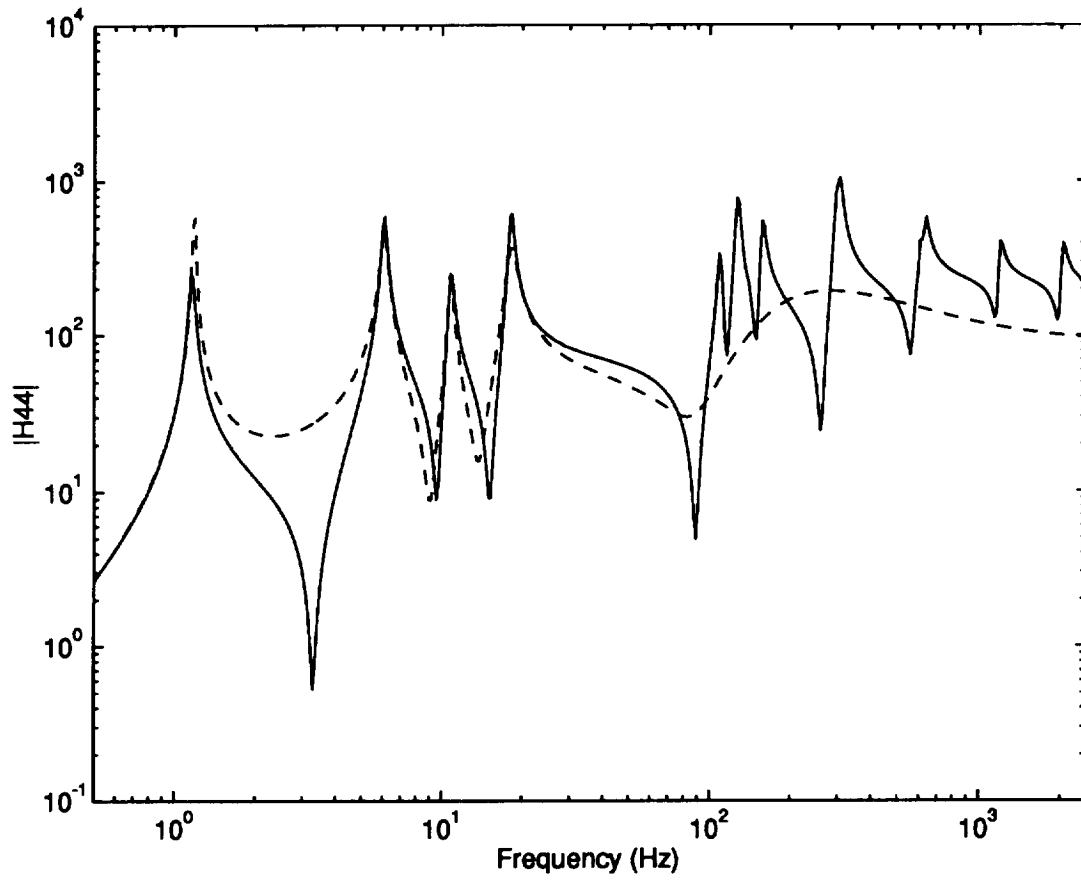
Figure 6.15: A Least Squares Solution in the Presence of Noise
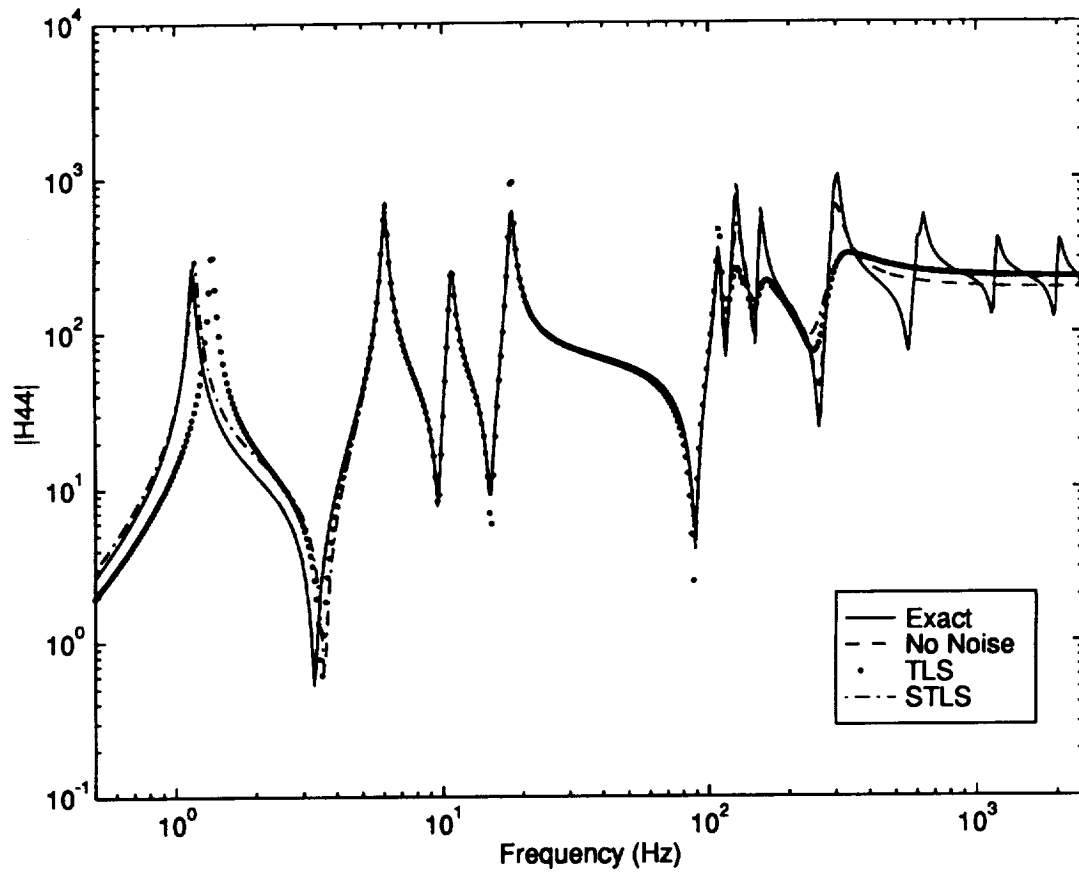
Figure 6.16: Comparison of FRFs of 10-DOF Model vs Solution Method
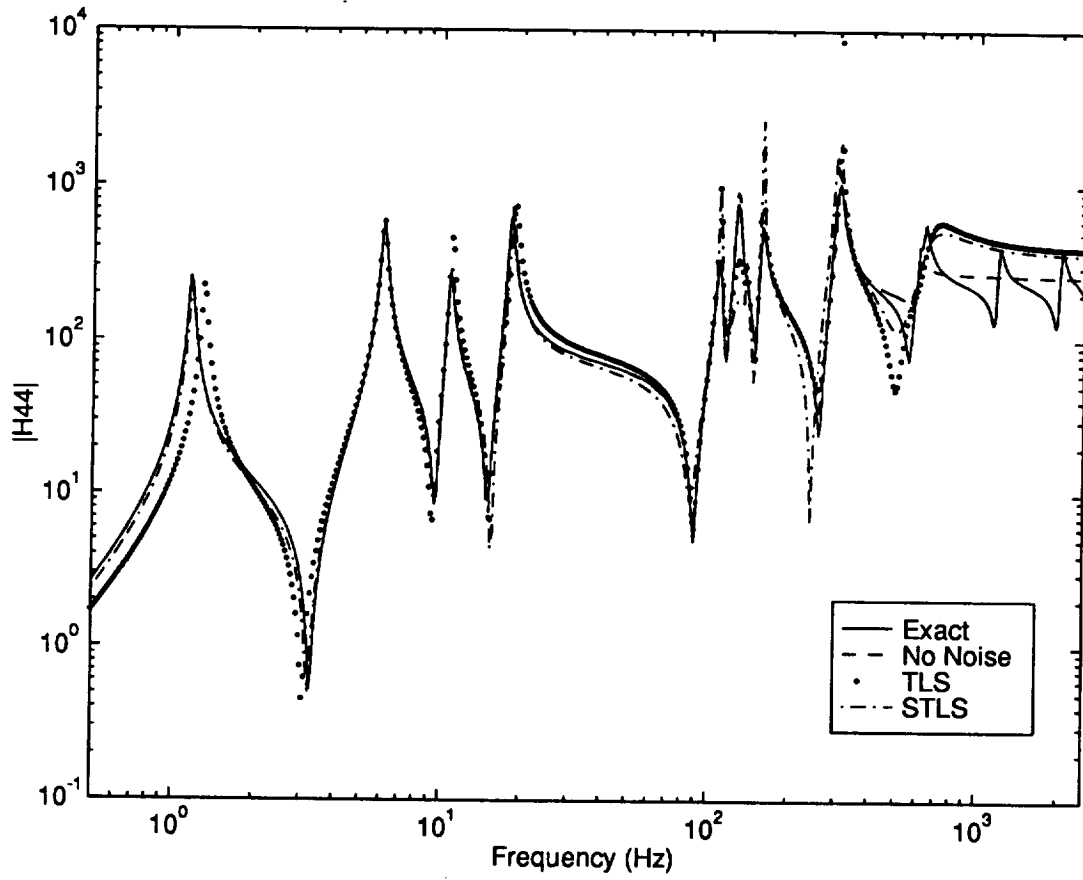
Figure 6.17: Comparison of FRFs of 12-DOF Model vs Solution Method
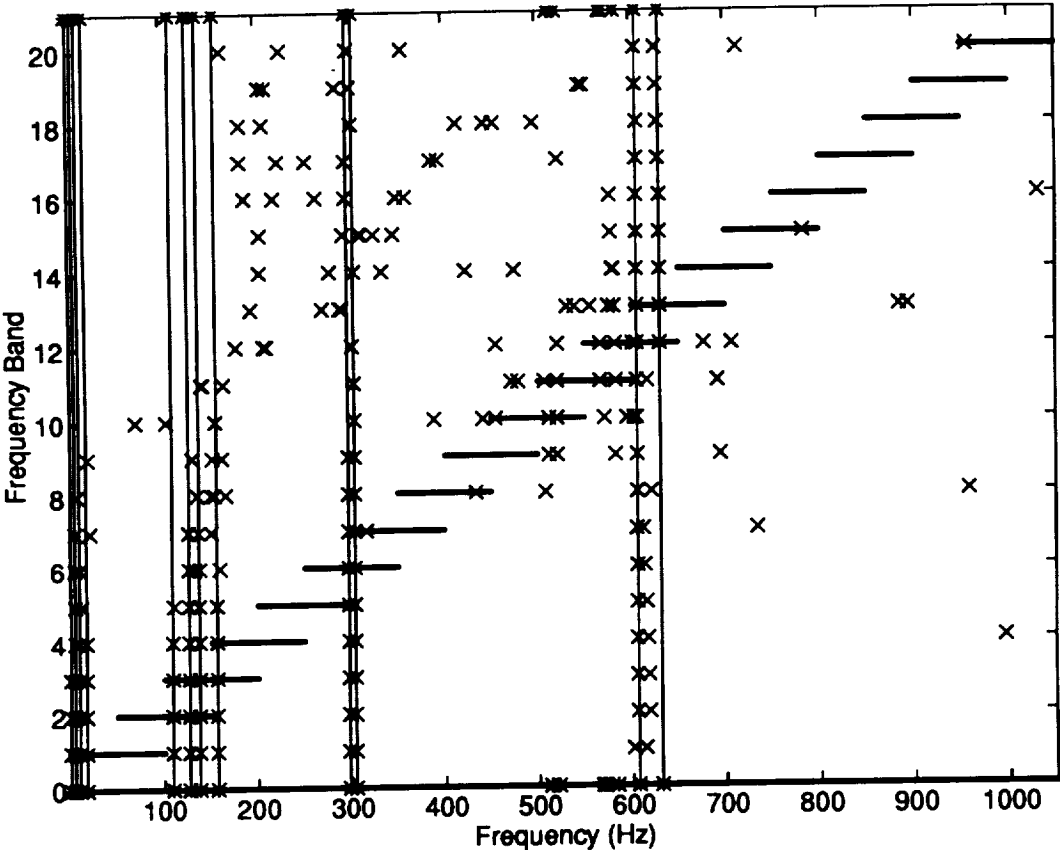
Figure 6.18: Estimated Natural Frequencies of 16-DOF Noise-Free Model Employing Band Processing
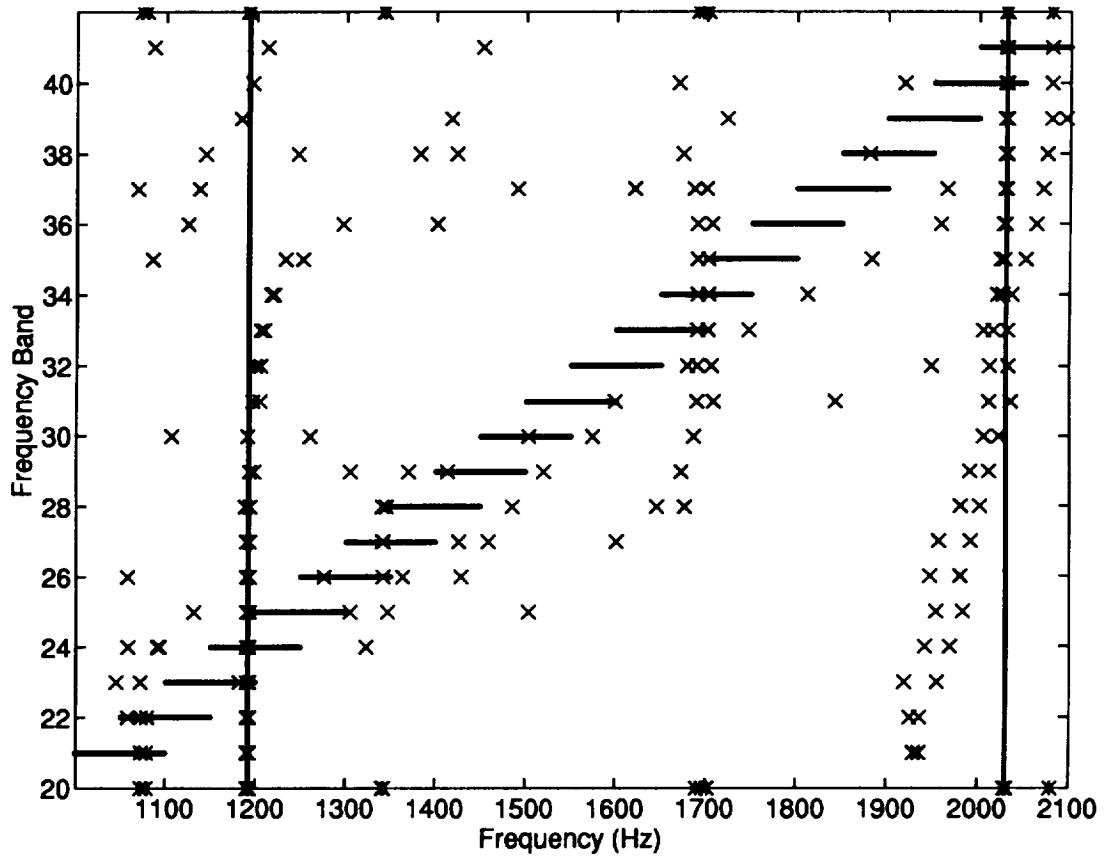
Figure 6.19: Estimated Natural Frequencies of 16-DOF Noise-Free Model Employing Band Processing (continued)
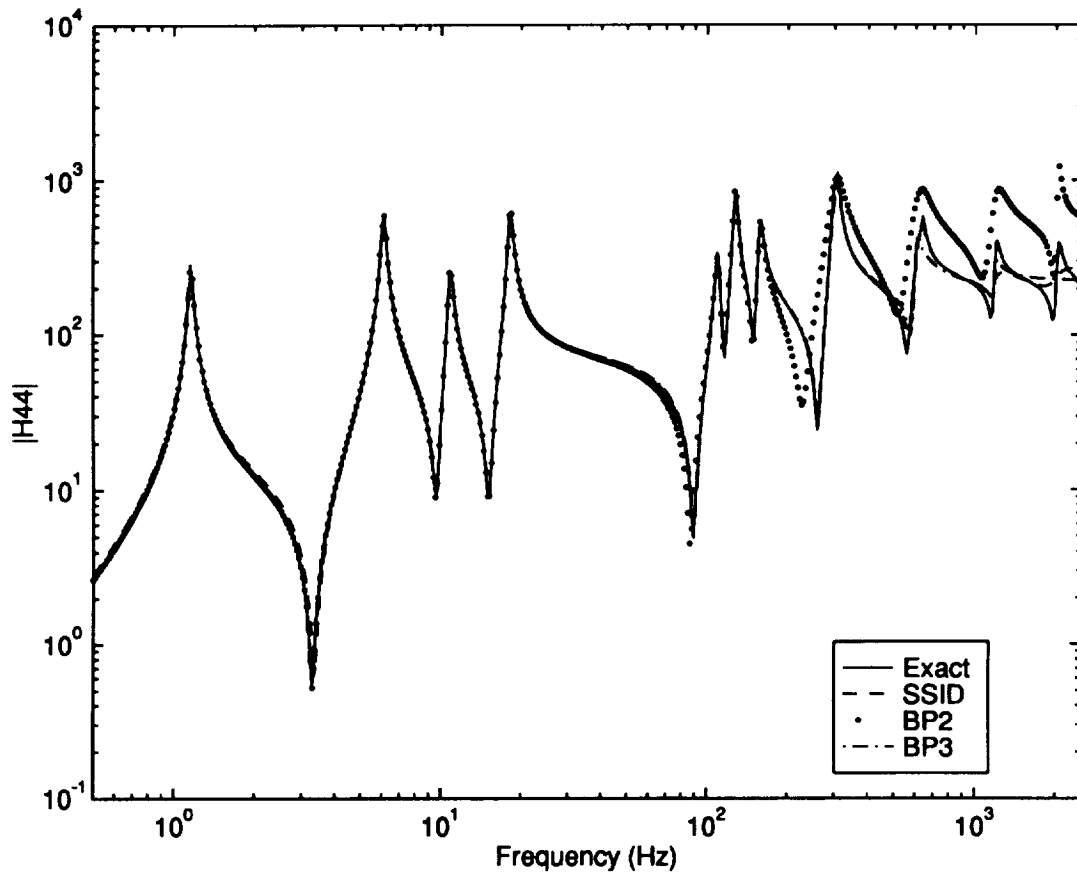
Figure 6.20: Comparison of FRFs of 16-DOF Noise-Free Model Using Band Processing
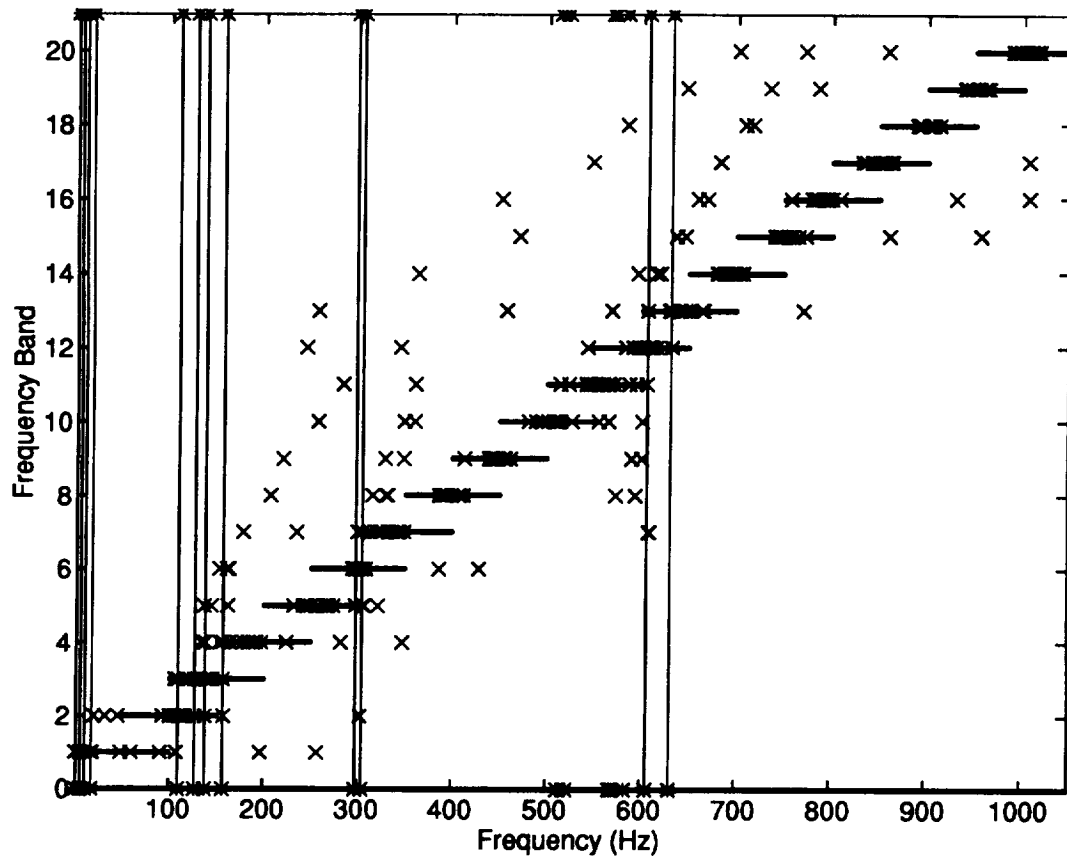
Figure 6.21: Estimated Natural Frequencies: Band Processing Using Noisy Data
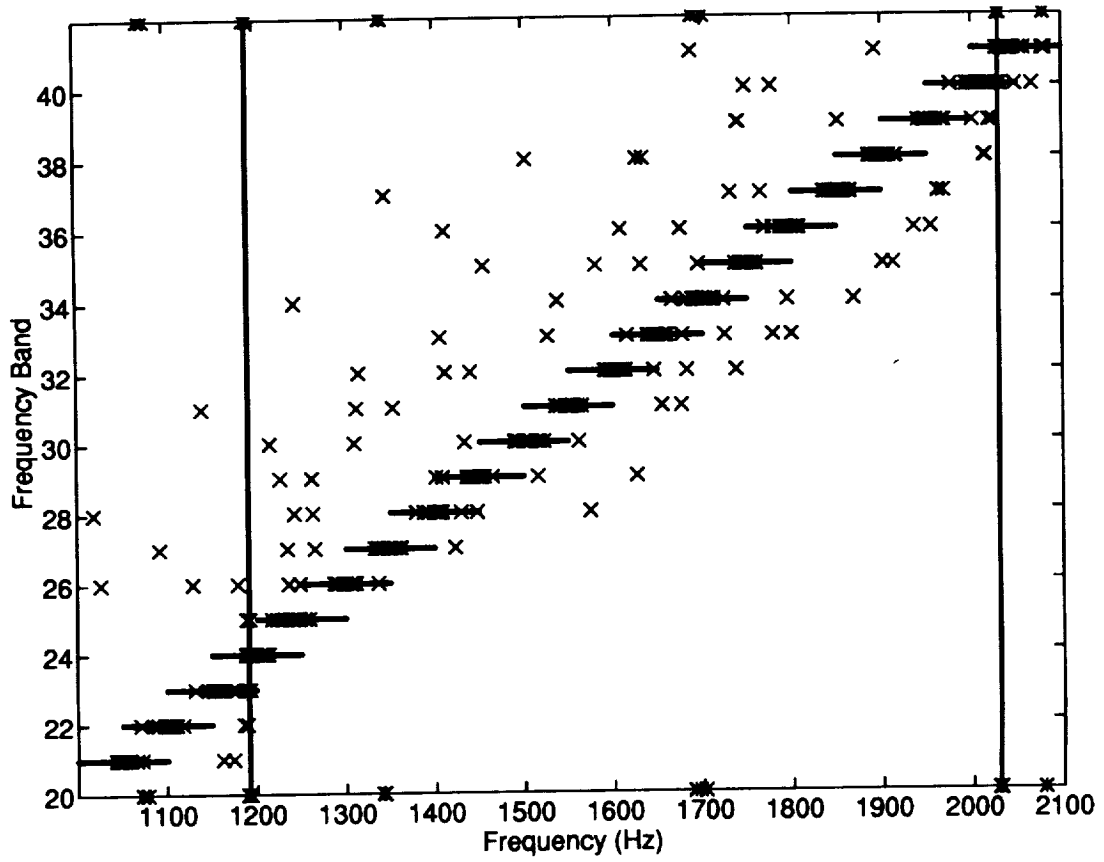
Figure 6.22: Estimated Natural Frequencies: Band Processing Using Noisy Data (continued)
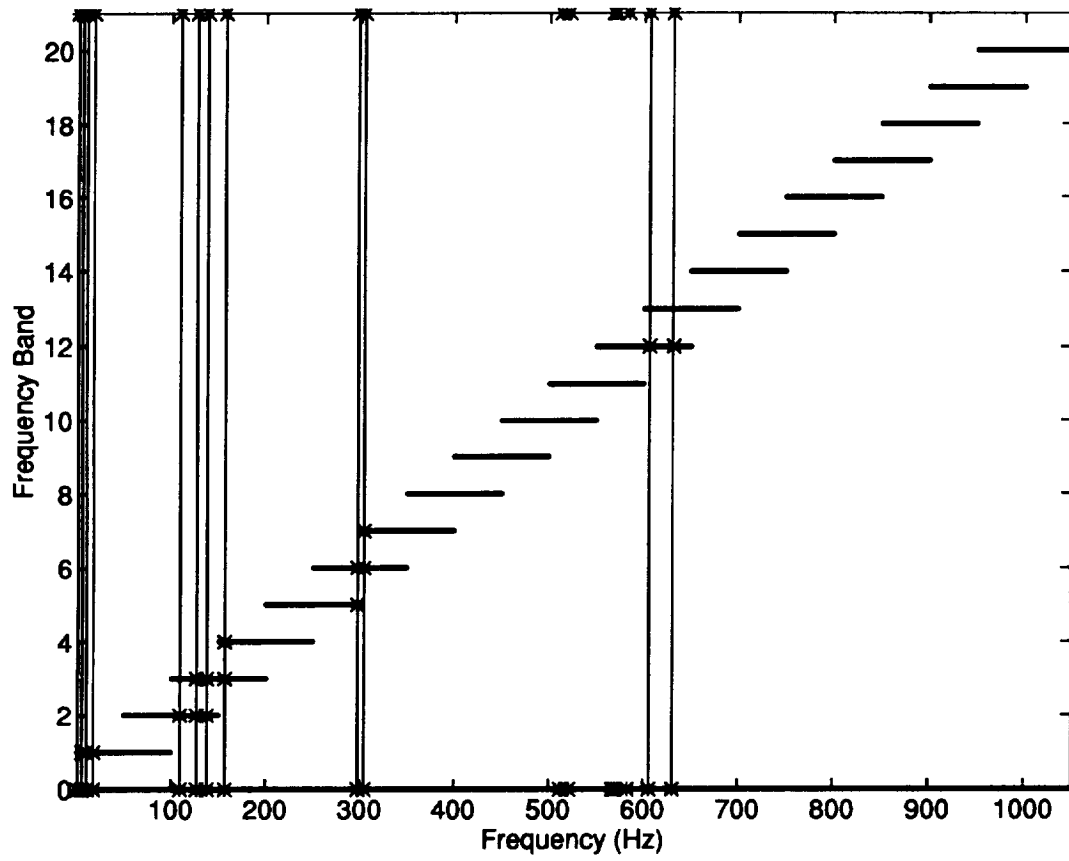
Figure 6.23: Estimated Natural Frequencies After Mode Selection: Band Processing Using Noisy Data
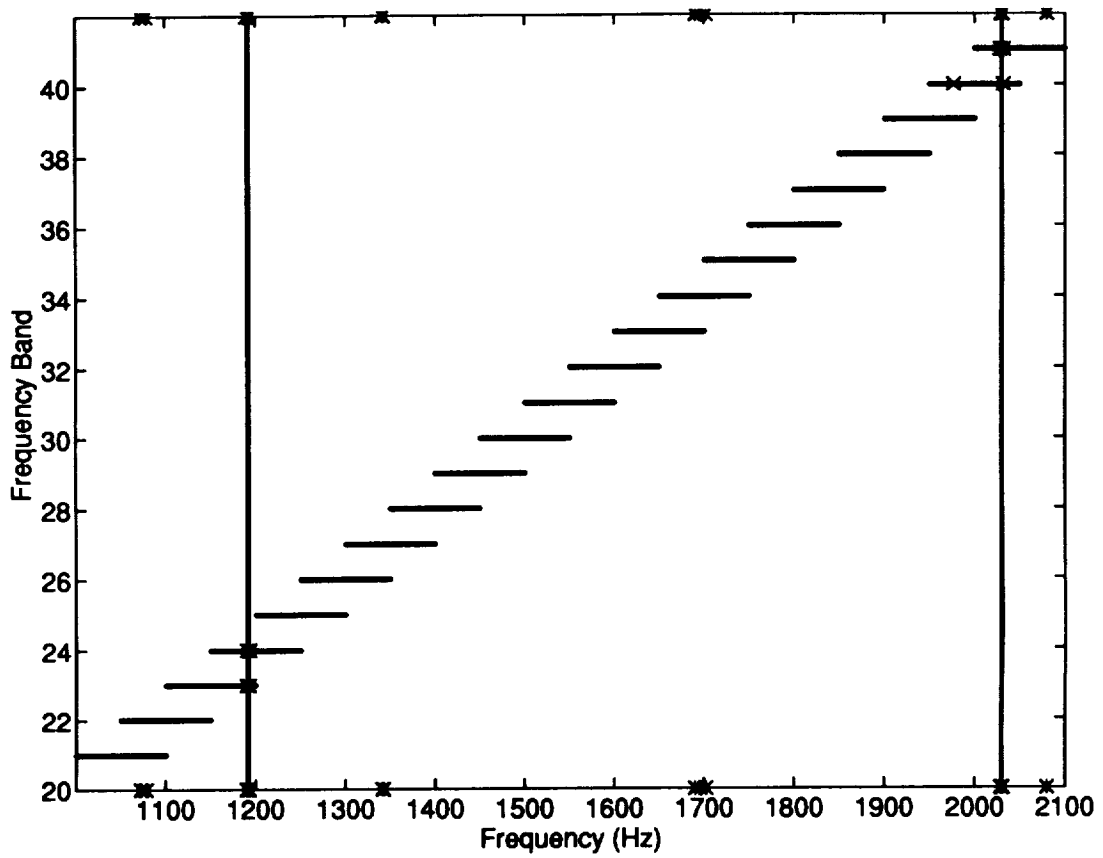
Figure 6.24: Estimated Natural Frequencies After Mode Selection: Band Processing Using Noisy Data (continued)
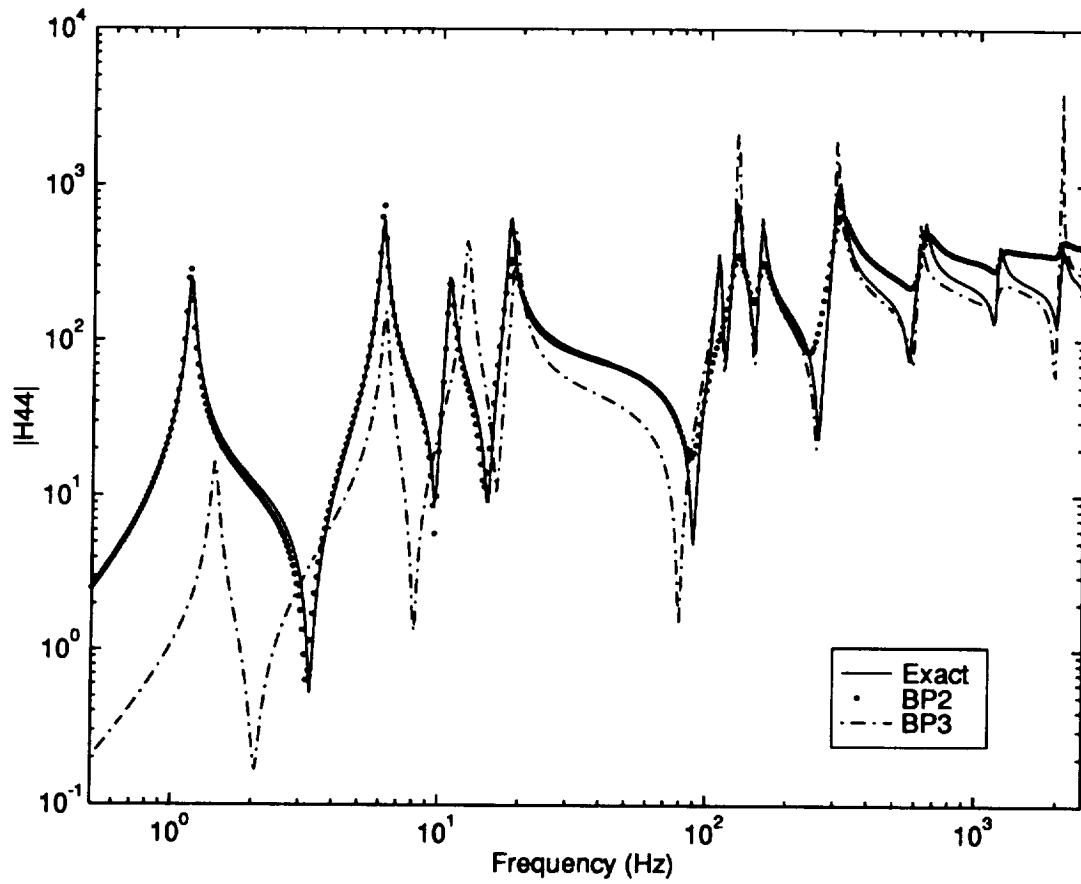
Figure 6.25: Comparison FRFs of 16-DOF Model Employing Band Processing with Noisy Data
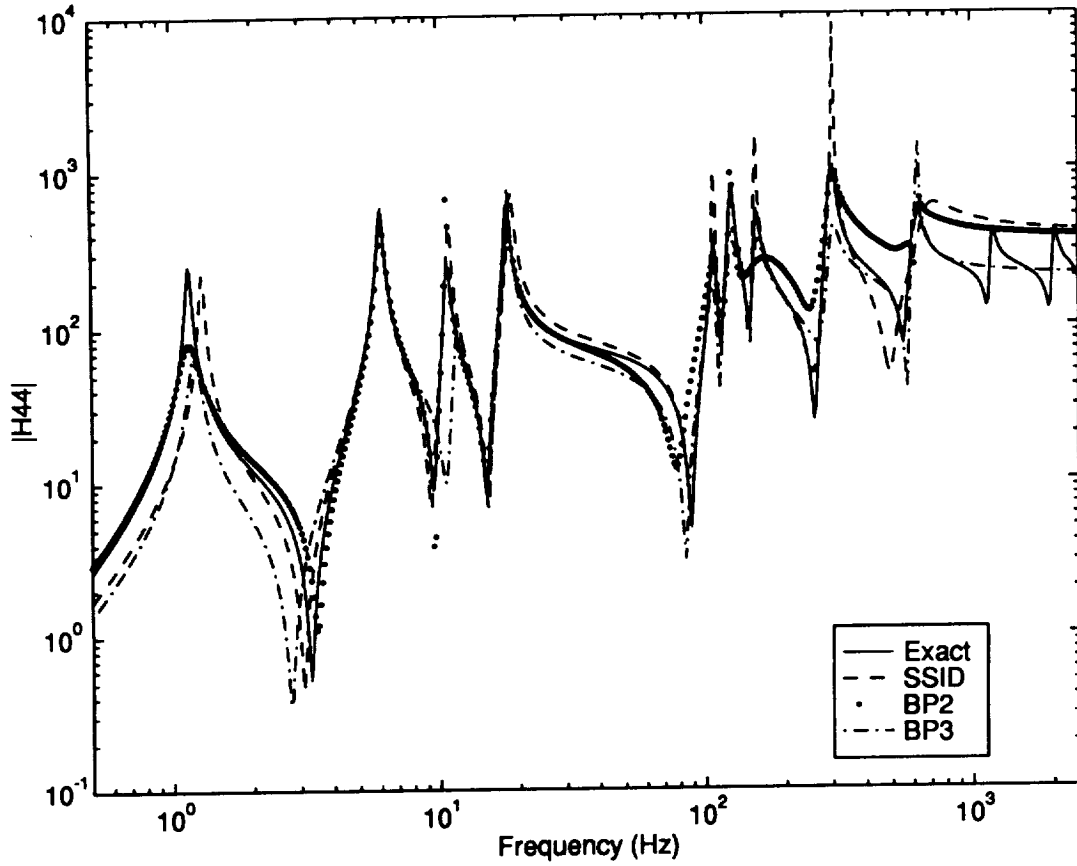
Figure 6.26: Comparison FRFs of 12 DOF Model Employing Band Processing with Noisy Data
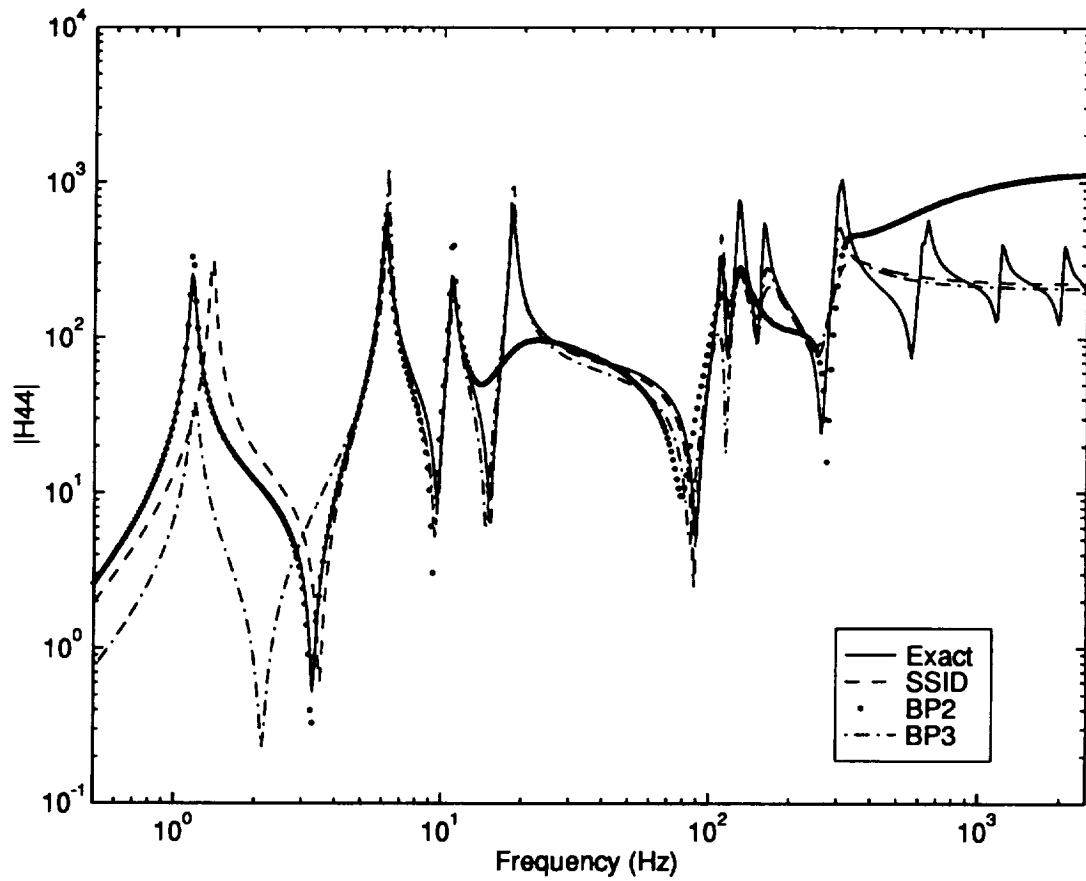
Figure 6.27: Comparison FRFs of 10 DOF Model Employing Band Processing with Noisy Data
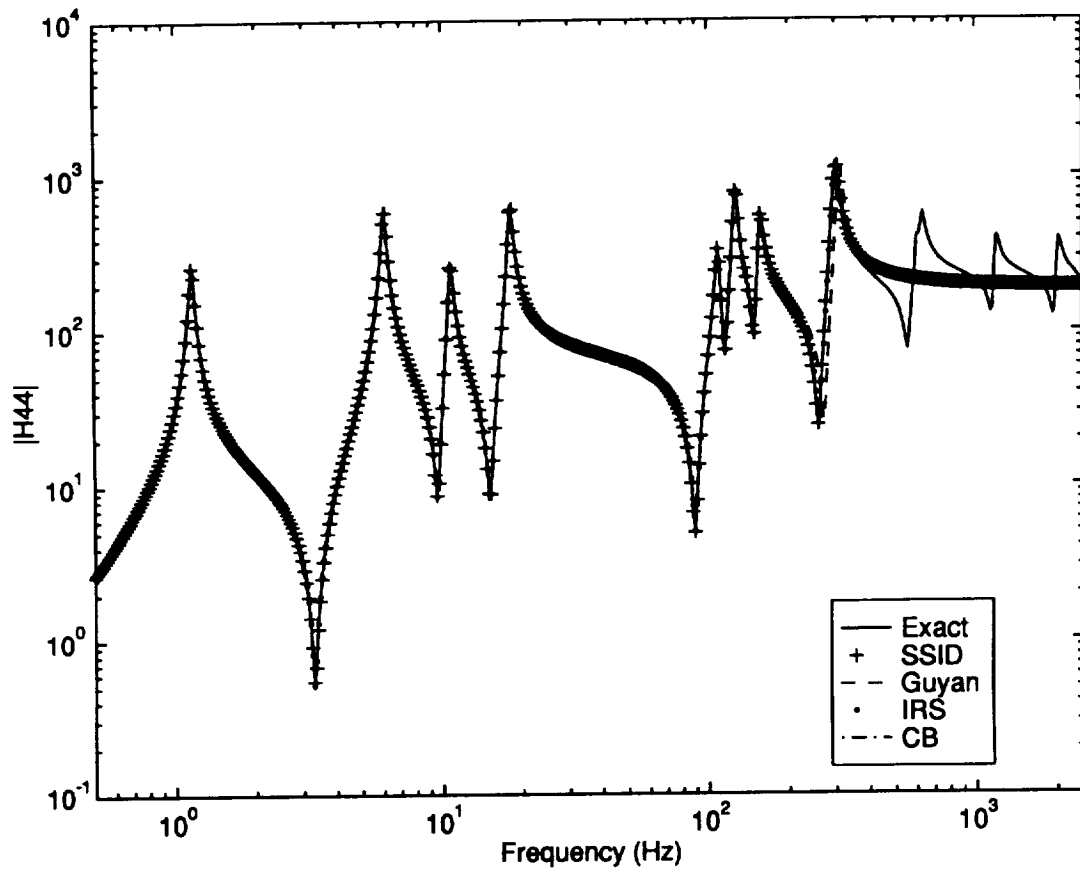
Figure 6.28: Comparison of FRFs for 10-DOF TAMs
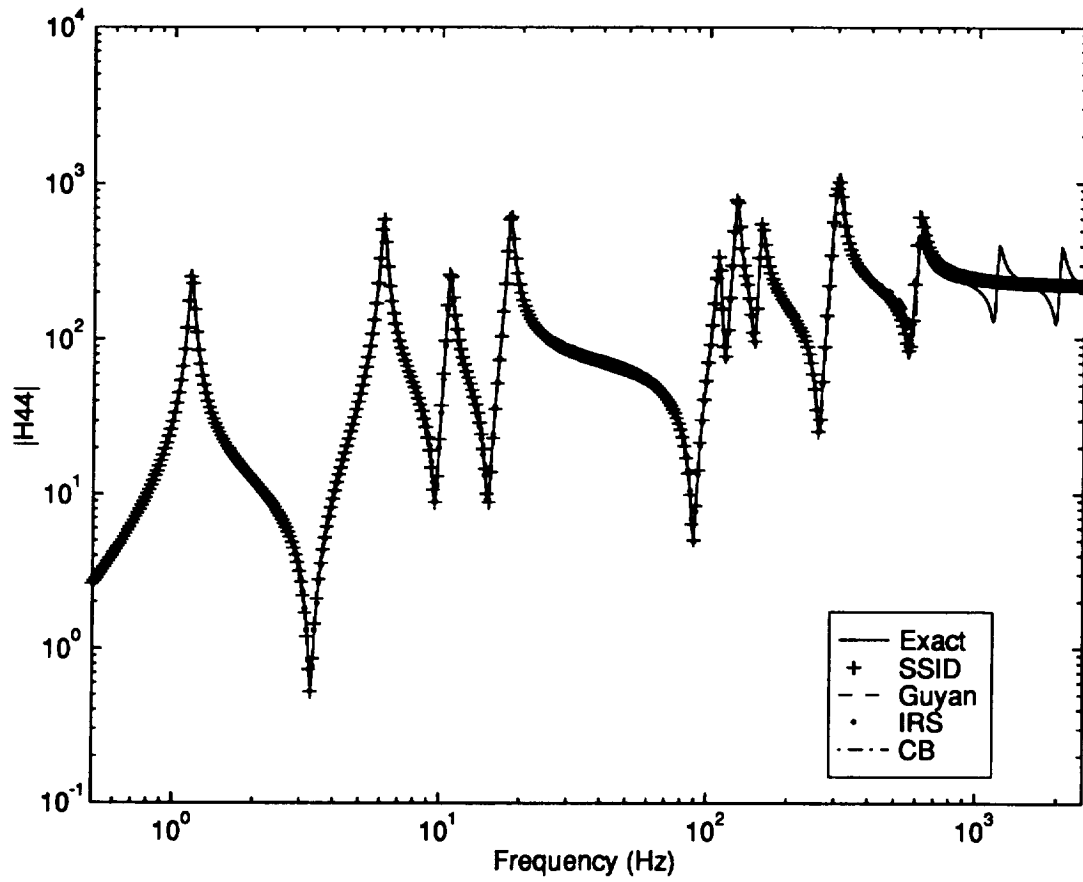
Figure 6.29: Comparison of FRFs for 12-DOF TAMs
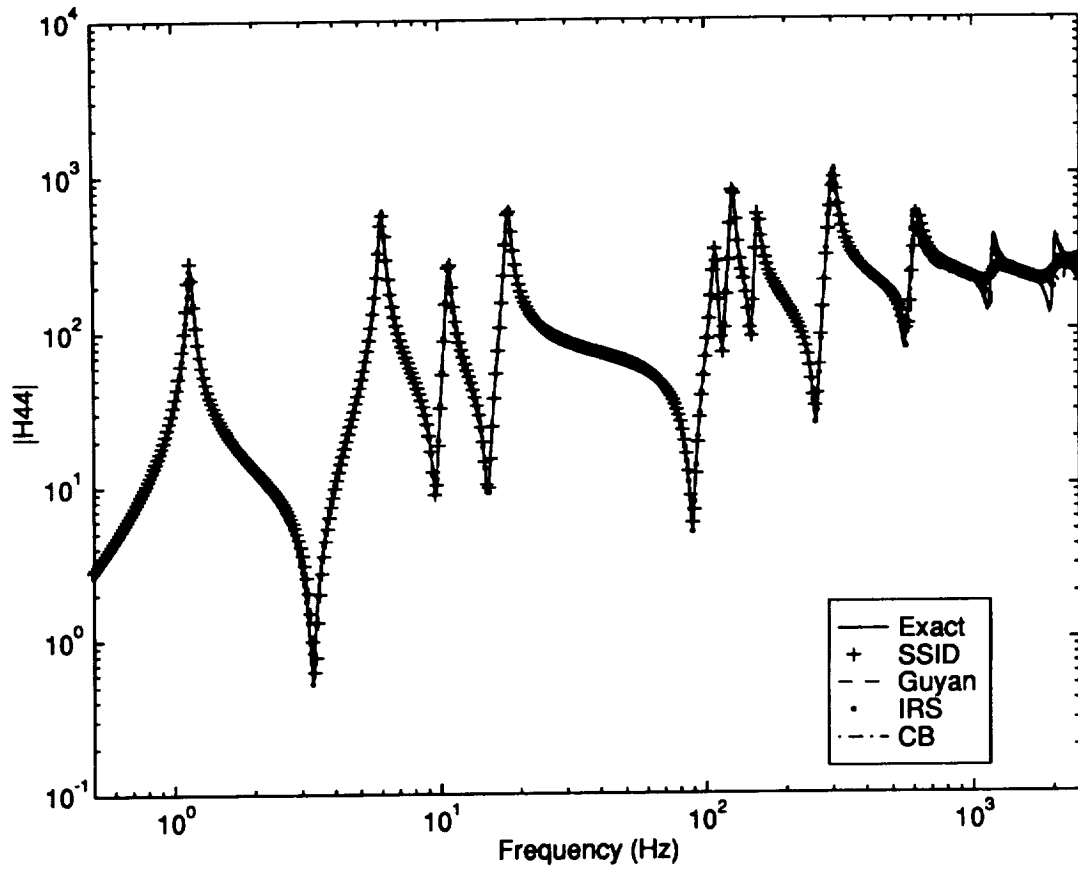
Figure 6.30: Comparison of FRFs for 16-DOF TAMs
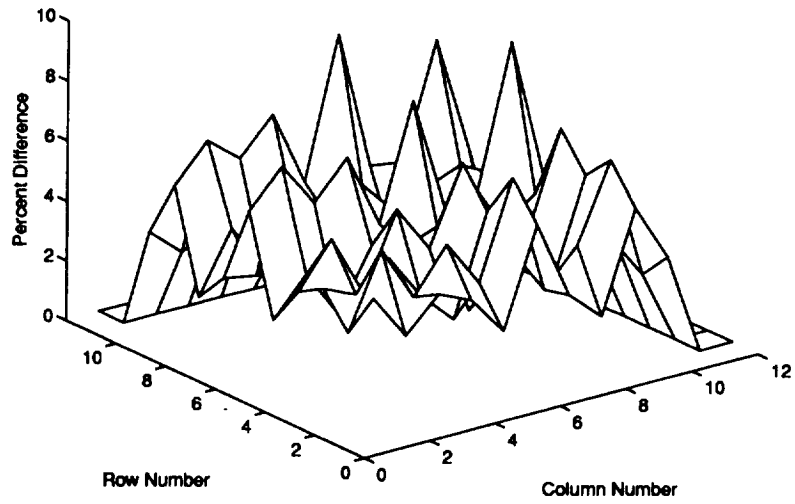
Figure 6.31: Comparison of Mass Matrices for the 12-DOF TAMs — IRS vs SSID
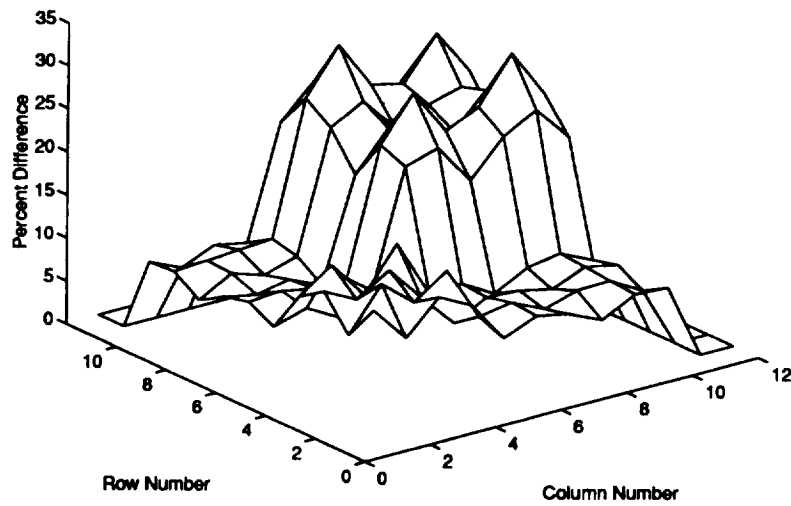


Figure 6.32: Comparison of Stiffness Matrices for the 12-DOF TAMs — IRS vs SSID
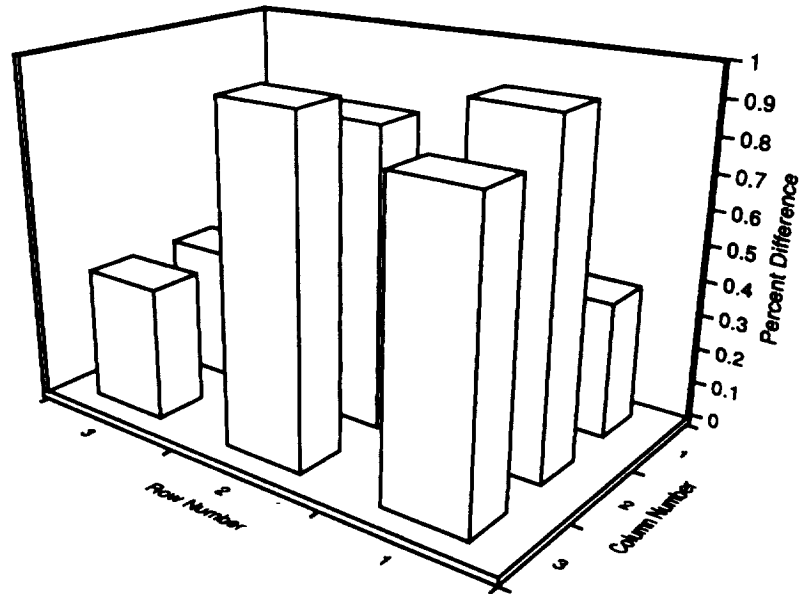
Figure 6.33: Comparison of the Constraint-Mode Partition of the C-B Stiffness
Matrix for the 10-DOF Model
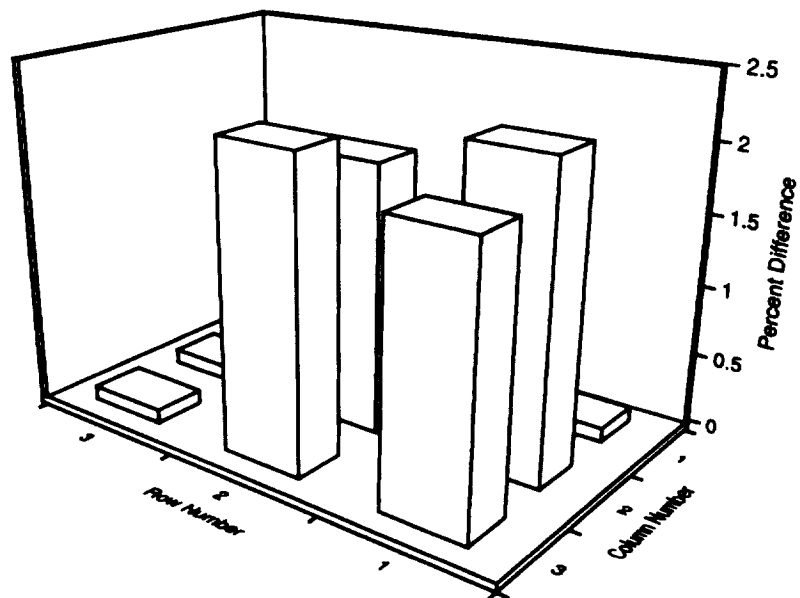


Figure 6.34: Comparison of the Constraint-Mode Partition of the C-B Stiffness
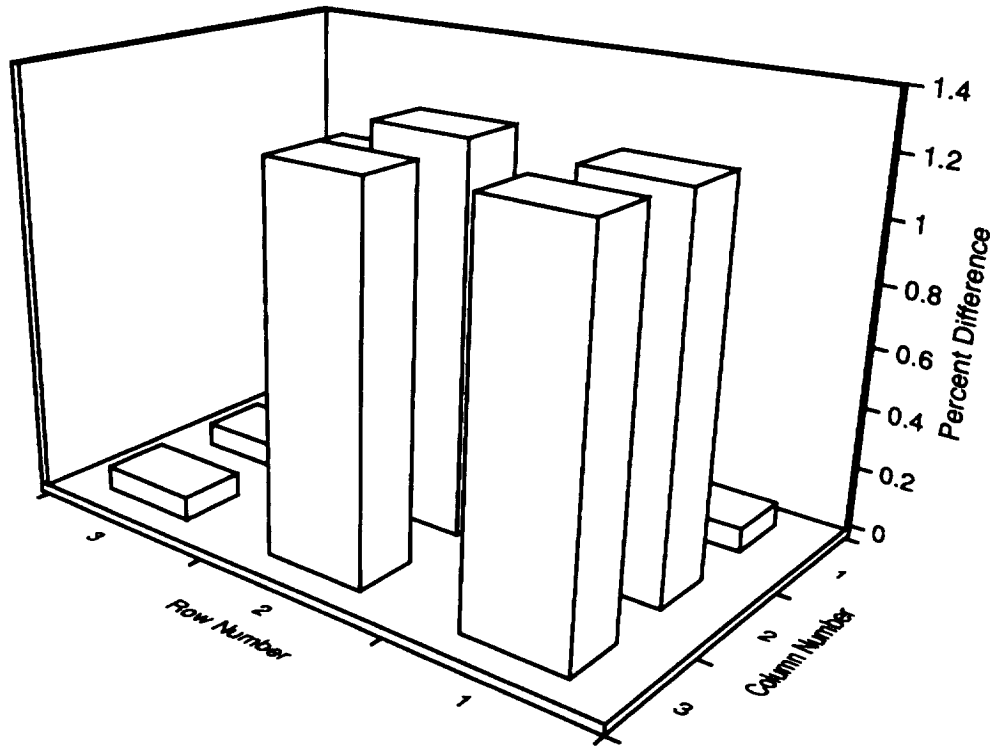Matrix for the 12-DOF Model

Figure 6.35: Comparison of the Constraint-Mode Partition of the C-B Stiffness Matrix for the 16-DOF Model
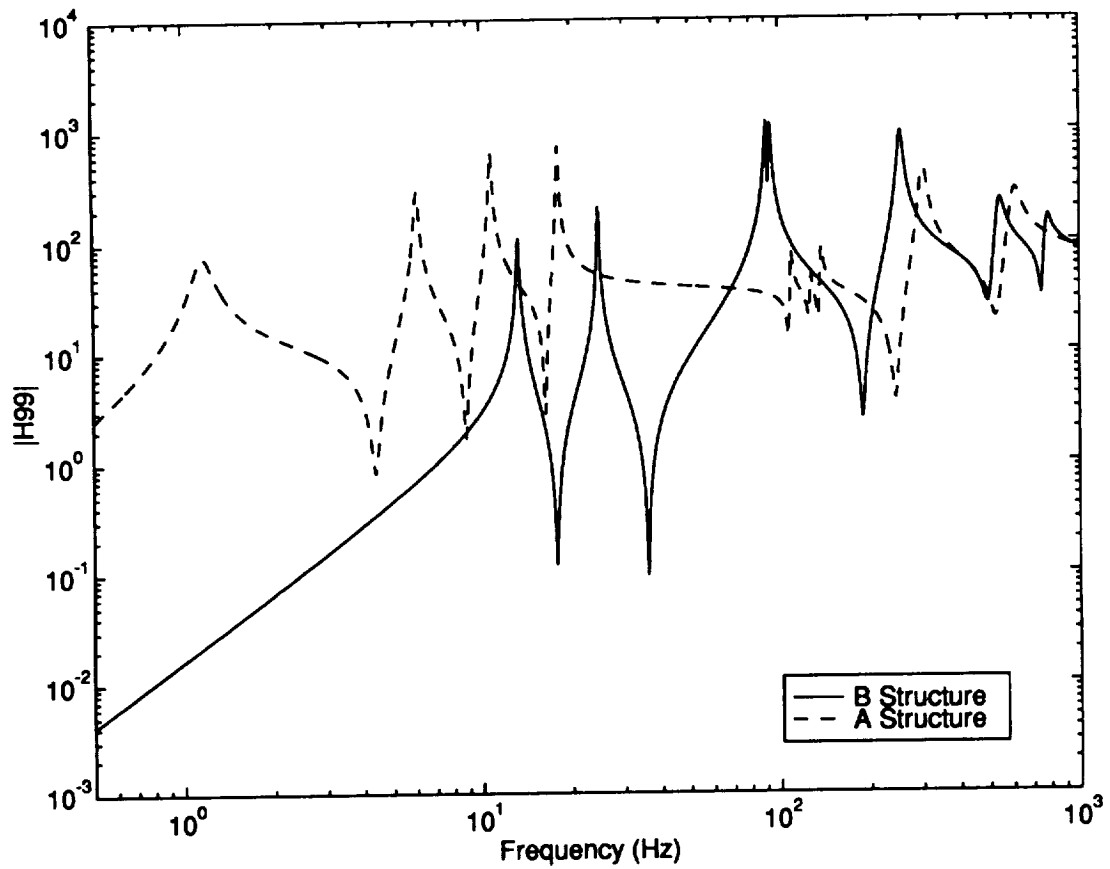
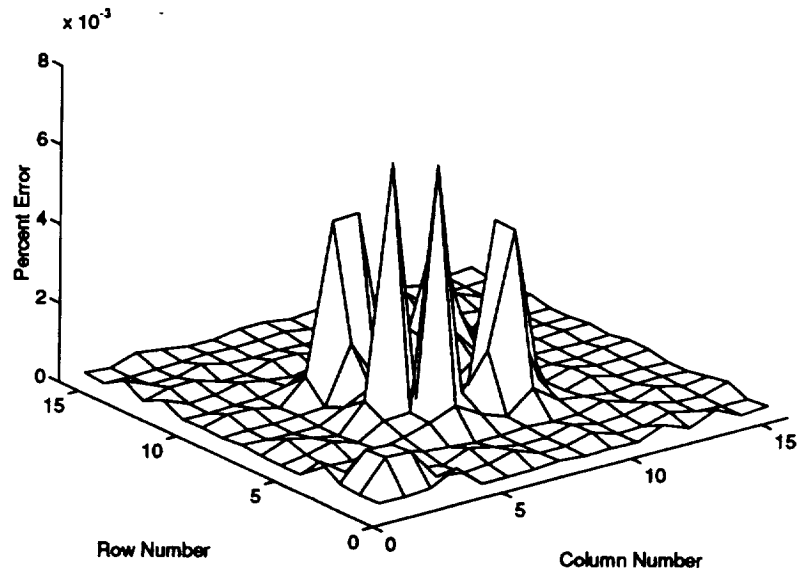Figure 6.36: Comparison of FRFs for the Coupled System and for the Substructure Alone

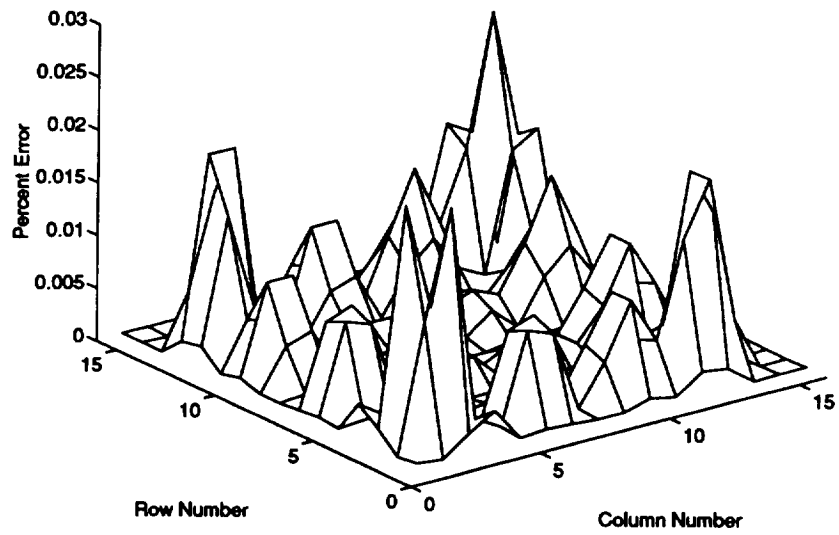Figure 6.37: Percent Error in the SSID-Estimated Mass Matrix



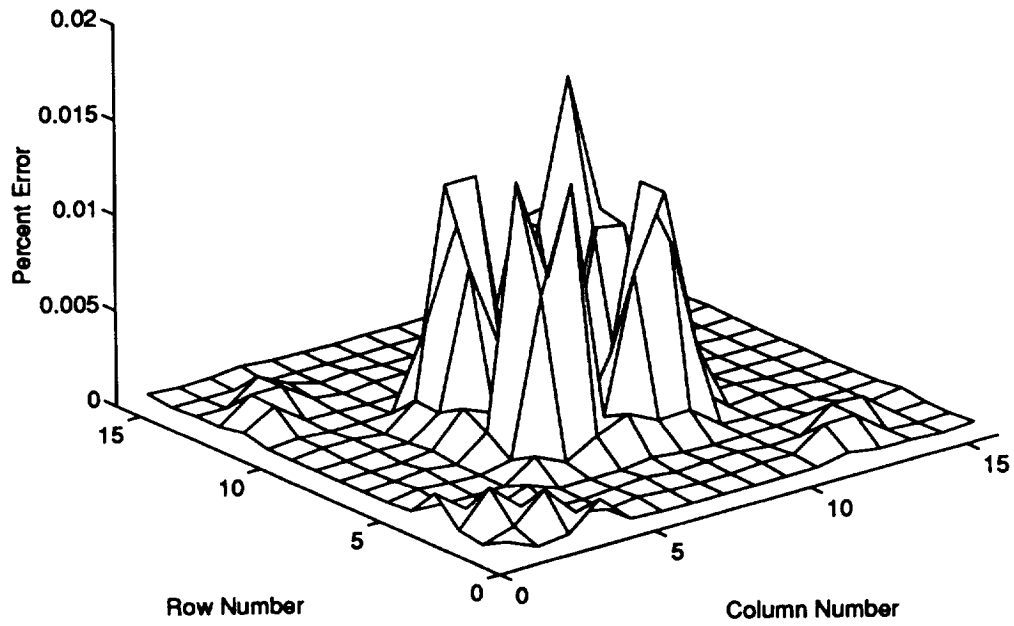Figure 6.38: Percent Error in the SSID-Estimated Damping Matrix

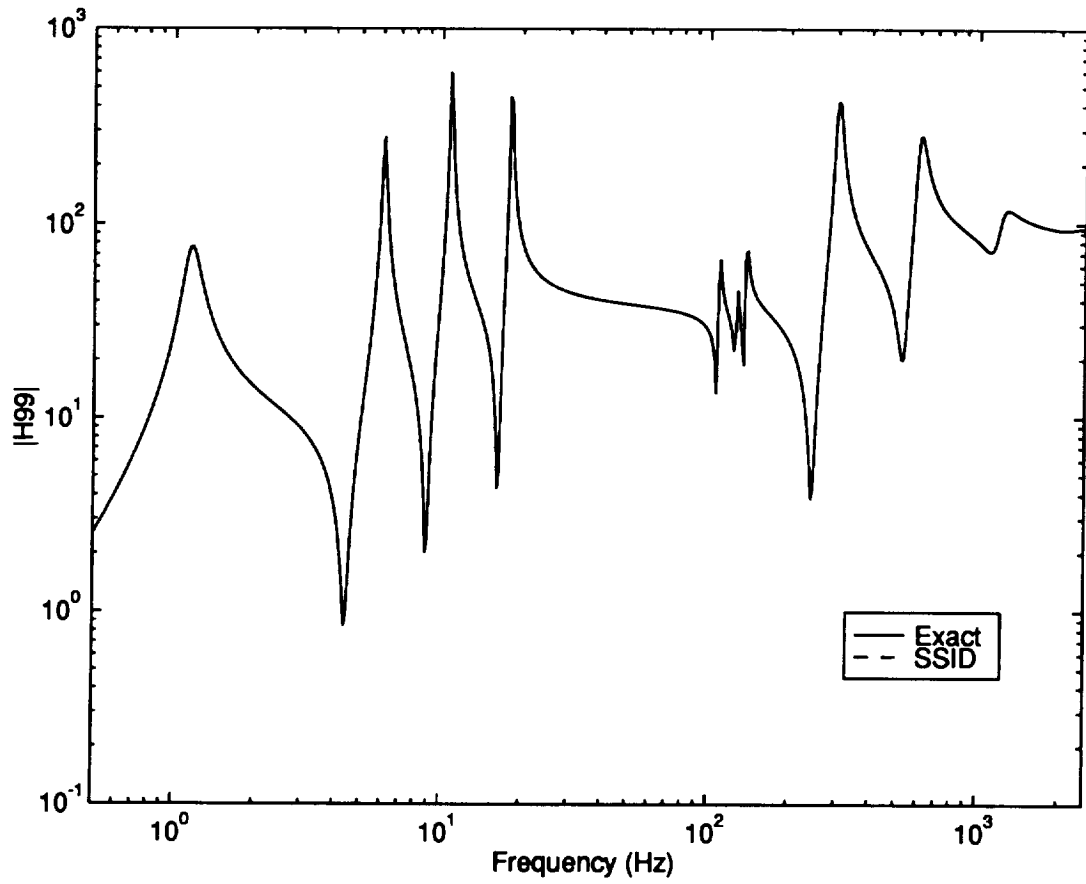Figure 6.39: Percent Error in the SSID-Estimated Stiffness Matrix

Figure 6.40: Comparison of Drive-Point FRFs with Reaction Forces Included
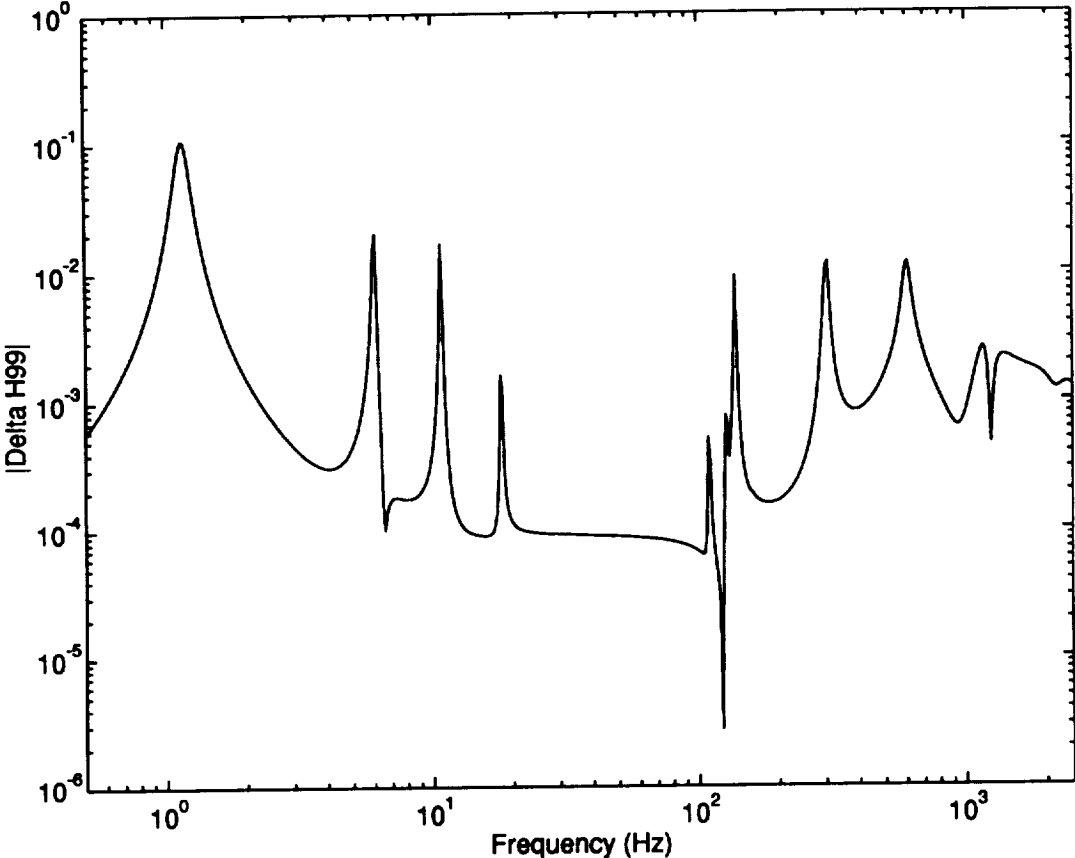
Figure 6.41: Difference Between the Exact and Identified FRFs with Reaction Forces Included
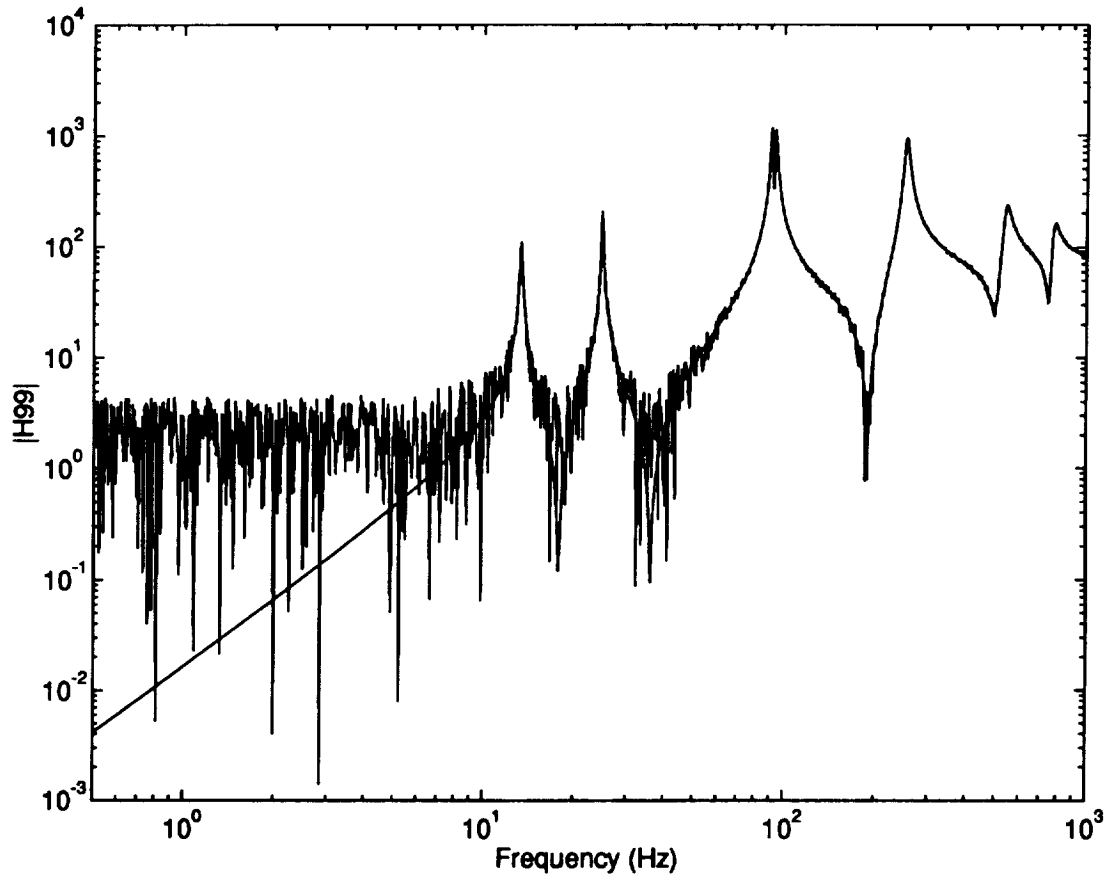
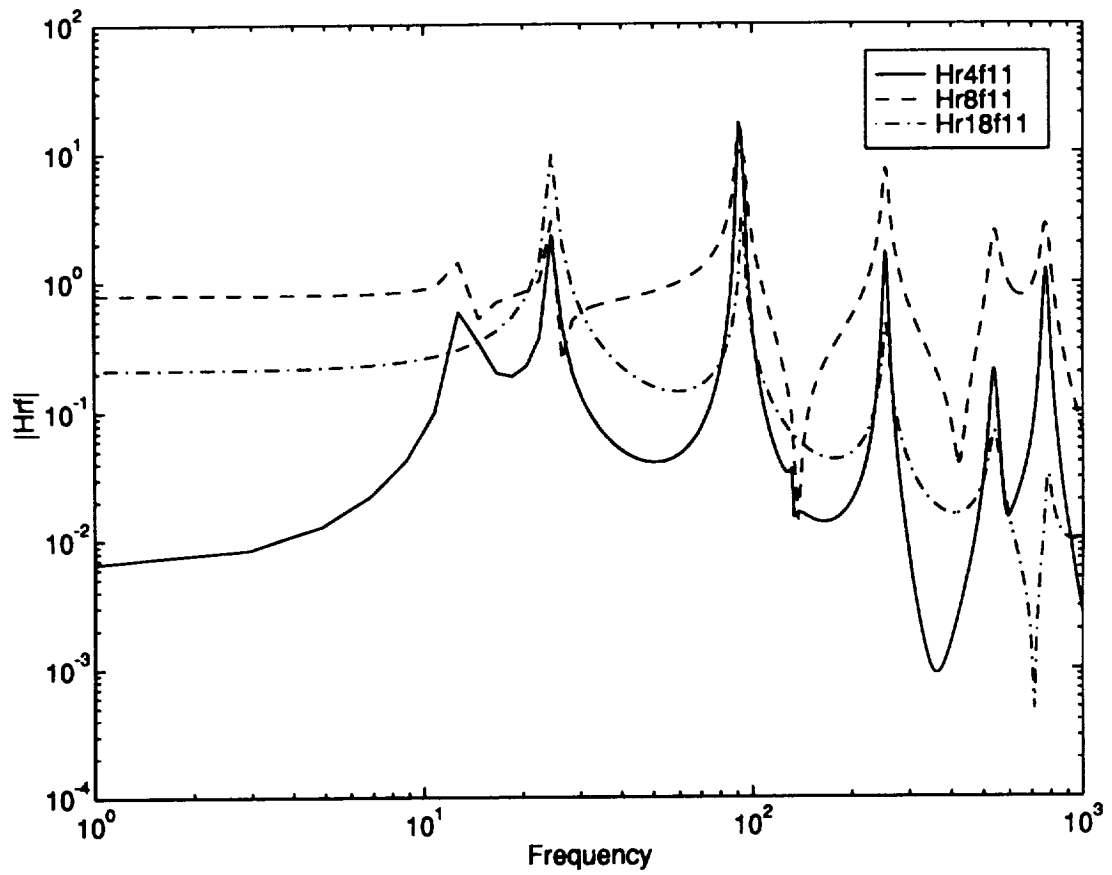Figure 6.42: Noisy Accelerance FRF of the Coupled System

Figure 6.43: Noise-Free Reaction Force Frequency Response Functions due to the Force at Node 11

# Chapter 7

# Conclusions and Recommendations

The purpose of this investigation was to examine the performance of a new structural identification algorithm, the Substructure System Identification algorithm, using numerical simulations for a moderate size finite element model. The algorithm successfully identified the substructure when active excitation was used at all the interface degrees of freedom and also for the case when reaction forces where measured at all the interface locations. The effects of spatial and frequency truncation were studied and it was found that the algorithm is capable of identifying valid reduced-order structural models. Simulations were also performed using data containing noise and it was shown that the algorithm is robust enough to handle such data.

A technique referred to as band processing was presented and shown to successfully identify structural models from noisy frequency data having a broad bandwidth. Thus, the SSID algorithm can be used as both a narrow-band and broad-band frequency-domain identification procedure. Pseudo degrees of freedom were examined as a way to expand the model size when there are more modes present in the data than there are output sensors. The model employing pseudo degrees of freedom was able to identify some of the additional modes when the original model could not.

The identified system matrices from the SSID algorithm were also

compared to other test-analysis models and it was found that the SSID reduced-order models represent the dynamic characteristics of the structure as well as, if not better than, the other test-analysis models. In addition, it was shown that the SSID reduced-order models provide the information necessary to obtain the fixed-interface modal data associated with the Craig-Bampton substructure model and the data associated with the constraint modes as well.

The following recommendations are made regarding the SSID algorithm and future work in this area:

- Remove the dependence on the scaling of the fixed-interface normal modes and determine an absolute measure that can be used to select the fixed-interface normal modes that contribute most to the target modes for the Craig-Bampton reduced-order models.

- Employ additional simulations to examine the identification of reduced-order models when the measured the reaction forces are included. Also, research is needed in the area of the measurement of reaction forces to determine acceptable reaction force levels.

- Investigate additional modal quality indicators for use in band processing and with models employing pseudo degrees of freedom to distinguish between structural and computational modes.

- Explore the band processing technique further, such as determining the optimal bandwidth and frequency resolution for different model sizes and modal densities. In addition, the SSID algorithm using the band processing technique should be implemented on a parallel-computing machine.

- Further study the area of proper model order determination for the SSID algorithm. The necessary steps needed to use pseudo degrees of freedom to increase the model order in the second stage of the SSID algorithm should be determined. Also, examine the case when there are much fewer modes than sensors. In this case, the resulting SSID model will not be a minimal-order model, but will be larger and the order of the model should somehow be reduced.

# Appendix A

# MATLAB© Source Code

```
% Set Parameters:
%   ne = No. Excitation Frequencies
%   nx = No. of DOF of Substructure Model
%   nf = No. of Active Forces
%   nr = No. of Reactions
%   ns = No. of States
%   nb = No. of DOF of Substructure and Test Stand
%   nsample = No. of samples of excitation source
%
clear rand('seed',0);
%
na=size(KA,1);
% Compute the mass-normalized eigenvectors
[phia,eiga]=massnorm(KA,MA);
freqa=sqrt(eiga)/(2*pi);
% Compute the modal damping matrix
[CA,zetaa]=damping(MA,KA,ones(na,1)*.02);
%
% Forced DOF: 10, 22, and 50
% Reaction DOF: NONE
fdof=[10 22 50]; nf=3; nr=0; nd=nf+nr;
%
% "Preserve" these modes of the "A" Structure
modes=[1:10,17,18,21,22,29,30];    %16 DOF Model
%modes=[1:10,17,18];                %12 DOF Model
%modes=[1:10];                      %10 DOF Model
% DOF to RETAIN from the Original Model
rdof=eidv(phia(:,modes),[1:na]',length(modes));
% DOF to OMITT from the Original Model
odof=omitdof(na,rdof);
% Retained Interior DOF of the Original Model and the Forced DOF
% of the Reduced Model
[a,ridof,frdof]=keptdof(na,odof,fdof(1:nf),fdof(nf+1:nd));
%
% Size of the substructure to identify
nx=length(rdof); ns=2*nx;
%
```

```
% Input Test Frequencies
ne=512; deltaf=1; fmin=1.0; fmax=300;
Freq=linspace(fmin,fmax,ne); W=Freq*2*pi; W2=W.^2;
%
% Noise parameters
nsample=40; magnoise=2.0/100.; phnoise=2*pi/180.; tol1=1e-10; tol2=1e-10;
%
% Initialize
DA=zeros(na,(nf+nr)); DAr=zeros(nx,(nf+nr));
for n=1:nd
   k=fdof(n);
   DA(k,n)=1;
   k=frdof(n);
   DAr(k,n)=1;
end
%
% Form Frequency-Response Vectors (Direct Solution)
[AB,P]=frfdirect(W,MA,CA,KA,DA);
%
% Simulate Noise
[ABn,Pn]=applynoise(AB,P,nsample,magnoise,phnoise);
%
% Remove Response Vectors Corresponding to "A" Structure
AA=ABn(rdof,:);
%
% Form Velocity and Displacement FRFs
[AA,VA,XA,Hff]=calvxf(AA,Pn,Freq); Hrf=[];
%
% LHS of Equation 3.7
VXFA=[VA;XA;-Hff];
%
% Form Real/Imaginary Partitions
% RHS of Equation 3.7
AA2=[real(AA) imag(AA)];
VXFA2=[real(VXFA) imag(VXFA)];
%
% Step 1 - Identification of M^-1K and M^-1C and the resulting eigensolution
% Solve Equation 3.7
%CKDAE2=-AA2/VXFA2;
[CKDAE2,V1,S1]=tls(VXFA2',-AA2',21,tol1,tol2,1); CKDAE2=CKDAE2';
%
% Complex Eigensolution Based on Estimated Minv*C and Minv*K
CHA=CKDAE2(:,1:nx);
KHA=CKDAE2(:,nx+1:ns);
DHA=CKDAE2(:,ns+1:ns+nd);
% Equation 3.11
```

144

```
ASAHATE=[CHA eye(nx);eye(nx) zeros(nx)];
BSAHATE=[KHA zeros(nx); zeros(nx) -eye(nx)];
% Equation 3.12 Lambda=LambdaHat
[CTHETAE,CLAMAE]=eig(-BSAHATE,ASAHATE);
[CTHETAE,CLAMAE]=eigensorti(CTHETAE,diag(CLAMAE));
zetass=-real(CLAMAE)./abs(CLAMAE);
omegss=imag(CLAMAE)./sqrt(1-zetass.^2);
%
% Step 2-Identification of M, C, and K
%
% Estimation of Inverse Generalized Modal Parameters
%
CTX=CTHETAE(1:nx,:);
%
E=zeros(nf*ne*nx,ns); R=zeros(ne,ns); Y=zeros(nf*ne*nx,1);
for k=1:ne
   for r=1:ns
      % Equation 3.19
      R(k,r)=-W2(k)/(j*W(k)-CLAMAE(r));
   end
end
%
offset=ne*nx;
for n=1:nf
   nof=n*offset-offset;
   for k=1:ne
      kk=nf*k-(nf-n);
      DF=DA(:,n)+DA(:,nf+1:nd)*Hrf(:,kk);
      for r=1:ns
         % Equation 3.24
         E((1+(k-1)*nx)+nof:(k*nx)+nof,r)=R(k,r)*CTX(:,r)*CTX(:,r).'*DF;
      end
      for r=1:nx
         % LHS of Equation 3.23
         Y(nx*(k-1)+r+nof)=AA(r,kk);
      end
   end
end
%
% Inverse Generalized Mass Estimation
% Solving Equation 3.23
GASAIE=E\Y;
%
% Estimated Generalized Modal Parameter Vector - $\tilde{a}_r$
GASAE=1./GASAIE;
%
```

```
% Estimated Generalized Modal Parameter Vector - b̃_r
% Solving Equation 3.25
GBSAE=-CLAMAE.*GASAE;
%
% Forming (Thetahat)^-1
CTHI=inv(CTHETAE);
%
% Estimated State-variable A Matrix
% Equation 3.26a
ASAE=CTHI.'*diag(GASAE)*CTHI;
%
% Estimated State-variable B Matrix
% Equation 3.26b
BSAE=CTHI.'*diag(GBSAE)*CTHI;
%
% Extract System Matrices
M1=real(ASAE(1:nx,nx+1:ns));
M2=real(ASAE(nx+1:ns,1:nx));
M3=-real(BSAE(nx+1:ns,nx+1:ns));
M=M3;
C=real(ASAE(1:nx,1:nx));
K=real(BSAE(1:nx,1:nx));
C2=damping(M,K,zetass(1:nx));
[phie,eige]=eig(K,M);
[phie,eige]=eigensortr(phie,diag(eige)); freqe=sqrt(eige)/(2*pi);


function [Haf,Hvf,Hxf,Hff]=calvxf(AA,P,Freq)
% [Haf,Hvf,Hff]=calvxf(AA,P,Freq)
% AA = Accelerations of the "A" structure
% P = applied forces
% Haf = Accelerance Frequency Response Function
% Hvf = [Haf]/(jw)
% Hxf = [Haf]/(-w^2)
% Hff
ne=length(Freq); nf=size(P,1); W=Freq*2*pi; W2=W.^2;
Haf=zeros(size(AA)); Hvf=zeros(size(AA));
Hxf=zeros(size(AA)); Hff=zeros(size(P));
%
for k=1:ne
  nk2=nf*k;
  nk1=nk2-(nf-1);
%
% Form Autospectrum
  Pstar=conj(P(:,nk1:nk2));
  Gff=P(:,nk1:nk2)*Pstar;
```

```
    Gffi=inv(Gff);
    Hff(:,nk1:nk2)=Gff*Gffi;
%
% Form [Haf]/(jw)-Mobility
    WB=eye(nf)*(1./(j*W(k)));
    Hvf(:,nk1:nk2)=(AA(:,nk1:nk2)*WB)*Pstar*Gffi;
%
% Form [Haf]/(-w^2)-Receptance
    W2B=-eye(nf)*1./W2(k);
    Hxf(:,nk1:nk2)=(AA(:,nk1:nk2)*W2B)*Pstar*Gffi;
%
% Form Haf-Accelerance
    Haf(:,nk1:nk2)=AA(:,nk1:nk2)*Pstar*Gffi;
end
```

```
function [ABn,Pn]=applynoise(AB,P,nsample,magnoise,phnoise)
% [ABn,Pn]=applynoise(AB,P,nsample,magnoise,phnoise)
nx=size(AB,1);
nf=size(P,1);
ne=size(AB,2)/nf;
ABn=zeros(size(AB));
Pn=zeros(size(P));
for k=1:nx
   for kk=1:nf
     ABn(k,kk:nf:nf*ne)=addnoise(AB(k,kk:nf:nf*ne),nsample,magnoise,phnoise);
   end
end
for k=1:nf
   Pn(k,k:nf:nf*ne)=addnoise(P(k,k:nf:nf*ne),nsample,magnoise,phnoise);
end



function XN=addnoise(X,Navg,magnoise,phnoise)
% XN=addnoise(X,Navg,magnoise,phnoise)
% XN = output signal with the noise added
% X = the original signal
% Navg = the number of avergages
% magnoise = the noise on the magnitude
% phnoise = the noise on the phase
[nx nf]=size(X);
Xreal=real(X);
Ximag=imag(X);
% Compute magnitude and phase of base signal
Xmag=sqrt( (Xreal).^2 + (Ximag).^2 );
Xphase=atan2(Ximag,Xreal);
% RMS value of base signal
Hrms=norm(Xmag)/length(Xmag);
% Percentage of RMS value of base signal
noisescale=Hrms*magnoise;
XN=zeros(size(X));
I=ones(size(Xmag));
for k=1:Navg
   Nmag=zeros(size(Xmag));
   Nphase=zeros(size(Xphase));
% Calculate and add noise for magnitude
   R1=rand(nx,nf);
   R2=rand(nx,nf);
   noiseM=(I-2*R1);
   noiseM=noiseM-mean(noiseM);
   Nrms=norm(noiseM)/length(noiseM);
   SNmag=noisescale/Nrms;
```

148

```
    Nmag=SNmag*noiseM;
% Calculate and noise for phase
    noisePh=(I-2*R2);
    noisePh=noisePh-mean(noisePh);
    Nphase=phnoise*noisePh;
%
    XNmag=Xmag+Nmag;
    XNph=Xphase+Nphase;
%
    XNreal=XNmag.*cos(XNph);
    XNimag=XNmag.*sin(XNph);
    XNnk=XNreal+j*XNimag;
    XN=XN+XNnk;
end
XN=XN/Navg;
```

```
function [X,V,S]=tls(A,B,rank,tol1,tol2,comp)
% Solves the Total Least Squares problem AX=B
% [X,V,S]=tls(A,B,rank,tol1,tol2,comp)
% A    The data matrix (mxn)
% B    The observation matrix (nxd)
% rank The rank of [A;B], if set to zero it will be computed
% tol1 Two possibilities depending on the value of comp
%        Specifies the tolerance to be used when checking for multiplicity of
%        singular vales OR the estimated standard deviation of the error on
%        each element of the matrix C
% tol2 Tolerance used to check for the singularity of the upper triangular
%        matrix F, see description
% comp Specifies whether rank and/or tol1 is to be computed by the routine
%        comp = 1 rank is to be computed
%             = 2 tol1 is to be computed (stdv is input by the user)
%             = 3 neither tol1 nor rank is computed
%             = 4 both rank and tol1 are to be computed (stdv is input)
% X    The solution to the TLS problem, the leading nxd part of the array
% V    The right singular vectors of [A;B]
% S    The singular values of C in descending order

% Reference S.Van Huffel (ESAT Laboratory, KU Leuven).
crank=1; ctol=1;
if comp==3
  crank=0;
  ctol=0;
else
  if comp==1
ctol=0;
  end
  if comp==2
crank=0;
  end
end
tol1=max([tol1 eps]); tol2=max([tol2 eps]);
[m,n]=size(A); l=size(B,2); nl=n+1;
X=zeros(n,l); k=max([m nl]); p=min([m n]);
[U,S,V]=svd([A,B],0); S=diag(S);
%
% Step 2: Compute the rank approximation of [A B]
smax=tol1;
% Compute smax if requested
if ctol==1
  smax=sqrt(2.*k)*smax;
end
smax2=smax^2;
```

```
% Compute the rank if requested
if crank==1
  rank=p;
  while (rank>0) & (S(rank)<=smax)
    if rank > 0
      if S(rank) <= smax
        rank=rank-1;
      end
    end
  end
end
% Adjust the rank if S(rank) has multiplicity > 1
flag=0;
while flag==0
  r1=rank+1;
  while (rank>0) & ((S(rank)^2-S(r1)^2)<=smax2)
    if rank > 0
      if (S(rank)^2-S(r1)^2)<=smax2
        rank=rank-1;
        'Rank lowered because singular value had multiplicity > 1'
      end
    end
  end
  r1=rank+1;
%
% Compute the Householder matrix Q and matrices F and Y
%
  nl1=max([n r1])+1;
  zero=0;
  i=nl;
  while ( (~zero) & (i>=nl1) )
    if ( (~zero) & (i>=nl1) )
      k=i-rank;
      WRK=V(i,r1:r1+k-1);
      [WRK,temp,zero]=housh(WRK,k,tol2);
      if (~zero)
        V=tr2(V,WRK,temp,1,i,rank,k);
      end
      i=i-1;
    end
  end
%
  n1=n+1;
  if ((zero) | (abs(V(n1,n1))<=tol2))
    rank=rank-1;
    'Rank lowered because singular upper triangular matrix F'
```

```
        flag=0;
    else
        flag=1;
    end
end
X(1:n,1)=X(1:n,1)+(-1.)/V(n1,n1)*V(1:n,n1);
for j=2:l
    nj=n+j;
    temp=V(nj,nj);
    j1=j-1;
    for i=1:n
        X(i,j)=-(V(i,nj)+dot(V(n1:n1+j1-1,nj),X(i,1:j1)))/temp;
    end
end
```

152

```
function [u,s,zero]=housh(u,j,heps)
%HOUSH Construct a householder transformation H=I-s*UU'.
%
%       [U,S,ZERO] = HOUSH(U,J,Heps)
%  Constructs a Householder transformation H=I-s*UU' that 'mirrors' a
%  vector u to the Jth unit vector. If NORM(U)<Eps then Zero=1 [True]
%
%  Reference: Adapted from "Computation of Zeros of Linear Multivariable
%             Systems", A. Emami-Naeini, and P. Van Dooren; Automatica
%             Vol. 18, No. 4, pp. 415-430, 1982.
s = sum(u.*u);
alfa = sqrt(s);
if (alfa<=heps), zero=1; return, end
zero=0;
dum = u(j);
if dum>0, alfa=-alfa; end
u(j) = u(j)-alfa;
s = 1 ./(s-alfa*dum);
% Make u a column vector.
u = u(:);
```

```
function A=tr2(A,U,s,i1,i2,j1,j2)
  inprod=0.0;
  for j=1:j2
    inprod=inprod+U(j)*A(i,j1+j);
  end
  y=inprod*s;
  for j=1:j2
    A(i,j1+j)=A(i,j1+j)-U(j)*y;
  end
end
```

# Bibliography

[1] Craig, R. R., Jr., "A Review of Time-Domain and Frequency-Domain Component Mode Synthesis Methods," *International Journal of Analytical and Experimental Modal Analysis*, Vol. 2, No. 2, April 1987, pp. 59–72.

[2] Craig, R. R., Jr., "Substructure Methods in Vibration," *Transactions of the ASME*, Vol. 117(B), June 1995, pp. 207–213.

[3] Craig, R. R., Jr., "A New Substructure System Identification Method," Paper No. 95–1298, *Proceedings of the AIAA/ASME/ASCE/AHS/ASC 36th Structures, Structural Dynamics, and Materials Conference*, New Orleans, LA, April 1995, pp. 1209–1217.

[4] Craig, R. R., Jr., Cutshall, W. K., and Blades, E. L., "A New Substructure System Identification Method," *Report CAR 95-1*, Center for Aeromechanics Research, The University of Texas at Austin, Dec. 1995.

[5] Ewins, D. J., *Modal Testing: Theory and Practice*, Research Studies Press Ltd., Taunton, Somerset, England, 1995.

[6] Smith, S. W., "Iterative Use of Direct Matrix Updates: Connectivity and Convergence," Paper No. 92–2384, *Proceedings of the AIAA/ASME/ASCE/AHS/ASC 33rd Structures, Structural Dynamics, and Materials Conference*, Dallas, TX, April 1992, pp. 1797–1806.

154

[7] Farhat, C., and Hemez, F., "A Robust Methodology for the Simultaneous Updating of Finite Element Mass and Stiffness Matrices," Paper No. 95-1443, *Proceedings of the AIAA/ASME/ASCE/AHS/ASC 36th Structures, Structural Dynamics, and Materials Conference*, New Orleans, LA, April 1995, pp. 2488-2498.

[8] Hemez, F. M., "Closing the Gap Between Modal Parameter Based and Frequency Response Function Based Updating Methods," *Proceedings of the 13th International Modal Analysis Conference*, Nashville, TN, Feb. 1995, pp. 171-178.

[9] *Space Shuttle Payload Design and Development, Structural/Mechanical Interfaces and Requirements*, Revision C., NSTS 20052, Vol. 8, NASA-Lyndon B. Johnson Space Center, Houston, TX, June 1988.

[10] Blair, M. A., "Space Station Module Prototype Alternative Tests: Convergence to Fixed Base," *Proceedings of the 11th International Modal Analysis Conference*, Kissimmee, FL, Feb. 1993, pp. 959-964.

[11] Admire, J. R., Tinker, M. L., and Ivey, E. W., "Mass-Additive Test Method for Verification of Constrained Structural Models," *AIAA Journal*, Vol. 31, No. 11, Nov. 1993, pp. 2148-2153.

[12] Driskell, T. C., Anderson, J. B., and Coleman, A. D., "Free-Free and Fixed Base Modal Surveys of the Space Station Common Module Prototype," *Proceedings of the 10th International Modal Analysis Conference*, San Diego, CA, Feb. 1992, pp. 117-123.

[13] Brillhart, R. D., Hunt, D. L., Flanigan, C. C., Guinn, R., and Hull, R., "Transfer Orbit Stage Modal Survey Part 1—Measurement of Free-Free Modes and Residual Flexibility," *Proceedings of the 7th International Modal Analysis Conference*, Las Vegas, NV, Feb. 1989, pp. 1150–1156.

[14] Brillhart, R. D., Hunt, D. L., Flanigan, C. C., Guinn, R., and Hull, R., "Transfer Orbit Stage Modal Survey Part 2—Model Correlation," *Proceedings of the 7th International Modal Analysis Conference*, Las Vegas, NV, Feb. 1989, pp. 1157–1161.

[15] Admire, J. R., Tinker, M. L., and Ivey, E. W., "Residual Flexibility Test Method for Verification of Constrained Structural Models," *AIAA Journal*, Vol. 32, No. 1, Jan. 1994, pp. 170–175.

[16] Blair, M. A., and Vadlamudi, N., "Constrained Structural Dynamic Model Verification Using Free Vehicle Suspension Testing Methods," Paper No. 88-2359, *Proceedings of the AIAA/ASME/ASCE/AHS/ASC 36th Structures, Structural Dynamics, and Materials Conference*, Williamsburg, VA, April 1988, pp. 1187–1193.

[17] Blair, M. A., and Vadlamudi, N., "Hubble Space Telescope-Space Shuttle Interface Dynamic Verification Test," *Proceedings of the 7th International Modal Analysis Conference*, Las Vegas, NV, Feb. 1989, pp. 657–663.

[18] Chung, Y. T., Sernaker, M. L., and Peeples, J. H., "Simulating Flight Boundary Conditions for Orbiter Payload Modal Survey," Paper No. 93-1605, *Proceedings of the AIAA/ASME/ASCE/AHS/ASC 34th Structures,*

156

*Structural Dynamics, and Materials Conference*, La Jolla, CA, April 1993, pp. 2624–2630.

[19] Mühlbauer, K., Troidl, H., and Dillinger, S., "Design, Modeling and Verification of a Modal Survey Test Fixture for Space Shuttle Payloads," *Proceedings of the 10th International Modal Analysis Conference*, San Diego, CA, Feb. 1992, pp. 1005–1009.

[20] Juang, J. N., *Applied System Identification*, Prentice Hall PTR, Englewood Cliffs, NJ, 1994.

[21] Chen, J. C., "Evaluation of Spacecraft Modal Test Methods," *Journal of Spacecraft and Rockets*, Vol. 24, No. 1, Jan.–Feb. 1987, pp. 52–62.

[22] Gaylardt, D., and Quantz, C., "Comparative Results from Time and Frequency Domain Modal Parameter Estimation Algorithms," *Proceedings of the 5th International Modal Analysis Conference*, London, England, April 1987, pp. 115–121.

[23] Richardson, M. H., and Formenti, D. L., "Parameter Estimation from Frequency Response Measurements Using Rational Fraction Polynomials," *Proceedings of the First International Modal Analysis Conference*, Orlando, FL, Nov. 1982, pp. 167–181.

[24] Peterson, L. D., and Alvin, K. F., "A Time and Frequency Domain Procedure for Identification of Structural Dynamic Models," Paper No. 94–1731, *Proceedings of the AIAA/ASME/ASCE/AHS/ASC 35th Structures, Structural Dynamics, and Materials Conference–Adaptive Structures Forum*, Hilton Head, SC, April 1994, pp. 14–24.

[25] Leuridan, J. M., Brown, D. L., and Allemang, R. J., "Direct System Parameter Identification of Mechanical Structures with Application to Modal Analysis," Paper No. 82-0767, *Proceedings AIAA/ASME/ ASCE/AHS/ASC 23rd Structures, Structural Dynamics, and Materials Conference*, New Orleans, LA, May 1982, pp. 548-556.

[26] Juang, J. N., and Pappa, R. S., "An Eigensystem Realization Algorithm for Modal Parameter Identification and Model Reduction," *Journal of Guidance, Control, and Dynamics*, Vol. 8, No. 6, Sept.-Oct. 1985, pp. 620-627.

[27] Juang, J. N., Cooper, J. E., and Wright, J. R., "An Eigensystem Realization Algorithm Using Data Correlations (ERA/DC) for Modal Parameter Identification," *Control Theory and Advanced Technology*, Vol. 4, No. 1, March 1988, pp. 5-14.

[28] Juang, J. N., and Suzuki, H., "An Eigensystem Realization Algorithm in Frequency Domain for Modal Parameter Identification," *Journal of Vibration, Acoustics, Stress, and Reliability in Design*, Vol. 110, No. 1, Jan. 1988, pp. 24-29.

[29] Vold, H., Kundrat, J., Rocklin, T., and Russell, R., "A Multi-Input Modal Parameter Estimation Algorithm for Mini-Computers," SAE Paper No. 820194, *SAE Transactions*, Vol. 91, No. 1, 1982, pp. 815-821.

[30] Juang, J. N., "Mathematical Correlation of Modal Parameter Identification Methods via System Realization Theory," *International Journal of*

158

*Analytical and Experimental Modal Analysis*, Vol. 2, No. 1, Jan. 1987, pp. 1–18.

[31] Su, T. J., and Juang, J. N., "Substructure System Identification and Synthesis," *Journal of Guidance, Control, and Dynamics*, Vol. 17, No. 5, Oct. 1994, pp. 1087–1095.

[32] Alvin, K. F., and Park, K. C., "Second-Order Structural Identification Procedure via State-Space-Based System Identification," *AIAA Journal*, Vol. 32, No. 2, Feb. 1994, pp. 397–406.

[33] Leuridan, J. M., "Direct System Parameter Identification of Mechanical Structures with Application to Modal Analysis," Masters Thesis, Dept. of Mechanical and Industrial Engineering, University of Cincinnati, 1981.

[34] Potter, R., and Richardson, M., "Mass, Stiffness, and Damping Matrices from Measured Modal Parameters," Paper No. 74–630, *International Instrumentation-Automation Conference & Exhibit*, New York, NY, Oct. 1974, 5 pp.

[35] Balmès, E., "New Results on the Identification of Normal Modes From Experimental Complex Modes," *Proceedings of the 12th International Modal Analysis Conference*, Honolulu, HI, Jan. 1994, pp. 1576–1582.

[36] Lembregts, F., "Frequency Domain Identification Techniques for Experimental Mutliple Input Modal Analysis," Doctoral Dissertation, Dept. of Mechanical Engineering, Katholieke Universititeit Leuven, Leuven, Belgium, 1988.

[37] Lembregts, F., Leuridan, J., and Van Brussel, H., "Frequency Domain Direct Parameter Identification for Modal Analysis: State Space Formulation," *Mechanical Systems and Signal Processing*, Vol. 4, No. 1, 1990, pp. 65–75.

[38] Allemang, R. J., Brown, D. L., and Fladung, W., "Modal Parameter Estimation: A Unified Matrix Polynomial Appraoch," *Proceedings of the 12th International Modal Analysis Conference*, Honolulu, HI, Jan. 1994, pp. 501–514.

[39] Li, S., Brown, D. L., and Vold, H., "A Scaled Total Least Squares Method for Modal Parameter Estimation Using the Unified Matrix Polynomial Approach," *Proceedings of the 12th International Modal Analysis Conference*, Honolulu, HI, Jan. 1994, pp. 912–918.

[40] Li, S., Brown, D. L., and Vold, H., "Using the Scaled Total Least Squares Method and the Unified Matrix Polynomal Approach for Condensing the Perturbed Boundary Consition Test Data," *Proceedings of the 13th International Modal Analysis Conference*, Nashville, TN, Feb. 1995, pp. 1853–1860.

[41] Alvin, K. F., Peterson, L. D., and Park, K. C., "Method for Determining Minimal-Order Mass and Stiffness from Modal Test Data," *AIAA Journal*, Vol. 33, No. 1, Jan. 1995, pp. 128–135.

[42] Craig, R. R., Jr., Kurdila, A. J. and Kim, H. M., "State-Space Formulation of Multi-Shaker Modal Analysis," *International Journal of Analytical and Experimental Modal Analysis*, Vol. 5, No. 3, July 1990, pp. 169–183.

[43] Freed, A. M., and Flanigan, C. C., "A Comparison of Test-Analysis Model Reduction Methods," *Proceedings of the 8th International Modal Analysis Conference*, Kissimmee, FL, Jan. 1990, pp. 1344–1347.

[44] Guyan, R., J., "Reduction of Stiffness and Mass Matrices," *AIAA Journal*, Vol. 3, No. 2, Feb. 1965, p. 380.

[45] Henshall, R., D., and Ong, J. H. "Automatic Masters for Eigenvalue Economisation," *International Journal of Earthquake Engineering and Structural Dynamics*, Vol. 3, No. 4, April–June 1975, pp. 375–383.

[46] Anderson, R. G., Irons, B. M., and Zienkiewicz, O. C., "Vibration and Stability of Plates Using Finite Elements," *International Journal of Solids & Structures*, Vol. 4, No. 10, Oct. 1968, pp. 1031–1055.

[47] O'Callahan, J. C., "A Procedure for an Improved Reduced System (IRS) Model," *Proceedings of the 7th International Modal Analysis Conference*, Las Vegas, NV, Feb. 1989, pp. 17–21.

[48] Flanigan, C. C., "Development of the IRS Component Dynamic Reduction Method for Substructure Analysis," Paper No. 91–1056, *Proceedings AIAA/ASME/ASCE/AHS/ASC 32th Structures, Structural Dynamics, and Materials Conference*, Baltimore, MD, April 1991, pp. 2504–2509.

[49] Gordis, J. H., "An Analysis of the Improved Reduced System (IRS) Model Reduction Procedure," *The International Journal of Analytical and Experimental Modal Analysis*, Vol. 9, No. 4, Oct. 1994, pp. 269–285.

[50] Kammer, D. C., "Test-Analysis Model Development Using an Exact Modal Reduction," *The International Journal of Analytical and Experimental Modal Analysis*, Oct. 1987, pp. 174–179.

[51] O'Callahan, J. C., "System Equivalent Reduction/Expansion Process (SEREP)," *Proceedings of the 7th International Modal Analysis Conference*, Las Vegas, NV, Feb. 1989, pp. 29–37.

[52] Kammer, D. C., "A Hybrid Approach to Test-Analysis-Model Development for Large Space Structures," *Journal of Vibration and Acoustics*, Vol. 113, No. 3, July 1995, pp. 325–332.

[53] Bhatia, S. S., and Allemang, R. J., "A Test-Analysis-Matrix (TAM) with Improved Dynamic Characteristics," *Proceedings of the 13th International Modal Analysis Conference*, Nashville, TN, Feb. 1995, pp. 1506–1514.

[54] Hurty, W. C., "Dynamic Analysis of Structural Systems by Component Mode Synthesis," *AIAA Journal*, Vol. 3, No. 4, April 1965, pp. 678–685.

[55] Craig, R. R., Jr., and Bampton, M. C. C., "Coupling of Substructures for Dynamic Analyses," *AIAA Journal*, Vol. 6, No. 7, July 1968, pp. 1313–1319.

[56] Huang, H. H., and Craig, R. R., Jr., "System Identification and Model Updating for Substructures," *Report CAR 92-1*, Center for Aeromechanics Research, The University of Texas at Austin, April 1992.

[57] Kammer, D. C., and Flanigan, C. C., "Development of Test-Analyis Models for Large Space Structures Using Substructure Representations," *Jour-

162

*nal of Spacecraft and Rockets*, Vol. 28, No. 2, March–April 1991, pp. 244–250.

[58] Craig, R. R., Jr, and Bampton, M. C. C., "On the Iterative Solution of Semidefinte Eigenvalue Problems," *The Aeronautical Journal of the Royal Aeronautical Society*, Vol. 75, No. 724, April 1971, pp. 287–290.

[59] Golub, Gene H., and Van Loan, Charles F., *Matrix Computations*, The John Hopkins University Press, Baltimore, MD, 1983.

[60] Strang, Gilbert, *Linear Algebra and Its Applications*, 3rd ed., Harcourt Brace Jovanovich, Inc., San Diego, CA, 1988.

[61] Van Huffel, S., and Vandewalle, J., *The Total Least Squares Problem: Computational Aspects and Analysis*, Society of Industrial and Applied Mathematics, Philadelphia, PA, 1991.

[62] Klema, V. C., and Laub, A. J., "The Singular Value Decomposition: Its Computation and Some Applications," *IEEE Transactions on Automatic Control*, Vol. 25, No. 2, April 1980, pp. 164–176.

[63] Craig, R. R., Jr., Blades, E. L., and Cutshall, W. K., "A Reduced-Order Substructure System Identification Method," Paper No. 96–1200, *Proceedings of the AIAA Dynamics Specialists Conference*, Salt Lake City, UT, April 1996, pp. 12–20.

[64] Mast, J. R., and Craig, R. R., Jr., "Measurement of Dynamic Reactions at Interface Points for use in Susbstructure System Identification," Masters

Thesis, Dept. of Aerospace Engineering and Engineering Mechanics, The University of Texas at Austin, Aug. 1994.

[65] *MATLAB©*, The MathWorks, Natick, MA, 1991.

[66] Kammer, D. C., "Sensor Placement for On-Orbit Modal Identification and Correlation of Large Space Structures," *Journal of Guidance, Control, and Dynamics*, Vol. 14, No. 2, March–April 1991, pp. 251–259.

[67] Berman, A., "Multiple Acceptable Solutions in Structural Model Improvement," *AIAA Journal*, Vol. 33, No. 5, May 1995, pp. 924–927.